UNIVERSITY OF CALIFORNIA

Los Angeles

Spin-Motion Entanglement with a Single Mode-Locked Laser Pulse

A dissertation submitted in partial satisfaction

of the requirements for the degree

Doctor of Philosophy in Physics

by

Randall Paul Putnam

2024

ABSTRACT OF THE DISSERTATION

Spin-Motion Entanglement with a Single Mode-Locked Laser Pulse

by

Randall Paul Putnam

Doctor of Philosophy in Physics

University of California, Los Angeles, 2024

Professor Paul Hamilton, Co-Chair

Professor Wesley Campbell, Co-Chair

A single 16 ps laser pulse performs single qubit rotations as well as generates entanglement of the spin and motional degrees of freedom in a single, trapped $^{138}Ba^{+}$ ion. The fidelity of these single qubit rotations was found to be consistent with 100%, $(97^{+3}_{-4})\%$. Entanglement is demonstrated through the collapse and revival of spin coherence as the spin components of the wavefunction separate and recombine in phase space.

The dissertation of Randall Paul Putnam is approved.

Hong-Wen Jiang

Eric R. Hudson

Wesley Campbell, Committee Co-Chair

Paul Hamilton, Committee Co-Chair

University of California, Los Angeles

2024

TABLE OF CONTENTS

LIST OF FIGURES

LIST OF TABLES

VITA

2013-2015 Fresno Community College

2015-2017 B.A. Physics, University of California Berkeley

2017-present University of California Los Angeles

PUBLICATIONS

A. West, R. Putnam, W. C. Campbell, and P. Hamilton. "Tunable transverse spin–motion coupling for quantum information processing." *Quantum Science and Technology* (2021)

R. Putnam, A. West, W. C. Campbell, and P. Hamilton. "Impulsive Spin-Motion Entanglement for Fast Quantum Computation and Sensing." *preprint available, arXiv:2307.11287* (2023)

CHAPTER 1

Introduction

Since humans have been making tools, we have made tools to enhance our senses. Throughout the years the fundamental mechanisms behind these sensors have increased in complexity leading to more precise and accurate measurements. This dissertation will go over the research I have done to further advance these measurements.

1.1 Motivation

Sensor precision reached new heights with the invention of atomic trapping techniques such as the ion trap and later the magneto-optical-trap, or MOT. One of the major advancements to sensor precision came with the advent of the atomic clock, carefully calibrating time based on the fundamental energy splitting of a particular atom. Not only can atoms tell time, they are also incredible force sensors. Atom interferometers are some of the most precise devices to measure gravity, electric fields, magnetic fields, even ruling out some fifth force theories.

With this in mind, a proof-of-principle rotation sensor based on a trapped-ion interferometer began construction [CH17]. The basic scheme is to create a wavefunction superposition of two counter-rotating states. The states will each pick up a phase. Particularly, when the apparatus is rotated in the plane of the ion orbits the counter-rotating superposition states will pick up opposite phases due to the rotation. This phase difference, known as the Sagnac phase, can be used to deduce the apparatus rotation rate. Although ions are not the typical choice for interferometers, there are some benefits to using trapped ions for Sagnac phase measurements.

1.2 Background

Rotation sensors, or gyroscopes have long been constructed for use in navigation. Today, the most sensitive gyroscopes measure angular velocities, $\vec{\Omega}$, utilizing the Sagnac effect with photonic wavepackets of wavelength λ. The phase difference between the wavepackets due to the rotation can be calculated

$$\Delta\phi = \frac{4\pi}{\lambda c}\vec{A}\cdot\vec{\Omega},$$

with c the speed of light in vacuum and $\vec{A}$ the path-length area of the interfering wavepackets [POS67].

Motivated by the benefits of atomic interferometers discussed above, academic groups set out to measure the Sagnac effect with atomic wavepackets. Atomic gyroscopes use atoms of mass M to measure angular velocities, $\vec{\Omega}$, utilizing the Sagnac effect. Different points of view can be used to calculate the phase difference between the atomic wavepackets due to the rotation [RKW91], but the result is the same

$$\Delta\phi = \frac{2M}{\hbar}\vec{A}\cdot\vec{\Omega},$$

where the interferometer area $\vec{A}$ depends on the differential momentum imparted by the interferometer beamsplitters.

The phases can be compared using the atom's Compton wavelength, $\lambda_{\text{atom}} = \frac{h}{Mc} \Rightarrow 2M/\hbar = 4\pi/(\lambda_{\text{atom}}c)$ or substituting in the particle energies. The photon energy is $E_{\text{photon}} = hc/\lambda$. The electronic energy of the atom is negligible, so the atom's energy can be expressed as $E_{\text{atom}} = \gamma Mc^2$, with $\gamma = 1/\sqrt{1 - v_{\text{atom}}^2/c^2}$ the Lorentz factor and v_{atom} the atom's center-of-mass velocity. Realistic experiments use non-relativistic speeds ($\gamma = 1$), so the Sagnac phase from both interferometer schemes can be expressed as

$$\Delta\phi = \frac{4\pi E}{hc^2}\vec{A}\cdot\vec{\Omega}. \tag{1.1}$$

Typical optical photons have energy $E \sim 1$ eV while atoms' rest mass energies are typically $E \sim 10^{11}$ eV. Using fiber optics, optical interferometer areas can easily exceed 10^5 m^2 while atom interferometer areas rarely exceed 10^{-3} m^2. While the phase shifts in atomic interferometers are much larger than their optical counterparts, optical gyroscopes reach higher sensitivities due to the increased number of interfering

particles. To increase the atom interferometer area, the beamsplitter operation could be made to impart more momentum, a larger apparatus can be constructed, or the interferometer path made to circle back in on itself such that the atomic wavepackets traverse around the interferometer's physical area multiple times, leading to a multiplication of the effective interferometer area. Practically, increasing the apparatus size is not desirable, so a scheme utilizing large-momentum beamsplitter operations and orbiting interferometer paths will be used.

To create a wavefunction superposition of two counter-rotating states, a spin-dependent momentum transfer scheme is used in an ion trap. To obtain a large momentum transfer, multiple kicks should be performed. A practical limitation to the momentum transfer is the kick timing: all the kicks need to be applied much faster than the motion of the ion in the trap to ensure the constructive addition of the momentum kicks. To this end, a single pulse from a mode-locked laser is desirable to drive this spin-dependent kick. Mode-locked lasers provide ultrafast, high-power pulses at a high repetition rate. The seminal study of spin-dependent kicks in trapped ions used stimulated Raman transitions between hyperfine ground states of a trapped $^{9}Be^{+}$ ion [MMK96]. Later studies using stimulated Raman transitions in the ground-state hyperfine qubit of $^{171}Yb^{+}$ were able to demonstrate qubit rotations using a single-pulse from a mode-locked laser with 72% fidelity, limited by the laser pulse's finite bandwidth [CMQ10]. Spin-dependent kicks with a single pulse were not possible using the $^{171}Yb^{+}$ hyperfine qubit due to multi-photon transitions leading to higher-order momentum states being populated [MSN13]. To remedy this problem, stimulated Raman transitions in a Zeeman qubit can be employed. Due to the potential for a smaller qubit splitting when using Zeeman states, the fidelity of ultrafast single-pulse qubit rotations can be increased above 99%. Multi-photon transitions between the ground state Zeeman qubit of an spin-zero-nucleus ion can also be precluded by polarization selectivity of the Raman beams. The majority of the research presented here will be investigating single-pulse operations in the ground-state Zeeman qubit of a trapped $^{138}Ba^{+}$ ion.

CHAPTER 2

Atom-Light Interactions

2.1 Rotating Atomic Schrodinger Equation (RASE)

At any time the atom's internal state, $|\Psi\rangle$, can be described by a superposition $|\Psi\rangle = \sum_n c_n|\psi_n\rangle$ where c_n are complex time-dependent amplitudes and $|\psi_n\rangle$ are the eigenfunctions of the atomic Hamiltonian, with corresponding eigenenergies $E_n = \langle\psi_n|\mathcal{H}_{\text{atom}}|\psi_n\rangle = \hbar\omega_n$.

Applying a laser to the atom causes an interaction, $V_{mn} = \langle\psi_m|\mathcal{H}_{\text{int}}|\psi_n\rangle$. With $\hbar = 1$, the schrodinger equation can be written:

$$i|\dot{\Psi}\rangle = \mathcal{H}|\Psi\rangle = (\mathcal{H}_{\text{atom}} + \mathcal{H}_{\text{int}})|\Psi\rangle \tag{2.1}$$

$$\Rightarrow i\sum_m \dot{c}_m|\psi_m\rangle = \sum_m c_m(\mathcal{H}_{\text{atom}} + \mathcal{H}_{\text{int}})|\psi_m\rangle \tag{2.2}$$

$$\Rightarrow i\sum_m \dot{c}_m\langle\psi_n|\psi_m\rangle = \sum_m c_m\langle\psi_n|\mathcal{H}_{\text{atom}} + \mathcal{H}_{\text{int}}|\psi_m\rangle \tag{2.3}$$

$$i\sum_m \dot{c}_m\delta_{nm} = \sum_m \omega_m c_m\delta_{nm} + \sum_m c_m\langle\psi_n|\mathcal{H}_{\text{int}}|\psi_m\rangle \tag{2.4}$$

$$\Rightarrow i\dot{c}_n = \omega_n c_n + \sum_m V_{mn}c_m \tag{2.5}$$

$$\Rightarrow i\dot{\tilde{c}}_n = \sum_m V_{mn}\tilde{c}_m e^{i(\omega_n-\omega_m)t}, \tag{2.6}$$

in a rotating frame with $\tilde{c}_n = c_n e^{i\omega_n t}$, and $i\dot{\tilde{c}}_n = -\omega_n c_n e^{i\omega_n t} + i\dot{c}_n e^{i\omega_n t}$.

2.2 Two-Level Atom

Starting with just two atomic levels with splitting ω_0 interacting with a laser of frequency ω, and therefore detuning, $\Delta = \omega - \omega_0$ as shown in Fig. 2.1, the population dynamics can be calculated starting with Eq. (2.6).

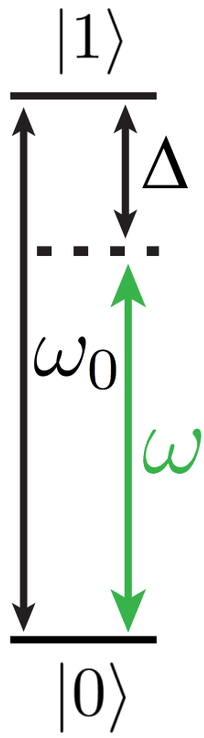

Figure 2.1: Two-level atom with energy splitting ω_0 interacting with a laser of detuning $\Delta = \omega - \omega_0$.

The laser field is composed of electric and magnetic fields. In general, the interaction of the laser electric field and the atom's electric dipole moment $\left(\vec{d} \cdot \vec{E}\right)$ will be much stronger than the laser magnetic field interacting with the atom's magnetic dipole moment $\left(\vec{\mu} \cdot \vec{B}\right)$, so the interaction Hamiltonian can be expressed $\mathcal{H}_{\text{int}} = -\vec{d} \cdot \vec{E}$. For a laser of frequency ω directed along $\hat{x}$ with the evolving transverse spatial profile $E_0(y, z, t)$, the electric field can be expressed:

$$\vec{E}(x, y, z, t) = \Re\left[E_0(y, z, t) e^{-i(\omega t - kx + \phi_0)} \hat{\epsilon}\right] \tag{2.7}$$

$$= \frac{1}{2} E_0(y, z, t) \left(e^{-i(\omega t - kx + \phi_0)} \hat{\epsilon} + e^{i(\omega t - kx + \phi_0)} \hat{\epsilon}^*\right). \tag{2.8}$$

Assuming the atomic wavepacket is much smaller than the wavelength of the light, known as the dipole approximation, the spatial dependence of the electric field can be taken as a constant. The electric field interaction at the ion position $\vec{r}_0 = (x_0, y_0, z_0)$ can be rewritten

$$\mathcal{H}_{\text{int}} = -\frac{1}{2} \mathcal{E}(t) \left(e^{-i(\omega t + \varphi)} \vec{d} \cdot \hat{\epsilon} + e^{i(\omega t + \varphi)} \vec{d} \cdot \hat{\epsilon}^*\right), \tag{2.9}$$

with $\mathcal{E}(t) = E_0(y_0, z_0, t)$ and $\varphi = -kx + \phi_0$. Solving for the population dynamics of this Hamiltonian, Eq. (2.6) expands into 2 equations:

$$\begin{aligned} i\dot{\tilde{c}}_0 &= V_{10}\tilde{c}_1 e^{-i\omega_0 t} = \left(\frac{1}{2}g_{01}(t)e^{-i\omega t} + \frac{1}{2}g_{01}^*(t)e^{i\omega t}\right)\tilde{c}_1 e^{-i\omega_0 t} \\ &= \frac{1}{2}\tilde{c}_1\left(g_{01}(t)e^{-i(\omega+\omega_0)t} + g_{01}^*(t)e^{i(\omega-\omega_0)t}\right) \qquad (2.10) \\ i\dot{\tilde{c}}_1 &= V_{01}\tilde{c}_0 e^{i\omega_0 t} = \left(\frac{1}{2}g_{01}(t)e^{-i\omega t} + \frac{1}{2}g_{01}^*(t)e^{i\omega t}\right)\tilde{c}_0 e^{i\omega_0 t} \\ &= \frac{1}{2}\tilde{c}_0\left(g_{01}(t)e^{-i(\omega-\omega_0)t} + g_{01}^*(t)e^{i(\omega+\omega_0)t}\right), \qquad (2.11) \end{aligned}$$

where $g_{ij}(t) \equiv -\mathcal{E}(t)e^{-i\varphi}\langle i|\vec{d}\cdot\hat{\epsilon}|j\rangle \Rightarrow V_{ij} = \frac{1}{2}g_{ij}(t)e^{-i\omega t} + \frac{1}{2}g_{ij}^*(t)e^{i\omega t}$. Integrating this system of equations leads to terms with coefficients of 2 forms, co-rotating terms $\propto 1/(\omega_0 - \omega)$ and counter-rotating terms $\propto 1/(\omega + \omega_0)$. Near resonance, the laser detuning $\Delta = \omega - \omega_0$ is small such that $|\Delta| << \omega_0$ and the counter-rotating terms can be dropped to simplify the solution. This procedure is known as the *Rotating Wave Approximation*. From this simplified model the effective Hamiltonian for the co-rotating coefficients is

$$\begin{aligned} i\begin{pmatrix}\dot{\tilde{c}}_0 \\ \dot{\tilde{c}}_1\end{pmatrix} &= \frac{1}{2}\begin{pmatrix}\tilde{c}_1 g_{01}^*(t)e^{-i\Delta t} \\ \tilde{c}_0 g_{01}(t)e^{i\Delta t}\end{pmatrix} \qquad (2.12) \\ \Rightarrow i\begin{pmatrix}\dot{c}_0 \\ \dot{c}_1\end{pmatrix} &= \frac{1}{2}\begin{pmatrix}g_{01}^*(t)c_1 \\ 2\omega_0 c_1 + g_{01}(t)c_0\end{pmatrix} = \frac{1}{2}\begin{pmatrix}0 & g_{01}^*(t) \\ g_{01}(t) & 2\omega_0\end{pmatrix}\begin{pmatrix}c_0 \\ c_1\end{pmatrix} \qquad (2.13) \\ \Rightarrow \mathcal{H}_{\text{eff}} &= \begin{pmatrix}0 & \frac{1}{2}g_{01}^*(t) \\ \frac{1}{2}g_{01}(t) & \omega_0\end{pmatrix} \qquad (2.14) \\ &= \frac{1}{2}g_{01}(t)\hat{\sigma}_x - \frac{1}{2}\omega_0\hat{\sigma}_z + \frac{1}{2}\omega_0\mathbb{1}, \qquad (2.15) \end{aligned}$$

with $\hat{\sigma}_x, \hat{\sigma}_z$ the x and z Pauli spin operators.

For a constant drive, $g_{01}(t) = g_{01}$ and the initial conditions $c_0(0) = 1$, $c_1(0) = 0$,

and $|c_0|^2+|c_1|^2 = 1$ the differential equation can be simplified and integrated directly:

$$i\dot{\tilde{c}}_0 = \frac{1}{2}\tilde{c}_1 g_{01}^* e^{-i\Delta t} \Rightarrow i\dot{\tilde{c}}_0(0) = 0 \qquad i\dot{\tilde{c}}_1 = \frac{1}{2}\tilde{c}_0 g_{01} e^{i\Delta t} \Rightarrow i\dot{\tilde{c}}_1(0) = \frac{1}{2}g_{01} \tag{2.16}$$

$$i\ddot{\tilde{c}}_0 = \frac{1}{2}e^{-i\Delta t}\left(\dot{\tilde{c}}_1 g_{01}^* - i\Delta\tilde{c}_1 g_{01}^*\right) \qquad i\ddot{\tilde{c}}_1 = \frac{1}{2}e^{i\Delta t}\left(\dot{\tilde{c}}_0 g_{01} + i\Delta\tilde{c}_0 g_{01}\right) \tag{2.17}$$

$$\ddot{\tilde{c}}_0 + i\Delta\dot{\tilde{c}}_0 + \frac{1}{4}|g_{01}|^2\tilde{c}_0 = 0 \qquad \ddot{\tilde{c}}_1 - i\Delta\dot{\tilde{c}}_1 + \frac{1}{4}|g_{01}|^2\tilde{c}_1 = 0 \tag{2.18}$$

$$c_0 = \left(\cos\left(\frac{Wt}{2}\right) + \frac{i\Delta}{W}\sin\left(\frac{Wt}{2}\right)\right)e^{-i\Delta t/2} \qquad c_1 = \frac{g_{01}}{W}\sin\left(\frac{Wt}{2}\right)e^{i\Delta t/2} \tag{2.19}$$

$$\Rightarrow P_{0\to 1} = |c_1|^2 = \frac{|g_{01}|^2}{W^2}\sin^2(Wt/2)\,. \tag{2.20}$$

with $W = \sqrt{|g_{01}|^2 + \Delta^2}$, the generalized Rabi frequency and using the solution

$$\ddot{y}(t) + ia\dot{y}(t) + \frac{b^2}{4}y(t) = 0 \tag{2.21}$$

$$\Rightarrow y(t) = e^{-iat/2}\left(C_1\sin\left(\sqrt{a^2+b^2}\;t/2\right) + C_2\cos\left(\sqrt{a^2+b^2}\;t/2\right)\right). \tag{2.22}$$

2.3 Single-Photon Rabi Frequency

The single photon Rabi frequency can be calculated as follows:

$$g_{ij}(t) = -\mathcal{E}(t)e^{-i\varphi}\langle i|\vec{d}\cdot\hat{\epsilon}|j\rangle = -\mathcal{E}(t)e^{-i\varphi}\langle n',l',j',m_j'|\vec{d}\cdot\hat{\epsilon}|n,l,j,m_j\rangle \tag{2.23}$$

$$= -\mathcal{E}(t)e^{-i\varphi}\sum_q \beta_q\langle n',l',j',m_j'|d_q|n,l,j,m_j\rangle \tag{2.24}$$

$$= -\mathcal{E}_d(t)e^{-i\varphi}\langle n',l',j'||d||n,l,j\rangle\sum_q \beta_q\langle j',m_j',1,q|j,m_j\rangle, \tag{2.25}$$

using the Wigner-Eckart theorem to go from Eq. (2.24) to Eq. (2.25) and q is the spherical component of the electric field's polarization vector. For a given $\{j,j',m_j,m_j'\}$, there will be a single value of q, q', such that $\langle j',m_j',1,q'|j,m_j\rangle \neq 0$. The sum simplifies and defining $\mathcal{E}_d(t) = \beta_{q'}\mathcal{E}(t)$, the complex part of the laser field aligned with $\vec{d}$, the Rabi frequency becomes

$$g_{ij}(t) = -\mathcal{E}_d(t)e^{-i\varphi}\langle j',m_j',1,q'|j,m_j\rangle\langle n',l',j'||d||n,l,j\rangle \tag{2.26}$$

$$= -e^{-i\varphi}\frac{d_{ij}\mathcal{E}_d(t)}{\hbar}C_{ij}, \tag{2.27}$$

where $C_{ij} = \langle j',m_j',1,q'|j,m_j\rangle$, the Clebsch-Gordan coefficients, and $d_{ij} = \langle n',l',j'||d||n,l,j\rangle$, the transition dipole moment.

2.3.1 Selection Rules

As mentioned in the previous section, only one polarization, σ^-, π, σ^+, or one value of $q = -1,\ 0,\ 1$, respectively, will lead to a non-zero Clebsch-Gordan coefficient, namely $q = m'_j - m_j$. Another requirement for the Clebsch Gordan coefficient to be non-zero is $\Delta j = j' - j = 0, \pm 1$. These selection rules can be interpreted as the conservation of angular momentum between the laser photons and the atom. As the atom absorbs a photon, both the photon's momentum, $\hbar k$, and angular momentum, $q\hbar$, are transferred to the atom, resulting in the state change $m'_j = m_j + q$. If the necessary value of m'_j is not a part of the excited state manifold the atom will not interact with the laser and the m_j state is called "dark". For example, a resonant σ^+ polarized beam incident on an atom will drive population from $|^2S_{1/2}\ m_j = -1/2\rangle \rightarrow |^2P_{1/2}\ m_j = 1/2\rangle$, but not from $|^2S_{1/2}\ m_j = 1/2\rangle$ as there is not an $m_j = 3/2$ state in the $P_{1/2}$ manifold, and the $|^2S_{1/2}\ m_j = 1/2\rangle$ is referred to as dark, this is an example of optical pumping (section 2.6).

2.4 Spontaneous Emission

Random vacuum fluctuations cause random emission when the atom is in a state with higher energy than the ground state. The probability density of emission from a state $|j\rangle$ to a lower state $|i\rangle$ is a decaying exponential $P_{ij_{\text{spon}}} = \Gamma_{ij} e^{-\Gamma_{ij} t}$, with the state lifetime defined by $\tau = 1/\Gamma$. Following Fermi's Golden Rule [Ste], the rate of spontaneous emission is

$$\Gamma_{ij} = \frac{d_{ij}^2}{3\pi\epsilon_0 \hbar c^3} (\omega_j - \omega_i)^3. \tag{2.28}$$

Measurements of Γ_{ij} are used to extract the value of d_{ij}.

2.5 Doppler Cooling

Doppler laser cooling is a quintessential technique used to slow and cool trapped ions. The Doppler effect alters the frequency of light the ion interacts with. If the atom is moving away from the laser, the frequency will be shifted down (redder), and the laser frequency will be shifted up (bluer) if the atom is moving toward the

laser. This affects the probability of absorbing a photon from the laser, and so the force on the ions is dependent on the laser detuning, Δ. In cases where the laser frequency is lower than the resonant frequency ($\Delta < 0$), it is referred to as red-detuned. Conversely, when the laser frequency is set higher than the transition resonance the laser is blue-detuned. Red-detuned lasers provide a damping force on the ion. The ion will be more likely to scatter photons when it is moving toward the laser than when it's moving away since the Doppler effect causes the light to shift closer to resonance when the atom is moving toward the red-detuned laser and the light is shifted further from resonance when the ion is moving away from the laser. This preferentially kicks the ion in the opposite direction to its movement, thus reducing its temperature.

2.6 Optical Pumping

To prepare a pure quantum state, carefully tuned laser beams drive population out of all states in a manifold except one, the dark state, by taking advantage of the selection rules (section 2.3.1). After interacting with the laser for a sufficient time, the atom will scatter photons until it lands in the dark state, where it will remain, as it does not interact with the laser beams. This technique is called optical pumping. See section 3.3.2 for more details on how this is implemented in the experiment.

2.7 Relevant Levels

Moving forward, the relevant atomic states will be referred to by the labels and energy levels in Fig. 2.2:

$$|0\rangle \equiv |\,^2S_{1/2}\ m_j = -1/2\rangle \qquad |1\rangle \equiv |\,^2S_{1/2}\ m_j = 1/2\rangle$$
$$|2\rangle \equiv |\,^2P_{1/2}\ m_j = -1/2\rangle \qquad |3\rangle \equiv |\,^2P_{1/2}\ m_j = 1/2\rangle$$
$$|4\rangle \equiv |\,^2P_{3/2}\ m_j = -3/2\rangle \qquad |5\rangle \equiv |\,^2P_{3/2}\ m_j = -1/2\rangle$$
$$|6\rangle \equiv |\,^2P_{3/2}\ m_j = 1/2\rangle \qquad |7\rangle \equiv |\,^2P_{3/2}\ m_j = 3/2\rangle.$$

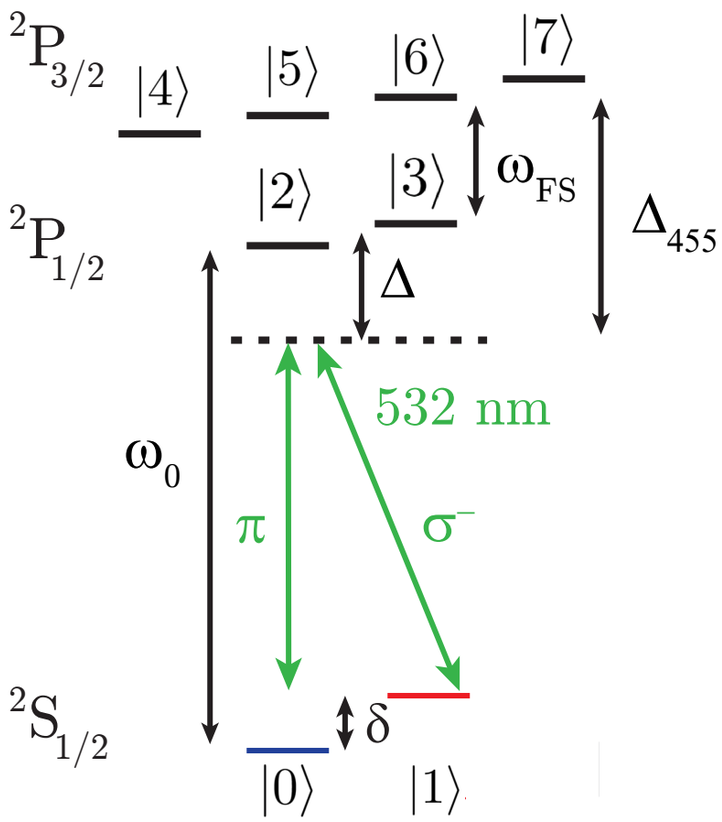

Figure 2.2: Relevant barium ion energy levels for the stimulated Raman transition

2.8 Three-Level Atom

Using the labels in Fig. 2.2, a stimulated Raman transition uses two polarized electric fields to transfer population between two states $|0\rangle$, $|1\rangle$ with energies $E_{|0\rangle} = 0$, and $E_{|1\rangle} = \delta$, through an intermediate state, $|2\rangle$, $E_{|2\rangle} = \hbar\omega_0$.

Eq. (2.6) now expands to 3 equations for 3 levels :

$$
\begin{aligned}
i\dot{\tilde{c}}_0 &= V_{20}\tilde{c}_2 e^{-i\omega_0 t} = \left(\frac{1}{2}g_{02}(t)e^{-i\omega t} + \frac{1}{2}g^*_{02}(t)e^{i\omega t}\right)\tilde{c}_2 e^{-i\omega_0 t} \\
&= \frac{1}{2}\tilde{c}_2\left(g_{02}(t)e^{-i(\omega+\omega_0)t} + g^*_{02}(t)e^{i(\omega-\omega_0)t}\right) \qquad (2.29) \\
i\dot{\tilde{c}}_1 &= V_{21}\tilde{c}_2 e^{-i(\omega_0-\delta)t} = \left(\frac{1}{2}g_{12}(t)e^{-i\omega t} + \frac{1}{2}g^*_{12}(t)e^{i\omega t}\right)\tilde{c}_2 e^{-i(\omega_0-\delta)t} \\
&= \frac{1}{2}\tilde{c}_2\left(g_{12}(t)e^{-i(\omega+\omega_0-\delta)t} + g^*_{12}(t)e^{i(\omega-\omega_0+\delta)t}\right) \qquad (2.30) \\
i\dot{\tilde{c}}_2 &= V_{02}\tilde{c}_0 e^{i\omega_0 t} + V_{12}\tilde{c}_1 e^{i(\omega_0-\delta)t} = \left(\frac{1}{2}g_{02}(t)e^{i\omega t} + \frac{1}{2}g^*_{02}(t)e^{i\omega t}\right)\tilde{c}_0 e^{i\omega_0 t} \\
&\quad + \left(\frac{1}{2}g_{12}(t)e^{-i\omega t} + \frac{1}{2}g^*_{12}(t)e^{i\omega t}\right)\tilde{c}_1 e^{i(\omega_0-\delta)t} \\
&= \frac{1}{2}\tilde{c}_0\left(g_{02}(t)e^{-i(\omega-\omega_0)t} + g^*_{02}(t)e^{i(\omega+\omega_0)t}\right) \\
&\quad + \frac{1}{2}\tilde{c}_1\left(g_{12}(t)e^{-i(\omega-\omega_0+\delta)t} + g^*_{12}(t)e^{i(\omega+\omega_0-\delta)t}\right) \qquad (2.31)
\end{aligned}
$$

Rotating Wave Approximation

$$
\begin{aligned}
i\dot{\tilde{c}}_0 &= \frac{1}{2}\tilde{c}_2\left(g^*_{02}(t)e^{-i\Delta t}\right) \qquad (2.32) \\
i\dot{\tilde{c}}_1 &= \frac{1}{2}\tilde{c}_2\left(g^*_{12}(t)e^{-i(\Delta-\delta)t}\right) \qquad (2.33) \\
i\dot{\tilde{c}}_2 &= \frac{1}{2}\tilde{c}_0\left(g_{02}(t)e^{i\Delta t}\right) + \frac{1}{2}\tilde{c}_1\left(g_{12}(t)e^{i(\Delta-\delta)t}\right) \qquad (2.34)
\end{aligned}
$$

with $\Delta = \omega_0 - \omega$. Assuming $g_{01}(t)$, $g_{02}(t)$, $\tilde{c}_0$, and $\tilde{c}_1$ vary more slowly than $e^{i\Delta t}$, Eq. (2.34) can be directly integrated. This simplification is known as adiabatic elimination. With the initial condition $\tilde{c}_2(0) = 0$:

$$
\tilde{c}_2 = \frac{1}{2\Delta}\tilde{c}_0\left(g_{02}(t)(1-e^{i\Delta t})\right) + \frac{1}{2(\Delta-\delta)}\tilde{c}_1\left(g_{12}(t)(1-e^{i(\Delta-\delta)t})\right). \qquad (2.35)
$$

Plugging this into Eq. (2.32) and Eq. (2.33):

$$
\begin{aligned}
\dot{\tilde{c}}_0 &= \frac{|g_{02}(t)|^2}{4\Delta}\left(e^{-i\Delta t}-1\right)\tilde{c}_0 + \frac{g^*_{02}(t)g_{12}(t)}{4(\Delta-\delta)}\left(e^{-i\Delta} - e^{-i\delta t}\right)\tilde{c}_1 \qquad (2.36) \\
\dot{\tilde{c}}_1 &= \frac{g^*_{12}(t)g_{02}(t)}{4\Delta}\left(e^{-i(\Delta-\delta)t} - e^{i\delta t}\right)\tilde{c}_0 + \frac{|g_{12}(t)|^2}{4(\Delta-\delta)}\left(e^{-i(\Delta-\delta)t}-1\right)\tilde{c}_1. \qquad (2.37)
\end{aligned}
$$

After integration, the above equations will have coefficients of 2 forms, co-rotating terms $\sim 1/\delta$ and counter-rotating terms $\sim 1/\Delta$. While working in the regime $\delta << \Delta \Rightarrow \Delta - \delta \approx \Delta$, the counter-rotating terms will be much smaller than the co-rotating

terms. They will be dropped now to simplify the solution.

$$\dot{\tilde{c}}_0 = -\frac{|g_{02}(t)|^2}{4\Delta}\tilde{c}_0 - \frac{g_{02}^*(t)g_{12}(t)}{4\Delta}e^{-i\delta t}\tilde{c}_1 \tag{2.38}$$

$$\dot{\tilde{c}}_1 = -\frac{g_{12}^*(t)g_{02}(t)}{4\Delta}e^{i\delta t}\tilde{c}_0 - \frac{|g_{12}(t)|^2}{4\Delta}\tilde{c}_1. \tag{2.39}$$

Transforming back to the non-rotating frame, the effective two-level Hamiltonian

$$\dot{c}_0 = -\frac{|g_{02}(t)|^2}{4\Delta}c_0 - \frac{g_{02}^*(t)g_{12}(t)}{4\Delta}c_1 = -\frac{1}{2}\left(2\Delta_{L_0}(t)c_0 + \Omega^*(t)c_1\right) \tag{2.40}$$

$$\dot{c}_1 = -\frac{g_{02}(t)g_{12}^*(t)}{4\Delta}c_0 - \left(\frac{|g_{12}(t)|^2}{4\Delta} + \delta\right)c_1 = -\frac{1}{2}\left(\Omega(t)c_0 + 2(\Delta_{L_1}(t) + \delta)c_1\right) \tag{2.41}$$

$$\Rightarrow \mathcal{H}_{\text{eff}} = -\frac{1}{2}\begin{pmatrix} 2\Delta_{L_0}(t) & \Omega^*(t) \\ \Omega(t) & 2\Delta_{L_1}(t) + 2\delta \end{pmatrix} \tag{2.42}$$

where the two-photon Rabi frequency is defined $\Omega(t) = \frac{g_{02}(t)g_{12}^*(t)}{2\Delta}$, and the light shifts of the $|0\rangle$ state and $|1\rangle$ state, respectively, $\Delta_{L_0}(t) = \frac{|g_{02}(t)|^2}{4\Delta}$, $\Delta_{L_1}(t) = \frac{|g_{12}(t)|^2}{4\Delta}$

2.9 Multiple Beams, Multiple Excited States

Referencing the atomic levels in Fig. 2.2, the energy of the unshifted $^2S_{1/2} \rightarrow {}^2P_{1/2}$ transition is $\hbar\omega_0$; applying an external magnetic field $\vec{B} = B\hat{z}$ causes the states to split due to the Zeeman effect. To first order, the energy shift for each state is $E_{\text{Zeeman}} = \mu_B g_J B m_j = \hbar\omega_B g_J m_j$, giving characteristic frequencies $\omega_{B+} = \omega_B(g_{S_{1/2}} + g_{P_{1/2}})$ and $\omega_{B-} = \omega_B(g_{S_{1/2}} - g_{P_{1/2}})$. For a single beam driving the Raman transition $|0\rangle \rightarrow |1\rangle$ the dynamics of the atomic wavefunction according to Eq. (2.6) is described by the 4 equations:

$$i\dot{\tilde{c}}_0 = e^{-i(\omega_0+\omega_{B-})t}V_{02}\tilde{c}_2 + e^{-i(\omega_0+\omega_{B+})t}V_{03}\tilde{c}_3 \tag{2.43}$$

$$i\dot{\tilde{c}}_1 = e^{-i(\omega_0-\omega_{B+})t}V_{12}\tilde{c}_2 + e^{-i(\omega_0-\omega_{B-})t}V_{13}\tilde{c}_3 \tag{2.44}$$

$$i\dot{\tilde{c}}_2 = e^{i(\omega_0+\omega_{B-})t}V_{20}\tilde{c}_0 + e^{i(\omega_0-\omega_{B+})t}V_{21}\tilde{c}_1 \tag{2.45}$$

$$i\dot{\tilde{c}}_3 = e^{i(\omega_0+\omega_{B+})t}V_{30}\tilde{c}_0 + e^{i(\omega_0-\omega_{B-})t}V_{31}\tilde{c}_1. \tag{2.46}$$

Following the steps from previous solutions, substituting the matrix elements and applying the rotating wave approximation, the equations simplify:

$$i\dot{\tilde{c}}_0 = \frac{1}{2}e^{-i(\Delta+\omega_{B-})t}g_{02}^*\tilde{c}_2 + \frac{1}{2}e^{-i(\Delta+\omega_{B+})t}g_{03}^*\tilde{c}_3 \tag{2.47}$$

$$i\dot{\tilde{c}}_1 = \frac{1}{2}e^{-i(\Delta-\omega_{B+})t}g_{12}^*\tilde{c}_2 + \frac{1}{2}e^{-i(\Delta-\omega_{B-})t}g_{13}^*\tilde{c}_3 \tag{2.48}$$

$$i\dot{\tilde{c}}_2 = \frac{1}{2}e^{i(\Delta+\omega_{B-})t}g_{20}\tilde{c}_0 + \frac{1}{2}e^{i(\Delta-\omega_{B+})t}g_{12}\tilde{c}_1 \tag{2.49}$$

$$i\dot{\tilde{c}}_3 = \frac{1}{2}e^{i(\Delta+\omega_{B+})t}g_{03}\tilde{c}_0 + \frac{1}{2}e^{i(\Delta-\omega_{B-})t}g_{13}\tilde{c}_1, \tag{2.50}$$

Applying adiabatic elimination as above with $\tilde{c}_0,\ \tilde{c}_1,\ g_{02},\ g_{12},\ g_{03},\ g_{13}$ varying much more slowly than $e^{i\Delta t}$, and $\omega_{B+},\ \omega_{B-} << \Delta \Rightarrow \Delta \pm \omega_{B\pm} \approx \Delta$, the solution is a Hamiltonian analogous to Eq. (2.42):

$$\mathcal{H}_{\text{eff}} = -\frac{1}{2}\begin{pmatrix} 2\Delta_{L_0}(t) & \Omega(t) \\ \Omega(t) & 2\Delta_{L_1}(t) + 2\delta \end{pmatrix}, \tag{2.51}$$

with

$$\Omega(t) = \frac{g_{02}^*(t)g_{12}(t)}{2\Delta} + \frac{g_{03}^*(t)g_{13}(t)}{2\Delta}, \tag{2.52}$$

$$\Delta_{L_0} = \frac{|g_{02}(t)|^2}{4\Delta} + \frac{|g_{03}(t)|^2}{4\Delta}, \tag{2.53}$$

$$\Delta_{L_1} = \frac{|g_{12}(t)|^2}{4\Delta} + \frac{|g_{13}(t)|^2}{4\Delta} \tag{2.54}$$

The total Raman Rabi frequency is the sum of the two-photon rabi frequencies for each excited state, and the light shifts due to each excited state also add. Because of the linearity of electric fields, interactions from addition lasers will be linearly added to the interaction matrix elements V_{ij}. For simplicity, the frequency of each beam is the same, ω. With $g_{ij_k}(t)$ the single photon Rabi frequency between states $|i\rangle$ and $|j\rangle$ from beam k, and ω_j the resonant frequency for the transition $|0\rangle \rightarrow |j\rangle$, the general Raman Rabi frequency between nearly degenerate states $|0\rangle$ and $|1\rangle$ as well as the

light shifts:

$$\Omega_{\text{tot}}(t) = \frac{1}{2}\sum_j \frac{1}{\omega-\omega_j}\left(\sum_k g^*_{0j_k}(t)\right)\left(\sum_k g_{1j_k}(t)\right) \tag{2.55}$$

$$\Delta_{L_0} = \frac{1}{4}\sum_j \frac{1}{\omega-\omega_j}\sum_k |g_{0j_k}|^2 \tag{2.56}$$

$$\Delta_{L_1} = \frac{1}{4}\sum_j \frac{1}{\omega-\omega_j}\sum_k |g_{1j_k}|^2 \tag{2.57}$$

$$\Rightarrow \delta_{2\gamma} \equiv \Delta_{L_1} - \Delta_{L_2} = \frac{1}{4}\sum_j \frac{1}{\omega-\omega_j}\left(\sum_k |g_{1j_k}|^2 - |g_{0j_k}|^2\right) \tag{2.58}$$

2.10 Raman Rabi Frequency Calculation

Using the states in Fig. 2.2, and assuming a single beam drives the Raman transition $|0\rangle \rightarrow |1\rangle$, the total Rabi frequency is a sum of the Raman Rabi frequency due to both the $P_{1/2}$ state and the $P_{3/2}$ state,

$$\Omega_{\text{tot}} = \Omega_{2\gamma_0} + \Omega_{2\gamma_{455}} \tag{2.59}$$

$$= \frac{1}{2\Delta}\left(g^*_{02}(t)g_{12}(t) + g^*_{03}(t)g_{13}(t)\right) + \frac{1}{2\Delta_{455}}\left(g^*_{05}(t)g_{15}(t) + g^*_{06}(t)g_{16}(t)\right) \tag{2.60}$$

$$= \frac{d^2}{2\Delta}\left(E^*_\pi E_{\sigma_-} C_{02}C_{12} + E^*_{\sigma_+} E_\pi C_{03}C_{13}\right) + \frac{d^2_{455}}{2\Delta_{455}}\left(E^*_\pi E_{\sigma_-} C_{05}C_{15} + E^*_{\sigma_+} E_\pi C_{06}C_{16}\right), \tag{2.61}$$

with the Clebsch Gordan coefficients as follows:

$$\begin{aligned} C_{02} &= -\sqrt{\frac{1}{3}} \quad C_{03} = -\sqrt{\frac{2}{3}} \quad C_{04} = 1 \quad C_{05} = \sqrt{\frac{2}{3}} \quad C_{06} = \sqrt{\frac{1}{3}} \\ C_{12} &= \sqrt{\frac{2}{3}} \quad C_{13} = \sqrt{\frac{1}{3}} \quad C_{15} = \sqrt{\frac{1}{3}} \quad C_{16} = \sqrt{\frac{2}{3}} \quad C_{17} = 1. \end{aligned} \tag{2.62}$$

A single, circularly polarized beam pointed along $\hat{x}$, with the magnetic field pointed along $\hat{z}$ will have an electric field of the form:

$$\vec{E}(x,y,z,t) = E_0(t)\exp\left(-\frac{z^2}{w_z(x)^2} - \frac{y^2}{w_y(x)^2}\right)\exp\left(-i(\omega t - kx)\right)\hat{\epsilon}, \tag{2.63}$$

and since the size of the atom is much smaller than the wavelength of the light,

$$\vec{E} = \mathcal{E}(t)e^{-i(\omega t+\varphi)}\hat{\epsilon}. \tag{2.64}$$

An arbitrary elliptical polarization can be broken down: $\hat{\epsilon} = a\hat{z} + \sqrt{2}b\hat{y}$, with a real, but b can be imaginary. Using the polarization definitions from spherical basis

on Wikipedia, $\hat{y}$ could be broken down in two ways $\hat{y} = -\frac{1}{\sqrt{2}}(\hat{\sigma}_+ - \hat{\sigma}_-)$, or $\hat{y} = \frac{i}{\sqrt{2}}(\hat{\sigma}_+ + \hat{\sigma}_-)$. Both definitions give the same result, breaking down the polarization using the first definition: $\hat{\epsilon} = a\hat{z} - b(\hat{\sigma}_+ - \hat{\sigma}_-)$, so

$$\overrightarrow{E} = \mathcal{E}(t)(a\hat{z} - b(\hat{\sigma}_+ - \hat{\sigma}_-)) = E_\pi \hat{z} + E_{\sigma_+}\hat{\sigma}_+ + E_{\sigma_-}\hat{\sigma}_- \tag{2.65}$$

$$\overrightarrow{E}^* = \mathcal{E}(t)(a\hat{z} - b^*(-\hat{\sigma}_- + \hat{\sigma}_+)) = E^*_\pi \hat{z} + E^*_{\sigma_+}\hat{\sigma}_+ + E^*_{\sigma_-}\hat{\sigma}_- \tag{2.66}$$

$$E_\pi = \mathcal{E}(t)a \qquad E_{\sigma_+} = -\mathcal{E}(t)b \qquad E_{\sigma_-} = \mathcal{E}(t)b \tag{2.67}$$

$$E^*_\pi = \mathcal{E}(t)a \qquad E^*_{\sigma_+} = -\mathcal{E}(t)b^* \qquad E^*_{\sigma_-} = \mathcal{E}(t)b^*. \tag{2.68}$$

Just focussing on the contribution from the $P_{1/2}$ state for now,

$$\Omega_{2\gamma_0}(t) = \frac{1}{2\Delta}\frac{d^2}{\hbar^2}\left(E^*_\pi E_{\sigma_-} C_{02}C_{12} + E^*_{\sigma_+}E_\pi C_{03}C_{13}\right) \tag{2.69}$$

$$= -\frac{\sqrt{2}}{6\Delta}\frac{d^2}{\hbar^2}\left(E^*_\pi E_{\sigma_-} + E^*_{\sigma_+}E_\pi\right) \tag{2.70}$$

$$= -\frac{\sqrt{2}}{6\Delta}\frac{d^2}{\hbar^2}\left(a\mathcal{E}(t)^2(b - b^*)\right) = -\frac{i\sqrt{2}}{3\Delta}\left(\frac{d\mathcal{E}(t)}{\hbar}\right)^2 \Im(b). \tag{2.71}$$

With the other definition, the polarization is now: $\hat{\epsilon} = a\hat{z} + ib(\hat{\sigma}_+ + \hat{\sigma}_-)$, so

$$\overrightarrow{E} = \mathcal{E}(t)(a\hat{z} + ib(\hat{\sigma}_+ + \hat{\sigma}_-)) = E_\pi \hat{z} + E_{\sigma_+}\hat{\sigma}_+ + E_{\sigma_-}\hat{\sigma}_- \tag{2.72}$$

$$\overrightarrow{E}^* = \mathcal{E}(t)^*(a\hat{z} - ib^*(-\hat{\sigma}_- - \hat{\sigma}_+)) = E_\pi \hat{z} + E^*_{\sigma_+}\hat{\sigma}_+ + E^*_{\sigma_-}\hat{\sigma}_- \tag{2.73}$$

$$E_\pi = \mathcal{E}(t)a \qquad E_{\sigma_+} = i\mathcal{E}(t)b \qquad E_{\sigma_-} = i\mathcal{E}(t)b \tag{2.74}$$

$$E^*_\pi = \mathcal{E}(t)a \qquad E^*_{\sigma_+} = -i\mathcal{E}(t)b^* \qquad E^*_{\sigma_-} = -i\mathcal{E}(t)b^*. \tag{2.75}$$

The contribution to the Rabi frequency from the $P_{1/2}$ state:

$$\Omega_{2\gamma_0}(t) = \frac{1}{2\Delta}\frac{d^2}{\hbar^2}\left(E^*_\pi E_{\sigma_-} C_{02}C_{12} + E^*_{\sigma_+}E_\pi C_{03}C_{13}\right) \tag{2.76}$$

$$= -\frac{\sqrt{2}}{6\Delta}\frac{d^2}{\hbar^2}\left(E^*_\pi E_{\sigma_-} + E^*_{\sigma_+}E_\pi\right) \tag{2.77}$$

$$= -\frac{\sqrt{2}}{6\Delta}\frac{d^2}{\hbar^2}\left(ai\mathcal{E}(t)(b - b^*)\right) = \frac{\sqrt{2}}{3\Delta}\left(\frac{d\mathcal{E}(t)}{\hbar}\right)^2 \Im(b) \tag{2.78}$$

Just a 90° phase shift, same magnitude.

Using the second polarization convention, the $P_{3/2}$ state contribution to the two

beam rabi frequency :

$$\Omega_{2\gamma 455}(t) = \frac{1}{2\Delta_{455}} \frac{d_{455}^2}{\hbar^2} \left(E_\pi^* E_{\sigma_-} C_{05} C_{15} + E_{\sigma_+}^* E_\pi C_{06} C_{16} \right) \tag{2.79}$$

$$\Omega_{2\gamma 455}(t) = \frac{\sqrt{2}}{6\Delta_{455}} \frac{d_{455}^2}{\hbar^2} \left(E_\pi^* E_{\sigma_-} + E_{\sigma_+}^* E_\pi \right) \tag{2.80}$$

$$= -\frac{\sqrt{2}}{3\Delta_{455}} \left(\frac{d_{455}\mathcal{E}(t)}{\hbar} \right)^2 \Im(b). \tag{2.81}$$

The Raman Rabi frequency for any polarization and pointing, making sure the same polarization convention was used to calculated both terms,

$$\Omega_{\text{tot}}(t) = \frac{\sqrt{2}}{6\hbar} \left(\frac{d_{455}^2}{\Delta_{455}} - \frac{d^2}{\Delta} \right) \left(E_\pi^* E_{\sigma_-} + E_{\sigma_+}^* E_\pi \right) \tag{2.82}$$

According to the transition dipole moments from [IS08]

$$d_{455} = \sqrt{2} d \tag{2.83}$$

$$\Rightarrow \Omega_{\text{tot}}(t) = \frac{\sqrt{2}}{6} \frac{d^2}{\hbar^2} \left(\frac{2}{\Delta_{455}} - \frac{1}{\Delta} \right) \left(E_\pi^* E_{\sigma_-} + E_{\sigma_+}^* E_\pi \right) \tag{2.84}$$

$$= \frac{\sqrt{2}}{6\Delta} \frac{d^2}{\hbar^2} \left(\frac{2\Delta}{\Delta - \omega_{\text{FS}}} - 1 \right) \left(E_\pi^* E_{\sigma_-} + E_{\sigma_+}^* E_\pi \right) \tag{2.85}$$

2.11 Differential Light-Shift

Using the transition dipole moments above, $d_{455} = \sqrt{2}d$, the differential light shift is

$$\begin{aligned} \delta_{2\gamma}(t) = \Delta_{L_1}(t) - \Delta_{L_0}(t) &= \frac{1}{4\Delta} \left(|g_{12}|^2 + |g_{13}|^2 - |g_{02}|^2 - |g_{03}|^2 \right) \\ &+ \frac{1}{4\Delta_{455}} \left(|g_{15}|^2 + |g_{16}|^2 + |g_{17}|^2 - |g_{04}|^2 - |g_{05}|^2 - |g_{06}|^2 \right) \end{aligned} \tag{2.86}$$

$$\begin{aligned} = \frac{1}{4\hbar^2} \Bigg(& \frac{d^2}{\Delta} \left(|C_{12} E_{\sigma^-}|^2 + |C_{13} E_\pi|^2 - |C_{02} E_\pi|^2 - |C_{03} E_{\sigma^+}|^2 \right) \\ & + \frac{d_{455}^2}{\Delta_{455}} \Big(|C_{15} E_{\sigma^-}|^2 + |C_{16} E_\pi|^2 + |C_{17} E_{\sigma^+}|^2 \\ & - |C_{04} E_{\sigma^-}|^2 - |C_{05} E_\pi|^2 - |C_{06} E_{\sigma^+}|^2 \Big) \Bigg) \end{aligned} \tag{2.87}$$

$$\begin{aligned} = \frac{d^2}{4\hbar^2} \Bigg(& \frac{2}{3\Delta} \left(|E_{\sigma^+}|^2 - |E_{\sigma^-}|^2 \right) \\ & + \frac{2}{\Delta_{455}} \left(|E_{\sigma^+}|^2 - \frac{1}{3}|E_{\sigma^+}|^2 + \frac{1}{3}|E_{\sigma^-}|^2 - |E_{\sigma^-}|^2 \right) \Bigg) \end{aligned} \tag{2.88}$$

$$= \frac{d^2}{6\hbar^2\Delta} \left(\frac{2\Delta}{\Delta - \omega_{\text{FS}}} + 1 \right) \left(|E_{\sigma^+}|^2 - |E_{\sigma^-}|^2 \right) \tag{2.89}$$

2.11.0.1 Nulling Light Shift

For some laser frequency, ω, the differential light shift will vanish, independent of the laser intensity:

$$\delta_{2\gamma} = 0 = \frac{d^2}{6\hbar^2\Delta}\left(\frac{2\Delta}{\Delta - \omega_{\mathrm{FS}}} + 1\right)\left(|E_{\sigma^+}|^2 - |E_{\sigma^-}|^2\right) \tag{2.90}$$

$$\Rightarrow 0 = \frac{2\Delta}{\Delta - \omega_{\mathrm{FS}}} + 1 = 2\Delta + \Delta - \omega_{\mathrm{FS}} \tag{2.91}$$

$$\Rightarrow 3\Delta = \omega_{\mathrm{FS}} \tag{2.92}$$

$$\omega_{\mathrm{magic}} = \omega_0 + \frac{1}{3}\omega_{\mathrm{FS}}. \tag{2.93}$$

2.12 Rabi Frequency with Perpendicular Beams

When using muliple beams, the optical phase of each needs to be considered when calculating the Rabi frequency. For reference:

$$g_{ij_k} = -e^{-i\varphi_k}\frac{d_{ij}\mathcal{E}_d}{\hbar}C_{ij_k}. \tag{2.94}$$

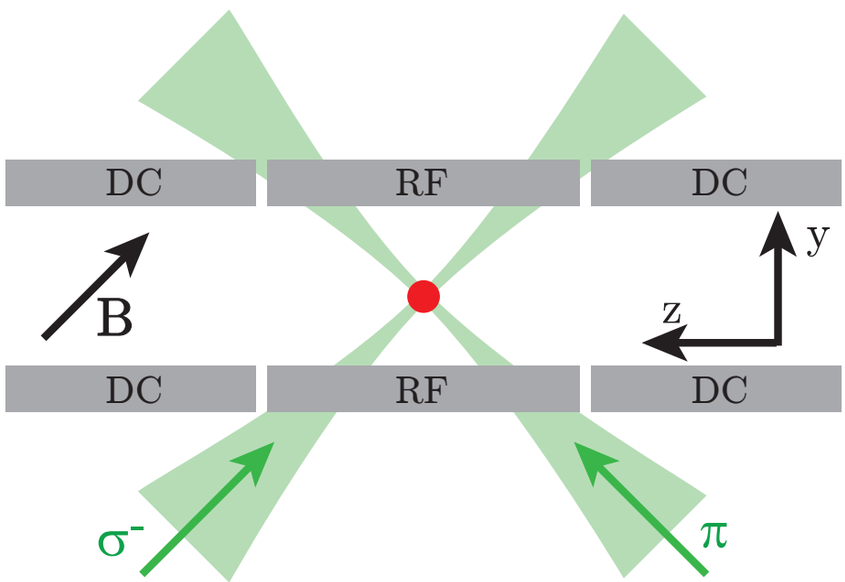

Figure 2.3: SDK laser beam geometry

With the beams shown in Fig. 2.3, which are of the same frequency, but differing k vectors, $\vec{k}_\pi = \frac{1}{\sqrt{2}}k\,(\hat{y} + \hat{z})$ and $\vec{k}_{\sigma^-} = \frac{1}{\sqrt{2}}k\,(\hat{y} - \hat{z})$ and just focusing on the $P_{1/2}$

state, there is no coupling between $|0\rangle$ and $|3\rangle$, and the Rabi frequency follows:

$$\Omega_{2\gamma_0} = \frac{1}{2\Delta}\left(g^*_{02_\pi} g_{12_{\sigma^-}}\right) \tag{2.95}$$

$$= -e^{i\varphi_\pi} e^{-i\varphi_{\sigma^-}} \frac{\sqrt{2}d^2}{6\hbar^2\Delta}\left(E^*_\pi E_{\sigma_-}\right), \tag{2.96}$$

where $\varphi_\pi = -\vec{k}_\pi \cdot \vec{r} + \phi_\pi = -\frac{1}{\sqrt{2}}k\,(y+z) + \phi_\pi$, and $\varphi_{\sigma^-} = -\vec{k}_{\sigma^-} \cdot \vec{r} + \phi_{\sigma^-} = -\frac{1}{\sqrt{2}}k\,(y-z) + \phi_{\sigma^-}$ and therefore the phase difference between the beams varies spatially,

$$\varphi_\pi - \varphi_{\sigma^-} = -\frac{1}{\sqrt{2}}k\,(y+z) + \phi_\pi + \frac{1}{\sqrt{2}}k\,(y-z) - \phi_{\sigma^-} \tag{2.97}$$

$$= -\sqrt{2}kz + \phi_\pi - \phi_{\sigma^-}. \tag{2.98}$$

This gives a spatial variation to the Rabi frequency:

$$\Omega_{2\gamma_0} = -\exp(i\,(\varphi_\pi - \varphi_{\sigma^-}))\frac{\sqrt{2}d^2}{6\hbar^2\Delta}\left(E^*_\pi E_{\sigma_-}\right) \tag{2.99}$$

$$= -e^{i\left(\phi_\pi - \phi_{\sigma^-}\right)} \exp\left(-i\sqrt{2}kz\right) \frac{\sqrt{2}d^2}{6\hbar^2\Delta}\left(E^*_\pi E_{\sigma_-}\right) \tag{2.100}$$

Continuing forward, the beam path lengths are assumed to be the same and the first phase factor goes away. The second phase factor can be seen as a momentum kick. This operation takes place in a harmonic oscillator where the operator $z = z_0\left(a^\dagger + a\right)$, and the phase difference causes a momentum displacement $\mathcal{D}\left(i\eta\right) \equiv \exp\left(i\eta\left(a^\dagger + a\right)\right)$, defining the effective Lamb-Dicke parameter $\eta \equiv \sqrt{2}kz_0$, and including the contribution from the $P_{3/2}$ state in the same way as section 2.10, the Rabi frequency becomes,

$$\Omega_{\text{tot}} = -\frac{\sqrt{2}}{6\Delta}\frac{d^2}{\hbar^2}\left(\frac{2\Delta}{\Delta - \omega_{\text{FS}}} - 1\right)\left(E^*_\pi E_{\sigma_-}\right)\mathcal{D}\left(-i\eta\right) \tag{2.101}$$

$$= \Omega_0 \mathcal{D}(-i\eta). \tag{2.102}$$

The displacement operator acts on the motional state of the ion, leading to a coupling between the internal (spin) state of the ion and its motion.

2.13 Including Motion

The ion trap potential adds to the Hamiltonian $\mathcal{H}_{\text{trap}} = \omega_{\text{trap}}(\hat{n} + 1/2)$ (see section 3.1). During the experiment, the ion is not prepared to a pure Fock state; the

density matrix formulation is needed to calculate expectation values. The Glauber-Sudarshan distribution expresses the density matrix in terms of coherent states $|\alpha\rangle$,

$$\rho = \int \mathrm{d}^2\boldsymbol{\alpha} P_G(\alpha)|\Psi\rangle\langle\Psi|, \tag{2.103}$$

with $\Psi \equiv |\psi, \alpha\rangle = |\psi\rangle \otimes |\alpha\rangle$, and $|\psi\rangle$ the ion's internal state wavefunction. After Doppler cooling the ion is in a thermal state so $P_G(\alpha) = \frac{1}{\pi\bar{n}} e^{-|\alpha|^2/\bar{n}}$, with $\bar{n}$ the mean occupation number, corresponding to the mean motional energy $\bar{E} = \omega_{\mathrm{trap}}\bar{n}$. For an ion in a thermal state with temperature T, $1/\bar{n} = \exp\left(\omega_{\mathrm{trap}}/k_B T\right) - 1$.

2.13.1 Coherent States

The coherent states of a particle with mass, m, in a harmonic oscillator with secular frequency, ω_{trap}, are the eigenfunctions of the annihilation operator a:

$$a|\alpha\rangle = \alpha|\alpha\rangle \tag{2.104}$$

$$|\alpha\rangle = e^{-|\alpha|^2/2} \sum_{n=0}^{\infty} \frac{\alpha^n}{\sqrt{n!}}|n\rangle, \tag{2.105}$$

they aren't orthonormal

$$\langle\alpha|\beta\rangle = e^{-\frac{1}{2}\left(|\alpha|^2+|\beta|^2-2\alpha^*\beta\right)}, \tag{2.106}$$

and their time evolution, with $\omega_{\mathrm{trap}}t = \phi$:

$$|\alpha(t)\rangle = \exp(-iHt)|\alpha(0)\rangle = \exp\left(-i\phi\left(\hat{n} + \frac{1}{2}\right)\right)|\alpha(0)\rangle \tag{2.107}$$

$$= e^{-i\phi(\hat{n}+1/2)} e^{-|\alpha(0)|^2/2} \sum_{n=0}^{\infty} \frac{\alpha(0)^n}{\sqrt{n!}}|n\rangle \tag{2.108}$$

$$= e^{-i\phi/2} e^{-|\alpha(0)|^2/2} \sum_{n=0}^{\infty} \frac{\alpha(0)^n}{\sqrt{n!}} e^{-i\phi\hat{n}}|n\rangle \tag{2.109}$$

$$= e^{-i\phi/2} e^{-|\alpha(0)|^2/2} \sum_{n=0}^{\infty} \frac{\alpha(0)^n}{\sqrt{n!}} e^{-i\phi n}|n\rangle \tag{2.110}$$

$$= e^{-i\phi/2} e^{-|\alpha(0)|^2/2} \sum_{n=0}^{\infty} \frac{(\alpha(0)e^{-i\phi})^n}{\sqrt{n!}}|n\rangle \tag{2.111}$$

$$= e^{-i\phi/2}|\alpha(0)e^{-i\phi}\rangle \tag{2.112}$$

The displacement operators:

$$\mathcal{D}(\beta) = e^{\beta\hat{a}^\dagger - \beta^*\hat{a}} \tag{2.113}$$

$$\mathcal{D}(\beta)|\alpha\rangle = e^{(\alpha^*\beta - \alpha\beta^*)/2}|\alpha+\beta\rangle \tag{2.114}$$

$$\mathcal{D}(i\eta)|\alpha\rangle = e^{(i\eta\alpha^* + i\eta\alpha)/2}|\alpha+i\eta\rangle = e^{i\eta(\alpha^*+\alpha)/2}|\alpha+i\eta\rangle \tag{2.115}$$

$$= e^{i\eta\Re(\alpha)}|\alpha+i\eta\rangle = e^{i\eta\alpha_R}|\alpha+i\eta\rangle \tag{2.116}$$

where $\alpha = \alpha_R + i\alpha_I$ and α_R, α_I are the real and imaginary components of the coherent state, respectively and η is real.

2.13.2 SDK Ramsey Wavefunction Calcluation

The ion state distribution after a $\pi/2$, wait, $\pi/2$ Ramsey sequence given a density matrix ρ and using Eq. (2.103), is calculated

$$P_\uparrow = |\langle\uparrow|\psi\rangle|^2 = \langle\uparrow|\psi\rangle\langle\psi|\uparrow\rangle = \langle\uparrow|\mathrm{Tr}_\alpha(\rho)|\uparrow\rangle = \left\langle \uparrow \left| \frac{1}{\pi}\int d^2\boldsymbol{\beta}\langle\beta|\rho|\beta\rangle \right| \uparrow \right\rangle \tag{2.117}$$

$$= \int d^2\boldsymbol{\beta}\langle\uparrow|\langle\beta|\left(\frac{1}{\pi}\int \mathrm{d}^2\boldsymbol{\alpha} P_G(\alpha)|\Psi\rangle\langle\Psi|\right)|\beta\rangle|\uparrow\rangle \tag{2.118}$$

$$= \int \mathrm{d}^2\boldsymbol{\alpha} P_G(\alpha)\left(\frac{1}{\pi}\int d^2\boldsymbol{\beta}\langle\uparrow,\beta|\psi,\alpha\rangle\langle\psi,\alpha|\uparrow,\beta\rangle\right) \tag{2.119}$$

$$= \int \mathrm{d}^2\boldsymbol{\alpha} P_G(\alpha)\left(\frac{1}{\pi}\int d^2\boldsymbol{\beta}\langle\psi,\alpha|\uparrow,\beta\rangle\langle\uparrow,\beta|\psi,\alpha\rangle\right) \tag{2.120}$$

$$= \int \mathrm{d}^2\boldsymbol{\alpha} P_G(\alpha)\left(\frac{1}{\pi}\int d^2\boldsymbol{\beta}\langle\psi,\alpha|\uparrow\rangle|\beta\rangle\langle\beta|\langle\uparrow|\psi,\alpha\rangle\right) \tag{2.121}$$

$$= \int \mathrm{d}^2\boldsymbol{\alpha} P_G(\alpha)\left(\langle\psi,\alpha|\uparrow\rangle\left(\frac{1}{\pi}\int d^2\boldsymbol{\beta}|\beta\rangle\langle\beta|\right)\langle\uparrow|\psi,\alpha\rangle\right) \tag{2.122}$$

$$= \int \mathrm{d}^2\boldsymbol{\alpha} P_G(\alpha)\langle\psi,\alpha|\uparrow\rangle\,(\mathbb{1})\,\langle\uparrow|\psi,\alpha\rangle \tag{2.123}$$

$$= \int \mathrm{d}^2\boldsymbol{\alpha} P_G(\alpha)\langle\alpha_\uparrow|\alpha_\uparrow\rangle, \tag{2.124}$$

Where $|\alpha_\uparrow\rangle$ is the motional part of the wavefunction entangled with the spin-up state. After optical pumping, the ion is prepared to $|\uparrow\rangle$, and the density matrix is:

$$\rho_i = \int \mathrm{d}^2\boldsymbol{\alpha} P_G(\alpha)|\uparrow,\alpha\rangle\langle\uparrow,\alpha|. \tag{2.125}$$

Subsequent density matrices can be cacluated by evolving the wavefunction according to the time evolution operator.

2.13.2.1 Time Evolution Operator

According to the Schrodinger representation of quantum mechanics, given an initial wavefunction $|\Psi(0)\rangle$, the wavefunction at a later time $|\Psi(t)\rangle$ and be found using the time evolution operator $U(t)$

$$|\Psi(t)\rangle = U(t)|\Psi(0)\rangle, \tag{2.126}$$

where $U(t) = \exp\left(-i\hat{\mathcal{H}}t\right)$, and $\hat{\mathcal{H}}$ is the Hamiltonian of the system. Adding in the motion and using Eq. (2.42) and (2.102), the effective Hamiltonian becomes

$$\mathcal{H}_{\text{eff}} = -\frac{1}{2}\begin{pmatrix} 2\Delta_{L_0} & \Omega_0\mathcal{D}(i\eta) \\ \Omega_0\mathcal{D}(-i\eta) & 2\Delta_{L_1} + 2\delta \end{pmatrix} + \omega_{\text{trap}}\left(\hat{n} + \frac{1}{2}\right). \tag{2.127}$$

Using the identity $e^{i\theta\hat{A}} = \cos(\theta)\mathbb{1} + i\sin(\theta)\hat{A}$, for any operator $\hat{A}$ such that $\hat{A}^2 = \mathbb{1}$, the Hamiltonian can be rewritten:

$$\mathcal{H}_{\text{eff}} = -\frac{\Omega_0}{2}\hat{A} - \hat{\Delta} + \omega_{\text{trap}}\left(\hat{n} + \frac{1}{2}\right), \tag{2.128}$$

With $\hat{\Delta} = \begin{pmatrix} \Delta_{L_0} & 0 \\ 0 & \Delta_{L_1} + \delta \end{pmatrix}$, $\hat{A} = \begin{pmatrix} 0 & \mathcal{D}(i\eta) \\ \mathcal{D}(-i\eta) & 0 \end{pmatrix}$ and $\omega_{\text{trap}}t = \phi$, it can be shown $\hat{A}^2 = \mathbb{1}$ leading to a time evolution operator:

$$U(t) = \exp(-i\hat{\mathcal{H}}t) = \exp\left(i\frac{\Omega_0 t}{2}\hat{A}\right)\exp\left(i\hat{\Delta}t\right)\exp\left(-i\phi\left(\hat{n} + \frac{1}{2}\right)\right) \tag{2.129}$$

$$= \left(\cos\left(\frac{\Omega_0 t}{2}\right)\mathbb{1} + i\sin\left(\frac{\Omega_0 t}{2}\right)\hat{A}\right)\exp\begin{pmatrix} i\Delta_{L_0}t & 0 \\ 0 & i\Delta_{L_1}t + i\delta t \end{pmatrix} e^{-i\phi\left(\hat{n}+\frac{1}{2}\right)} \tag{2.130}$$

$$= \begin{pmatrix} \cos\left(\frac{\Omega_0 t}{2}\right)e^{i\Delta_{L_0}t} & i\sin\left(\frac{\Omega_0 t}{2}\right)\mathcal{D}(i\eta)e^{i(\Delta_{L_1}+\delta)t} \\ i\sin\left(\frac{\Omega_0 t}{2}\right)\mathcal{D}(-i\eta)e^{i\Delta_{L_0}t} & \cos\left(\frac{\Omega_0 t}{2}\right)e^{i(\Delta_{L_1}+\delta)t} \end{pmatrix} e^{-i\phi\left(\hat{n}+\frac{1}{2}\right)} \tag{2.131}$$

Factoring out $e^{i\Delta_{L_0}t}$, using the fact that overall phase factors in the time evolution operator can be dropped as they don't affect the population dynamics, and assuming a vanishing differential light shift, $\Delta_{L_1} - \Delta_{L_0} = 0$, the time evolution operator becomes

$$U(t) = \begin{pmatrix} \cos\left(\frac{\Omega_0 t}{2}\right) & i\sin\left(\frac{\Omega_0 t}{2}\right)\mathcal{D}(i\eta)e^{i\delta t} \\ i\sin\left(\frac{\Omega_0 t}{2}\right)\mathcal{D}(-i\eta) & \cos\left(\frac{\Omega_0 t}{2}\right)e^{i\delta t}, \end{pmatrix} e^{-i\phi\hat{n}} \tag{2.132}$$

For $\Omega_0 t = \pi/2$, a $\pi/2$ pulse, the internal and motional phase factors can be dropped since $\delta, \omega << \Omega_0 \Rightarrow e^{i\delta t}, e^{-i\omega t\hat{n}} \approx 1$,

$$U_{\pi/2} = \frac{1}{\sqrt{2}} \begin{pmatrix} 1 & i\mathcal{D}(i\eta) \\ i\mathcal{D}(-i\eta) & 1 \end{pmatrix}. \tag{2.133}$$

The wavefunction after the first $\pi/2$ pulse is

$$|\Psi_1\rangle = U_{\pi/2}|\uparrow, \alpha\rangle = \frac{1}{\sqrt{2}} \begin{pmatrix} 1 & i\mathcal{D}(i\eta) \\ i\mathcal{D}(-i\eta) & 1 \end{pmatrix} \begin{pmatrix} 0 \\ |\alpha\rangle \end{pmatrix} \tag{2.134}$$

$$= \frac{1}{\sqrt{2}} \begin{pmatrix} i\mathcal{D}(i\eta)|\alpha\rangle \\ |\alpha\rangle \end{pmatrix} = \frac{1}{\sqrt{2}} \begin{pmatrix} ie^{i\eta\alpha_R}|\alpha + i\eta\rangle \\ |\alpha\rangle \end{pmatrix} \tag{2.135}$$

$$= \frac{1}{\sqrt{2}} \left(ie^{i\eta\alpha_R}|\downarrow, \alpha + i\eta\rangle + |\uparrow, \alpha\rangle \right) \tag{2.136}$$

During the wait, the Raman lasers are off, $\Omega_0 = 0$, and the time evolution operator becomes $U_{\text{wait}}(T) = \begin{pmatrix} e^{-i\phi\hat{n}} & 0 \\ 0 & e^{i\delta T}e^{-i\phi\hat{n}} \end{pmatrix}$, with $\phi = \omega T$. The $|\uparrow\rangle$ state picks up a phase $e^{i\theta} = e^{i\delta T}$ and the coherent state evolves according to Eq. (2.112),

$$|\Psi_2\rangle = U_{\text{wait}}(T)|\Psi_1\rangle = \frac{1}{\sqrt{2}} \begin{pmatrix} e^{-i\phi\hat{n}} & 0 \\ 0 & e^{i\delta T}e^{-i\phi\hat{n}} \end{pmatrix} \begin{pmatrix} ie^{i\eta\alpha_R}|\alpha + i\eta\rangle \\ |\alpha\rangle \end{pmatrix} \tag{2.137}$$

$$= \frac{1}{\sqrt{2}} \left(ie^{i\eta\alpha_R}|\downarrow, (\alpha + i\eta)e^{-i\phi}\rangle + e^{i\theta}|\uparrow, \alpha e^{-i\phi}\rangle \right) \tag{2.138}$$

The final $\pi/2$ pulse:

$$|\Psi_f\rangle = U_{\pi/2}|\Psi_2\rangle = \frac{1}{2} \begin{pmatrix} 1 & i\mathcal{D}(i\eta) \\ i\mathcal{D}(-i\eta) & 1 \end{pmatrix} \begin{pmatrix} i|(\alpha + i\eta)e^{-i\phi}\rangle e^{i\eta\alpha_R} \\ e^{i\theta}|\alpha e^{-i\phi}\rangle \end{pmatrix} \tag{2.139}$$

$$= \frac{i}{2}|\downarrow\rangle \otimes \left(e^{i\eta\alpha_R}|(\alpha + i\eta)e^{-i\phi}\rangle + e^{i\theta}e^{i\eta\Re(\alpha e^{-i\phi})}|\alpha e^{-i\phi} + i\eta\rangle \right)$$
$$+ \frac{1}{2}|\uparrow\rangle \otimes \left(e^{i\theta}|\alpha e^{-i\phi}\rangle - e^{i\eta(\alpha_R - \Re(\alpha e^{-i\phi}) - \eta\sin\phi)}|(\alpha + i\eta)e^{-i\phi} - i\eta\rangle \right) \tag{2.140}$$

$$\Rightarrow |\alpha_\uparrow\rangle = \frac{1}{2} \left(e^{i\theta}|\alpha e^{-i\phi}\rangle - e^{i\eta(\alpha_R - \Re(\alpha e^{-i\phi}) - \eta\sin\phi)}|(\alpha + i\eta)e^{-i\phi} - i\eta\rangle \right) \tag{2.141}$$

2.13.2.2 Motional Overlap

$$\langle \alpha_\uparrow | \alpha_\uparrow \rangle = \frac{1}{4}\left(e^{-i\theta}\langle \alpha e^{-i\phi}| - e^{-i\eta(\alpha_R - \Re(\alpha e^{-i\phi}) - \eta\sin\phi)}\langle (\alpha+i\eta)e^{-i\phi} - i\eta| \right)$$
$$\times \left(e^{i\theta}|\alpha e^{-i\phi}\rangle - e^{i\eta(\alpha_R - \Re(\alpha e^{-i\phi}) - \eta\sin\phi)}|(\alpha+i\eta)e^{-i\phi} - i\eta\rangle \right) \quad (2.142)$$
$$= \frac{1}{4}\left(2 - e^{-i\theta}e^{i\eta(\alpha_R - \Re(\alpha e^{-i\phi}) - \eta\sin\phi)}\langle \alpha e^{-i\phi}|(\alpha+i\eta)e^{-i\phi} - i\eta\rangle + c.c \right) \quad (2.143)$$
$$= \frac{1}{2} - \frac{1}{2}Re\left(e^{-i\theta}e^{-i\eta^2\sin\phi}e^{i\eta(\alpha_R - \Re(\alpha e^{-i\phi}))}\langle \alpha e^{-i\phi}|(\alpha+i\eta)e^{-i\phi} - i\eta\rangle \right) \quad (2.144)$$

Using $\langle\alpha|\beta\rangle = e^{-\frac{1}{2}\left(|\alpha|^2+|\beta|^2-2\alpha^*\beta\right)}$, and taking $B = (\alpha+i\eta)e^{-i\phi} - i\eta$, the inner product above simplifies

$$\langle \alpha e^{-i\phi}|(\alpha+i\eta)e^{-i\phi} - i\eta\rangle = \langle A|B\rangle = \exp\left(-\frac{1}{2}\left(|\alpha|^2 + |B|^2 - 2\alpha^* B e^{i\phi} \right) \right) \quad (2.145)$$

$$|B|^2 = ((\alpha^* - i\eta)e^{i\phi} + i\eta)((\alpha+i\eta)e^{-i\phi} - i\eta) \quad (2.146)$$
$$= (\alpha^* - i\eta)(\alpha+i\eta) + i\eta\left((\alpha+i\eta)e^{-i\phi} - (\alpha^* - i\eta)e^{i\phi} \right) \quad (2.147)$$
$$= |\alpha|^2 + 2\eta^2 + i\eta\left(\alpha^* - \alpha + \alpha e^{-i\phi} - \alpha^* e^{i\phi} \right) - \eta^2\left(e^{-i\phi} + e^{i\phi} \right) \quad (2.148)$$
$$= |\alpha|^2 + 2\eta^2(1-\cos\phi) + i\eta\left(\alpha^* - \alpha + \alpha e^{-i\phi} - \alpha^* e^{i\phi} \right) \quad (2.149)$$
$$2\alpha^* B e^{i\phi} = 2\alpha^*\left((\alpha+i\eta)e^{-i\phi} - i\eta \right)e^{i\phi} = 2|\alpha|^2 + 2i\eta(\alpha^* - \alpha^* e^{i\phi}) \quad (2.150)$$

$$\langle A|B\rangle = \exp\left(-\frac{1}{2}\left(|\alpha|^2 + |\alpha|^2 + 2\eta^2(1-\cos\phi) \right.\right.$$
$$\left.\left. + i\eta\left(\alpha^* - \alpha + \alpha e^{-i\phi} - \alpha^* e^{i\phi} \right) - 2|\alpha|^2 - 2i\eta\alpha^* + 2i\eta\alpha^* e^{i\phi} \right) \right) \quad (2.151)$$
$$= \exp\left(-\frac{1}{2}\left(2\eta^2(1-\cos\phi) - i\eta\left(\alpha^* + \alpha - \alpha e^{-i\phi} - \alpha^* e^{i\phi} \right) \right) \right) \quad (2.152)$$
$$= \exp\left(-\eta^2(1-\cos\phi) + i\eta\left(\alpha_R - \Re(\alpha e^{-i\phi}) \right) \right) \quad (2.153)$$
$$(2.154)$$

Plugging back into Eq. (2.144), and using $\Re(\alpha e^{-i\phi}) = \alpha_R\cos\phi + \alpha_I\sin\phi$,

$$\langle \alpha_\uparrow | \alpha_\uparrow \rangle = \frac{1}{2} - \frac{1}{2}Re\left(e^{-i\theta}e^{-i\eta^2\sin\phi}e^{i\eta(\alpha_R - \Re(\alpha e^{-i\phi}))}e^{-\eta^2(1-\cos\phi) + i\eta\left(\alpha_R - \Re(\alpha e^{-i\phi})\right)} \right) \quad (2.155)$$
$$= \frac{1}{2} - \frac{1}{2}e^{-\eta^2(1-\cos\phi)}Re\left(e^{2i\eta(\alpha_R(1-\cos\phi) - \alpha_I\sin\phi)}e^{-i\theta}e^{-i\eta^2\sin\phi} \right) \quad (2.156)$$
$$= \frac{1}{2} - \frac{1}{2}e^{-\eta^2(1-\cos\phi)}\cos\left(2i\eta(\alpha_R(1-\cos\phi) - \alpha_I\sin\phi) - \gamma \right) \quad (2.157)$$

with $\gamma = \theta + \eta^2 \sin\phi$

Now back to the population in $|\uparrow\rangle$ after the SDK Ramsey sequence, using Eq. (2.124) and the integral:

$$\int_{-\infty}^{\infty} \mathrm{d}x\ e^{-x^2/a^2} \cos(bx + c) = a\sqrt{\pi} e^{-b^2 a^2/4} \cos(c) \tag{2.158}$$

$$P_\uparrow = \int \mathrm{d}^2\boldsymbol{\alpha} \left(\frac{1}{\pi\bar{n}} e^{-|\alpha|^2/\bar{n}}\right) \left(\frac{1}{2} - \frac{1}{2} e^{-\eta^2(1-\cos\phi)} \cos\left(2i\eta(\alpha_R(1-\cos\phi) - \alpha_I \sin\phi) - \gamma\right)\right) \tag{2.159}$$

$$= \frac{1}{2} - \frac{1}{2} e^{-\eta^2(1-\cos\phi)} \int \mathrm{d}^2\boldsymbol{\alpha} \left(\frac{1}{\pi\bar{n}} e^{-|\alpha|^2/\bar{n}}\right) \cos\left(2i\eta(\alpha_R - \alpha_R\cos\phi - \alpha_I \sin\phi) - \gamma\right) \tag{2.160}$$

$$= \frac{1}{2} - \frac{e^{-\eta^2(1-\cos\phi)}}{2\pi\bar{n}} \int d\alpha_R d\alpha_I e^{-(\alpha_R^2+\alpha_I^2)/\bar{n}} \cos\left(2i\eta(\alpha_R - \alpha_R\cos\phi - \alpha_I \sin\phi) - \gamma\right) \tag{2.161}$$

$$= \frac{1}{2} - \frac{e^{-\eta^2(1-\cos\phi)}}{2\pi\bar{n}} \int d\alpha_R d\alpha_I e^{-(\alpha_R^2+\alpha_I^2)/\bar{n}} \cos\left(2i\eta(\alpha_R - \alpha_R\cos\phi - \alpha_I \sin\phi) - \gamma\right) \tag{2.162}$$

$$= \frac{1}{2} - \frac{\sqrt{\pi\bar{n}}}{2\pi\bar{n}} e^{-\eta^2(1-\cos\phi)} e^{-\eta^2\bar{n}(1-\cos\phi)^2} \int d\alpha_I e^{-\alpha_I^2/\bar{n}} \cos\left(2i\eta\alpha_I \sin\phi + \gamma\right) \tag{2.163}$$

$$= \frac{1}{2} - \frac{\pi\bar{n}}{2\pi\bar{n}} e^{-\eta^2(1-\cos\phi)} e^{-\eta^2\bar{n}(1-\cos\phi)^2} e^{-\eta^2\bar{n}\sin^2\phi} \cos\left(\gamma\right) \tag{2.164}$$

$$= \frac{1}{2} - \frac{1}{2} e^{-\eta^2(1-\cos\phi)(1+2\bar{n})} \cos\left(\gamma\right) \tag{2.165}$$

$$= \frac{1}{2} - \frac{1}{2} e^{-\eta^2(1-\cos\phi)(2\bar{n}+1)} \cos\left(\theta + \eta^2 \sin\phi\right) \tag{2.166}$$

The probability oscillates as a function of the Ramsey wait time, T, with a periodic, exponential envelope. These oscillations are interference fringes due to the varying phase difference between the $|\uparrow\rangle$ and $|\downarrow\rangle$ states. The amplitude, or the difference between the highest and lowest points, of these oscillations is the fringe contrast,

$$C(T) = \exp\left(-\eta^2(1-\cos\phi)(2\bar{n}+1)\right) \tag{2.167}$$

The contrast is lowest when the Ramsey time is exactly half a trap period,

$$T = T_{\text{trap}}/2 = \pi/\omega_{\text{trap}} \ \Rightarrow\ \phi = \pi \ \Rightarrow\ \sin\phi = 0,\ \cos\phi = -1$$

$$C(T_{\text{trap}}/2) = \exp\left(-2\eta^2(2\bar{n}+1)\right)$$

The contrast is highest when the Ramsey time equals a trap period,

$$T = T_{\text{trap}} = 2\pi/\omega_{\text{trap}} \;\Rightarrow\; \phi = 2\pi \Rightarrow \sin\phi = 0,\; \cos\phi = 1$$

$$C(T_{\text{trap}}) = 1$$

and the usual Ramsey equation is recovered.

$$P_{\uparrow}(T_{\text{trap}}) = \frac{1}{2} - \frac{1}{2}\cos\left(\delta T\right) = \sin^2\left(\delta T/2\right) \tag{2.168}$$

If the timing is close to correct,

$$T \approx T_{\text{trap}} = 2\pi/\omega_{\text{trap}} \;\Rightarrow\; \phi \approx 2\pi$$

$$\Rightarrow \sin\phi \approx \phi - 2\pi = \omega_{\text{trap}}T - \omega_{\text{trap}}T_{\text{trap}} = \omega_{\text{trap}}(T - T_{\text{trap}}) = \omega_{\text{trap}}\delta T$$

$$\cos\phi \approx 1 - (2\pi - \phi)^2/2 = 1 - (\omega_{\text{trap}}\delta T)^2/2,$$

using $\delta T \equiv T - T_{\text{trap}}$. The contrast is now

$$C(T \approx T_{\text{trap}}) = \exp\left(-\eta^2((\omega_{\text{trap}}\delta T)^2/2)(2\bar{n}+1)\right) \tag{2.169}$$

$$= \exp\left(-\delta T^2(\eta\omega_{\text{trap}}\sqrt{2\bar{n}+1})^2/2\right), \tag{2.170}$$

a Gaussian with deviation $\sigma = (\eta\omega_{\text{trap}}\sqrt{2\bar{n}+1})^{-1}$

CHAPTER 3

Experimental Setup

3.1 Ion Trap

3.1.1 Theory

According to Earnshaw's theorem, an oscillating field is needed to trap charged particles. There are a few known ways to do this. The two most prolific are the Penning trap and the Paul trap. Both use quadrupole electric fields, but the ion motion is much more complicated in a Penning trap and it utilizes a strong magnetic field that will cause unwanted Zeeman shifts. The Paul trap uses oscillating electric fields and no magnetic fields. It is typically constructed from 4 segmented, parallel, cylindrical rods, as shown in Fig. 3.1.

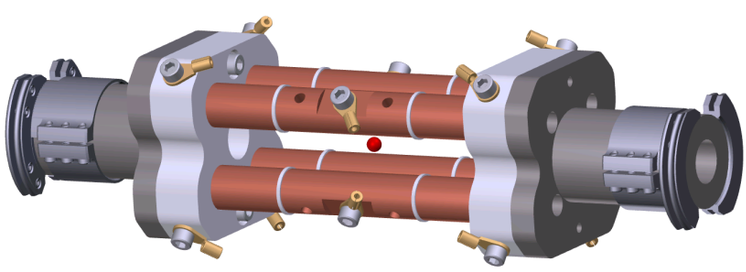

Figure 3.1: CAD drawing of the ion trap

The middle segments provide the oscillating field and the end segments, or endcaps, provide a static DC voltage to confine the ions along the axial direction. A DC voltage, U, on the endcaps, together with an oscillating voltage $V(t) = V_0 \cos(\Omega_T t)$

applied to two diagonal rods creates an approximate potential

$$V(x,y,z,t) \approx \frac{1}{2}V_0\cos(\Omega_T t)\left(1+\frac{x^2-y^2}{r_0^2}\right)+\frac{U}{z_0^2}\left(z^2-\frac{1}{2}\left(x^2+y^2\right)\right) \tag{3.1}$$

Now, the ion's equations of motion will follow Newton's 2^{nd} law

$$\ddot{\vec{x}} = \frac{\vec{F}}{m} = -\frac{e}{m}\nabla V \tag{3.2}$$

$$\Rightarrow \ddot{x}_i = -\frac{\Omega_T^2}{4}\left(a_i - 2q_i\cos\left(\Omega_T t\right)\right)x_i, \tag{3.3}$$

with i the x, y, z components of the position vector $\vec{x}$, and

$$a_x = -\frac{4eU}{mz_0^2\Omega_T^2} \qquad a_y = a_x \qquad a_z = -2a_x \tag{3.4}$$

$$q_x = -\frac{2eV_0}{mr_0^2\Omega_T^2} \qquad q_y = -q_x \qquad q_z = 0 \tag{3.5}$$

Making the change of variables $\xi = \Omega_T t/2$, transforms this equation into the familiar Mathieu equation [Mar97].

$$\frac{d^2x_i}{d\xi^2} + (a_i - 2q_i\cos(2\xi))x_i = 0 \tag{3.6}$$

The solutions are a power series in a_i and q_i. The trap typically operates with $U = 0$ and $eV_0 << mr_0^2\Omega_T^2$, so $a_i, q_i << 1$. This suggests the solution of lowest order in a_i and q_i will be good approximations of the ion's motion. Following [WMI98]:

$$x_i = x_{i_0}\cos\left(\omega_i t + \phi_S\right)\left(1 - \frac{q_i}{2}\cos\left(\Omega_T t + \phi_M\right)\right), \tag{3.7}$$

with x_{i_0}, ϕ_S, and ϕ_M given by initial trapping conditions, and $\omega_i \approx \frac{\Omega_T}{2}\sqrt{a_i + q_i^2/2}$, the trap secular frequencies.

3.1.2 Ion Trap Construction

In order to perform circular orbits during the operation of the gyroscope, the three trap secular frequencies need to be equal. Usually the oscillating fields are much larger than the DC voltage on the endcaps. This leads to a much larger radial secular frequency than the axial secular frequency. In order to keep all the secular frequencies ~ 100 kHz, the trap was designed with rod spacing $r_0 = 1$ cm, trap drive frequency $\Omega_T = 2\pi \times 1$ MHz, and trap voltage of $V_0 \approx 500$ V. The large rod spacing also makes the trap easier to assemble, the ions are easier to load, and allows for

increased optical access. In theory, one would expect $\omega_z = 0$ if $U = 0$, but because of the finite length of the RF segment of the rod, the fringing field provides some confinement in the axial direction. Experimentally, the axial secular frequency is measured $\omega_z \approx 2\pi \times 32$ kHz.

3.1.3 Ablation Loading

To load the ion trap, a Continuum Surelite pulsed Nd:YAG laser is used to ablate a BaO target, similar to [Kni81]. While the laser is firing and the ablation plume is being created, the ion trap voltage is switched off. Once the plume enters the trapping region of the ion trap, the voltage is switched back on. With the laser Q-switch delay set at 285 μs and focusing to a $1/e^2$ waist of 100 μm, a fluence of 650 μJ/(π/2(100 μm)^2) = 4 J/cm^2 is achieved. This configuration yields tens to several hundred trapped ions. To isolate a single ion, the trap voltage is rapidly lowered to a minimal value before being raised again using a computer-controlled toggle. After repeating this process several times, a crystal of a few ions remain. To refine this crystal to a single ion, the low voltage threshold is decreased and the toggling process is continued. The LabVIEW program, *ImageProcessor.vi*, running on the "sagnac_log" computer has been developed to automate this distillation process.

3.2 Vacuum Chamber

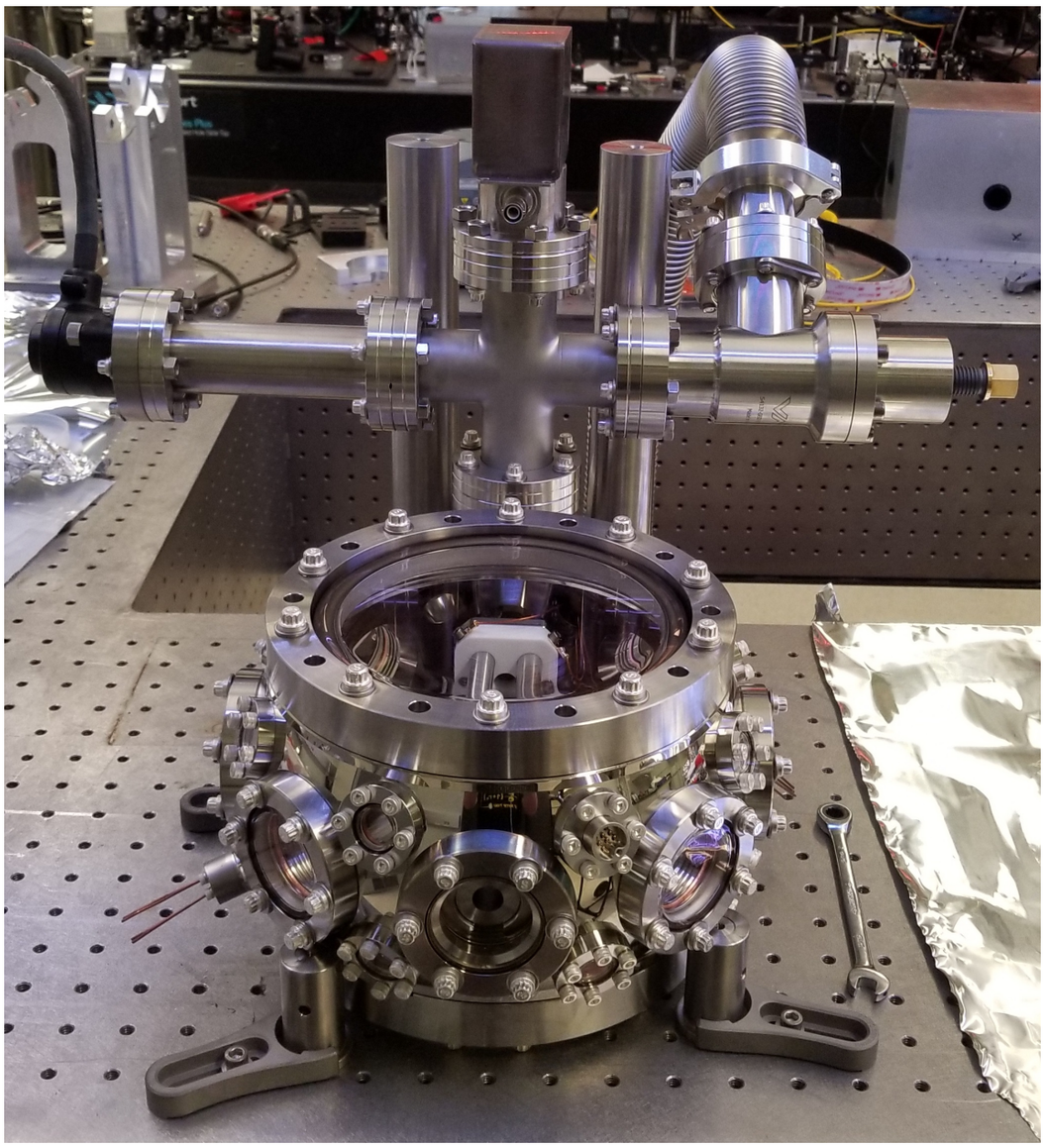

Figure 3.2: Assembled vacuum chamber with the metal bellows to the turbo pump attached.

To ensure the stability of the trapped ions, it is important to minimize collisions with background gases. Neutral molecules are unaffected by the ion trap and can disturb the trapped ions. One common method to avoid these collisions is to cool the entire assembly. This will slow down the neutral molecules so they are less likely to knock the ion out of the trap. The method used in this experiment is to pump out the excess gas to get the chamber down to ultra-high vacuum (UHV) pressures.

3.2.1 Vacuum Parts

All the vacuum parts can be found on the Sagnac BOM spreadsheet in the Hamilton Lab Google Drive, but for ease of access, some of the main parts are listed here:

- 8" octagon: MCF800-ExtOct-G2C8A16 from Kimball Physics
- AR coated viewports: from Larson
- KF and CF clamps, flanges, etc: from Lesker
- Ceramic washers and screws: from Ceramco
- Gamma Vacuum ion pump: 3SCV1V5KNN, from Edwards Vacuum
- Varian Agilent ion gauge: P104144, from Ideal Vacuum
- NEXTorr NEG-ion pump: D 200-5 is from SAES, part number NEXTorr D 200-5.

3.2.2 Chamber Preparation

In order to pump down to UHV pressures, the parts need to be cleaned and the chamber needs to be heated while being pumped down on, also known as baking. Baking releases gases that have been adsorbed into the metal vacuum chamber walls. [SFS17].

3.2.2.1 Cleaning

Cleaning the vacuum parts leads to a lower vacuum pressure by reducing the number of outgassing sources. Most of the vacuum chamber parts were machined and still have residual cutting grease or markings from pens that need to be cleaned off [Rei99]. The procedure used to clean the vacuum parts is as follows:

Note: Gloves should be worn during all parts of the cleaning process to prevent contamination from body oils, hair, and other sources.

1. First, the detergent Alconox was mixed with warm water to create a bath in a sonicator. The solution was heated to 50°C, the parts were placed in, and the sonicator was run for 30 minutes.

2. After the first bath, the parts were rinsed with deionized (DI) water, making sure to rinse out any residual Alconox solution from corners, slots, and especially blind holes. The DI water was wiped off with Kim Wipes and the parts were set on a large sheet of overlapping Kim Wipes to dry overnight.

3. Another bath of pure acetone was prepared to 50°C in the sonicator, the parts were placed in, and the sonicator was run for 30 minutes. The parts were then rinsed and dried as in step 2.

4. A final bath of isoproyl alcohol was prepared at 50°C in the sonicator, the parts were placed in, and the sonicator was run for 30 minutes. The parts were then rinsed and dried as in step 2.

The parts were then carefully wrapped-up and stored in kim wipes until chamber assembly.

3.2.2.2 Baking

Once the chamber was assembled and leak checked, it was heated in a Despatch LAC2-12-4 laboratory heater oven, shown in Fig. 3.3. The whole assembly was baked for about a week at 200°C while being pumped down by a PF70 HiCube turbo pump. The pressure was analyzed with a residual gas analyzer (RGA) until the pressure got low enough to use the ion pump and ion gauge. After the bake, the chamber pressure reached about 3.5e-10 Torr according to the ion pump. One of the ion gauge filaments broke and the ion gauge was not used to measure the vacuum pressure during this bake.

Figure 3.3: Inside of Despatch oven used to bake the vacuum chamber

After the first bake, the chamber was used for about a year, but the pressure had increased, as evidenced by the drastic decrease in ion lifetime. It came to a breaking point when the ion lifetime was getting to be less than a minute. The ion fluorescence data in Fig. 3.4 show that individual ion losses were uncorrelated and short-lived, eliminating issues arising from electrode voltages. It is likely that ion losses were due to collisions with background gasses, so the chamber was re-baked for about a week to lower the vacuum pressure.

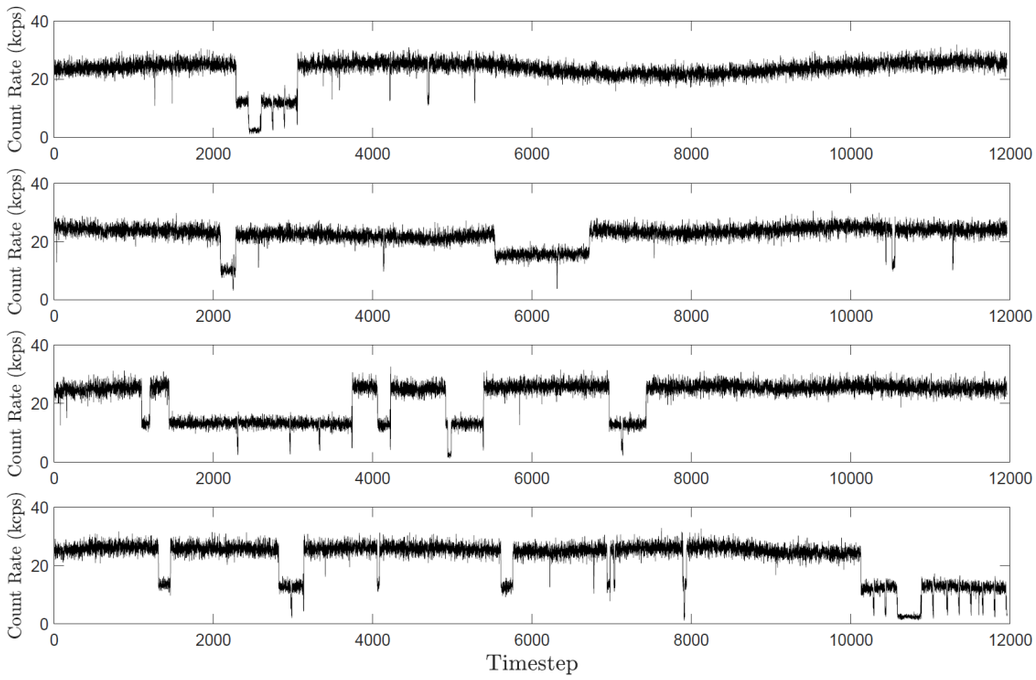

Figure 3.4: Four PMT count rate traces recording the fluorescence of two trapped ions. Dips in the count rate indicate ion loss. It is rare for both ions to go dark simultaneously and the ion are easily recoverable. This is indicative of a non-common loss mechanism.

The procedural steps during the second bake, along with the RGA partial pressures versus time, are depicted in Fig. 3.5.

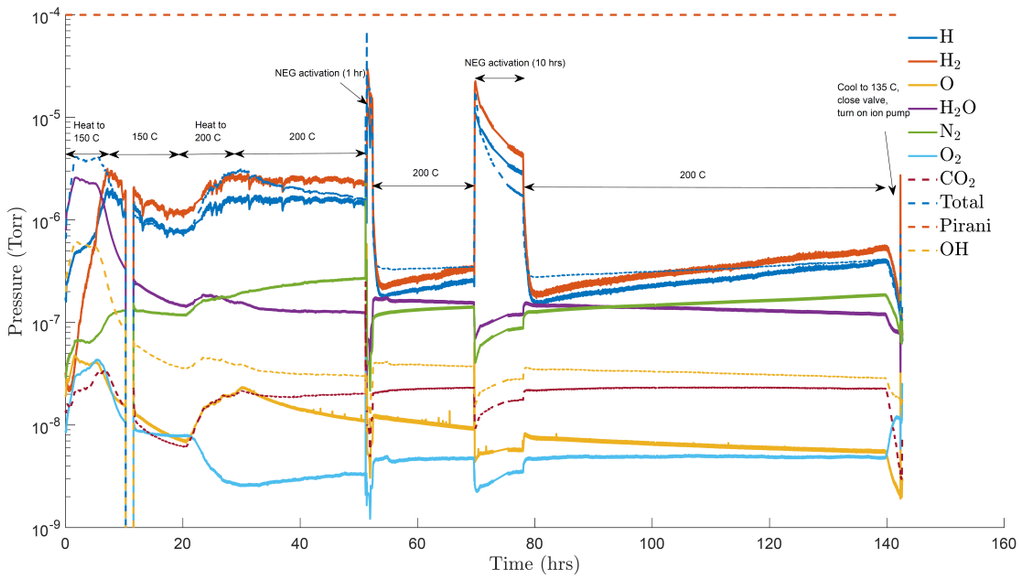

Figure 3.5: Procedural steps and RGA trace over the first 140 hours of the 2nd chamber bake.

At the end of the bake, as the chamber cooled down, the ion pump was turned on. As the pressure decreases below 10s of nTorr, the RGA becomes a less reliable barometer, so the pressure needs to be read with the ion pump. After a few hours the pump reads the minimum pressure of 1.5e-11 Torr, an order of magnitude better than the first bake, but to get an accurate pressure reading the ion gauge should be used.

During the first bake, the ion gauge was turned on towards the end of the bake, it read a fairly high pressure and after about an hour an error appeared on the controller indicating a filament had broken. In order to prevent another broken filament during the second bake, the ion gauge was degassed before turning it on. During the degassing process, the ion gauge ejects diffused gas into the chamber, so a local rise in pressure is expected. Fig. 3.6 shows the ion pump pressure (in black) and ion gauge pressure (in red) during the ion gauge degassing. The data starts on a Wednesday evening, shortly after the initiation of ion gauge degassing. Initially, the pressure in the chamber drops as the gate valve to the turbo is closed, and rises again as the chamber is heated. The ion gauge pressure rises quickly, requiring its

deactivation, while the ion pump pressure rises much more slowly, plateaus, and then starts decreasing. Thursday morning, the ion gauge is fully degassed and the chamber is cooled back down. The ion pump reads its minimum pressure that evening, but eventually creeps back up by Friday morning. Strangely, the ion pump pressure suddenly increased to about 7 nTorr that weekend, while the ion gauge pressure reading was less than 5e-10 Torr. Proceeding with these readings, the ion lifetime was verified to have increased to well over a few hours. During the COVID lockdown, many electronics, including the ion gauge, were turned off in case the lab was to remain vacant for many weeks. The ion gauge had broken once in the first bake, leading to reluctance to turn it back on. Instead, the ion pump is used as a proxy for the vacuum pressure. It consistently reads pressures of a few nTorr, so the ion gauge stays off and the vacuum remains satisfactory.

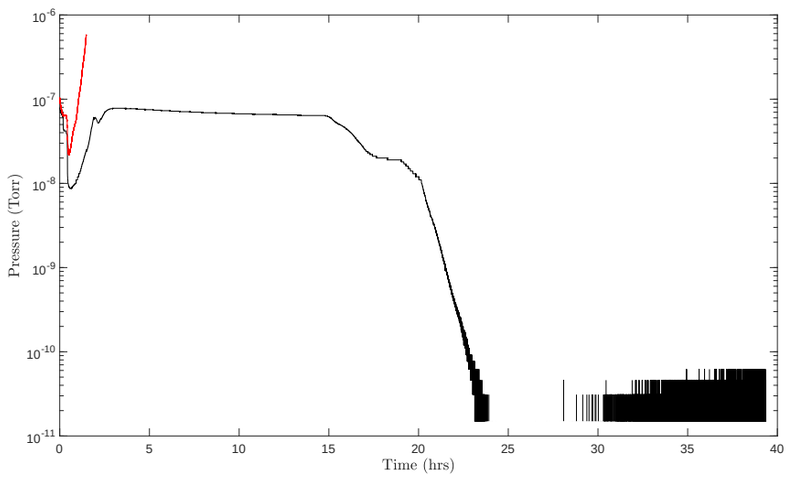

Figure 3.6: Ion pump pressure reading after the final bake and ion gauge degas

3.3 Laser Setups

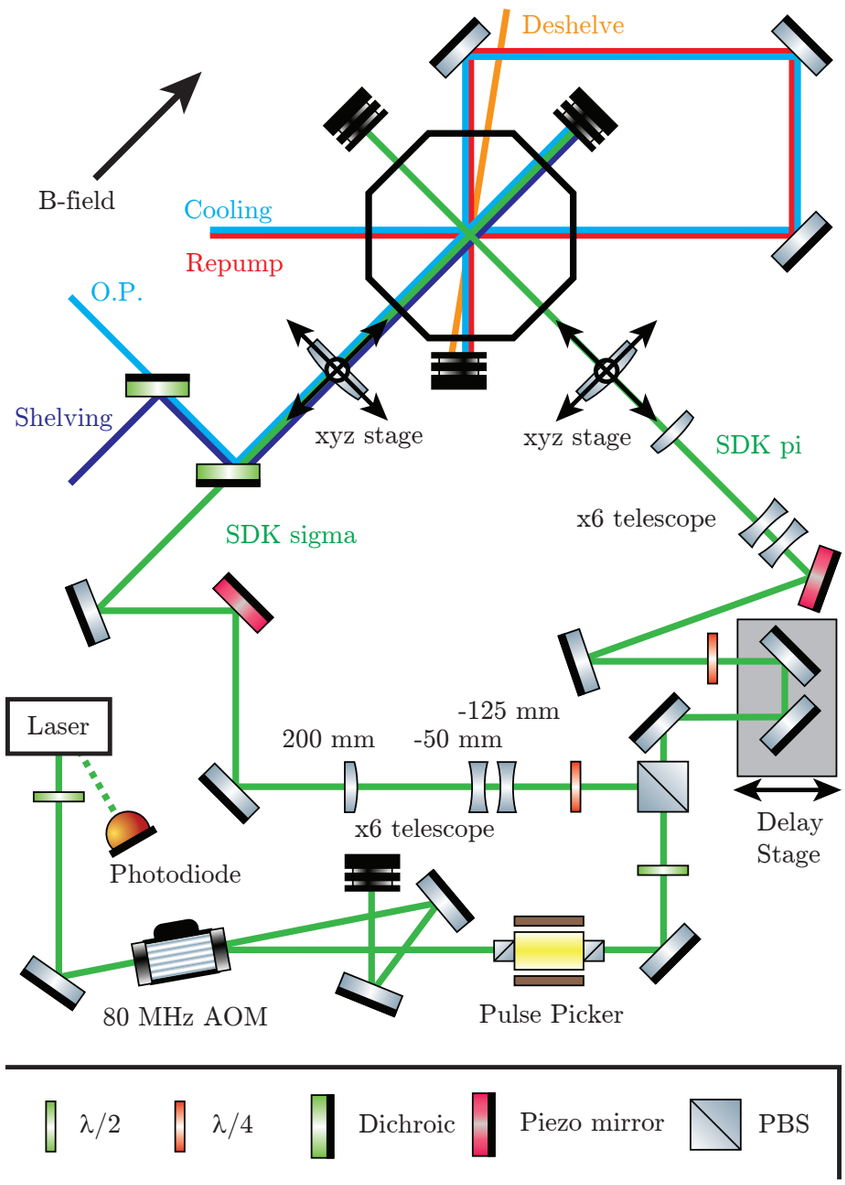

Figure 3.7: Laser setup near the vacuum chamber, showing the beam paths for the cooling, repump, optical pumping, shelving, deshelving, and Raman lasers.

Lasers for cooling, state preparation, state measurement, and Raman transitions need to shine on the ion. Typical laser parameters, EOM, and AOM shifts can be found in the experiment OneNote under the "Lasers" tab. The laser setup going into the vacuum chamber is shown in Fig. 3.7.

3.3.1 Doppler Cooling Lasers

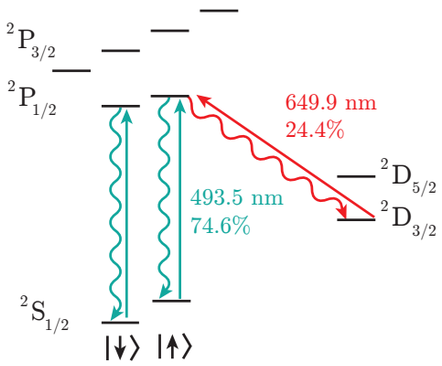

Figure 3.8: Doppler Cooling scheme: The spontaneously emitted 493 nm photons are used for fluorescence measurements.

To Doppler cool the ion as described in Sec. 2.5, two lasers are employed: a 493 nm laser for the primary cooling process, and a 650 nm laser to repump ions from the $D_{3/2}$ state. Both lasers are Toptica DL Pro ECDLs powered by Toptica's DLC pro. This cooling technique follows the $S_{1/2} \leftrightarrow P_{1/2} \leftrightarrow D_{3/2}$ cycle, as illustrated in Fig. 3.8. To efficiently cool the ion over many hours, the light from both lasers is sent through fibers to a wavemeter and a scanning cavity to measure and stabilize the frequency, respectively. Additionally, a portion of the 493 nm light is used for optical pumping. The setups are shown in Figs. 3.9-3.12.

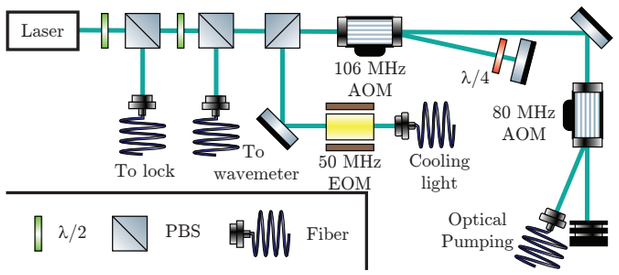

Figure 3.9: Condensed schematic of the 493 nm laser setup.

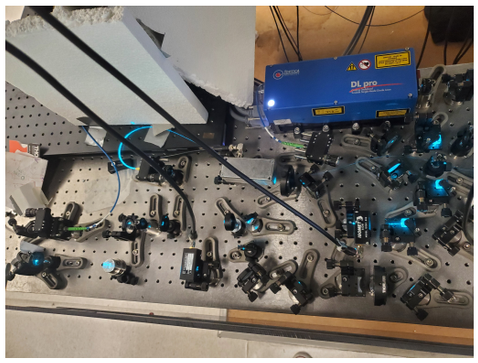

Figure 3.10: Picture of actual 493 nm laser setup

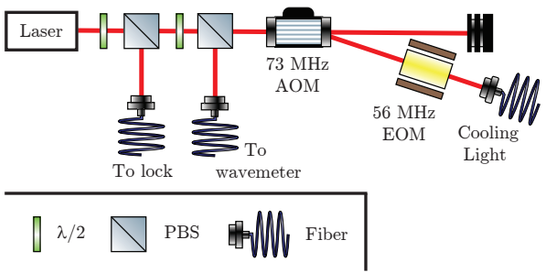

Figure 3.11: Condensed schematic of the 650 nm laser setup.

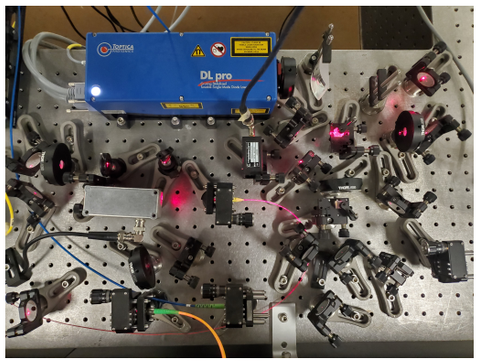

Figure 3.12: Picture of actual 650 nm laser setup

3.3.1.1 Laser Lock

The scanning cavity stabilizes, or locks, the frequencies of the experiment lasers, 493 nm, 650 nm, and 455 nm, the latter's purpose is explained in Sec. 3.3.3. The lock compares the experiment lasers' cavity resonances with the cavity resonances of a reference 633 nm HeNe laser (see Fig. 3.13). A piezoelectric transducer scans the cavity length slightly more than the full 633 nm free spectral range leading to two

transmission peaks from the HeNe laser. Using the known length of the cavity and the number of pixels between the HeNe cavity transmission peaks, the frequency change per pixel for the reference laser is calculated. The frequency per pixel for the experiment lasers is then the reference frequency change per pixel scaled by the ratio of the laser wavelengths. A LabVIEW VI constantly monitors the positions of the cavity peaks and sends voltages to the lasers' piezos. Given the HeNe's passive frequency stability, when the HeNe peaks change position, it is more likely that the cavity length changed (e.g. because the lab temperature changed) rather than the HeNe frequency changing. Therefore, when the HeNe peaks move, it is accounted for by adding an offset voltage to the piezo scan.

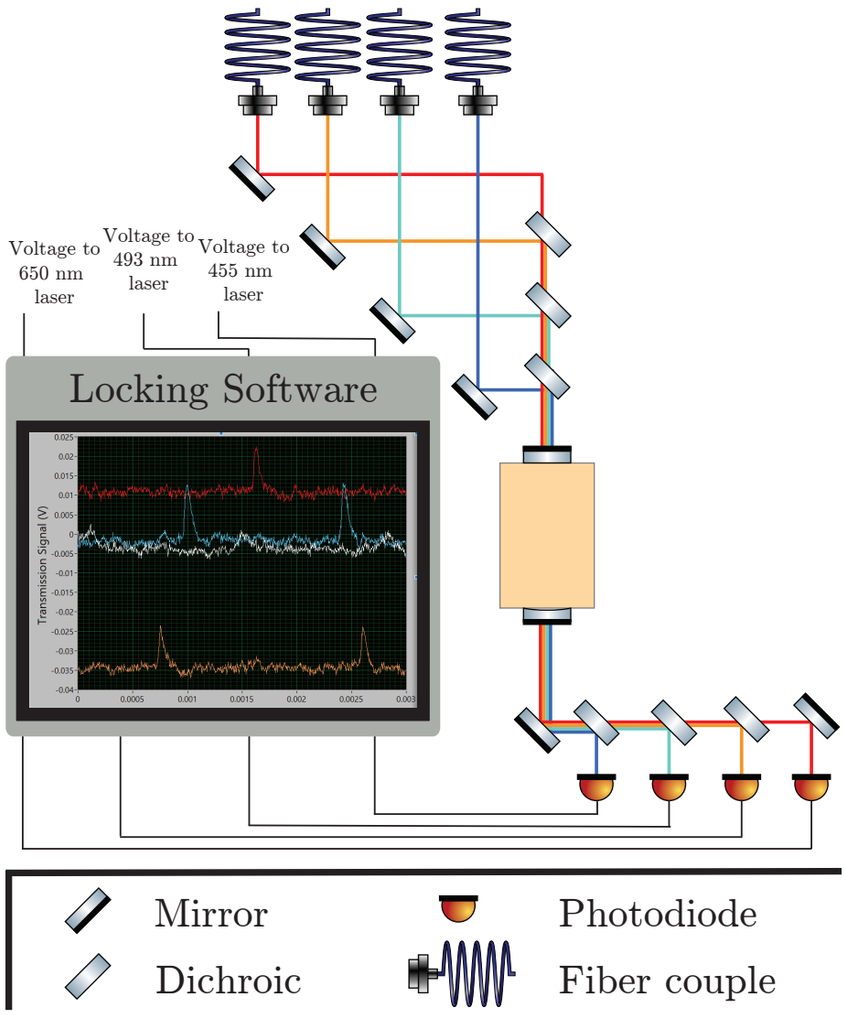

Figure 3.13: Laser locking setup showing the laser light getting sent to the locking cavity before the AOM shifts. The experiment lasers are compared to the stable HeNe laser on a scanning Fabry-Perot cavity. Individual error signals from the locking software control the lasers' piezo voltage to stabilize the laser frequency.

In order to perform meaningful, repeatable experiments, techniques to prepare and measure the state of the ion are needed.

3.3.2 State Preparation

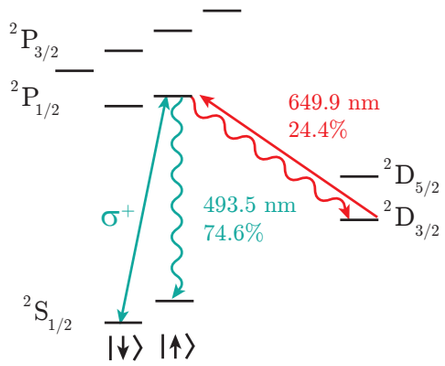

Figure 3.14: Optical Pumping scheme: Using a σ^+ polarized 493 nm beam and a 650 nm repump beam will pump the ion into the $|\uparrow\rangle$ state.

As shown in Fig. 3.14, a pure state is prepared using a σ^+ polarized 493 nm beam to optically pump the ion to $|\uparrow\rangle$ (see Sec. 2.6). The only transition that can be driven with σ^+ light is $|\downarrow\rangle \rightarrow |P_{1/2}, m_j = 1/2\rangle$. It is also ~ 50 MHz $> 2\Gamma_{493}$ away from any other transitions, so the optically pumped state is sensitive to both polarization and frequency.

3.3.3 State Measurement

Detecting the ion state involves two steps, first, shelving, Fig. 3.15 then fluorescence measurement, Fig. 3.8. During the fluorescence measurement, 493 nm and 650 nm cooling beams are applied, fluorescent 493 nm photons are then detected with the imaging setup described below. If fluorescence is observed, the ion state must have been in the $|\downarrow\rangle$, or bright, state. After shelving, if no fluorescence is observed then it must have been the case that the ion was in the $|\uparrow\rangle$, or dark, state and is now in the $D_{5/2}$ manifold, which does not interact with the cooling lasers.

3.3.3.1 Shelving

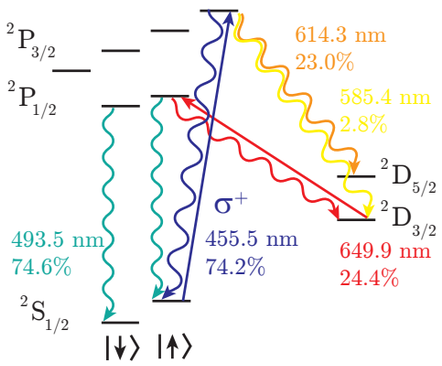

Figure 3.15: Shelving Scheme: 455 nm and 650 nm lasers are used to transfer the ion to the $D_{5/2}$ state.

To shelve, a σ^+ polarized 455 nm shelving beam and the 650 nm repump beam are applied until >99% of the $|\uparrow\rangle$ population is moved out of the $S_{1/2}$ manifold. Most of the population ends up in the $D_{5/2}$ manifold, which has a lifetime of about 30 seconds, during which the $|\downarrow\rangle$ population can be manipulated without addressing the $|\uparrow\rangle$ population which has now been moved to the shelved state.

The 455 nm light is generated by a home-built, Littrow ECDL, shown in Fig. 3.17. The diode is an OSRAM PLT-450B and is current controlled with an SRS LDC501 Laser Diode Controller, the SRS controller also maintains the laser diode temperature using a thermistor for temperature measurements and a TEC to cool or heat a metal plate under the diode. A piezo is used to control the grating angle for fine wavelength tuning. The beam path of the 455 nm laser is similar to that of the cooling lasers, some of the light is picked off to the wavemeter and some to the scanning cavity. The experiment light is switched using an AOM in double pass configuration, see Fig. 3.16.

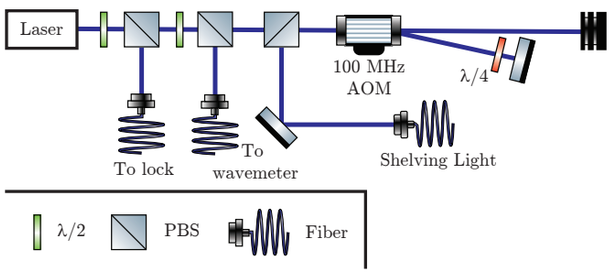

Figure 3.16: Condensed schematic of the 455 nm laser setup.

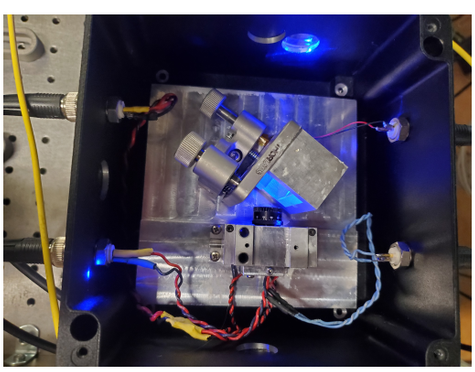

Figure 3.17: Picture of actual 455 nm laser setup

3.3.3.2 Fluorescence Imaging

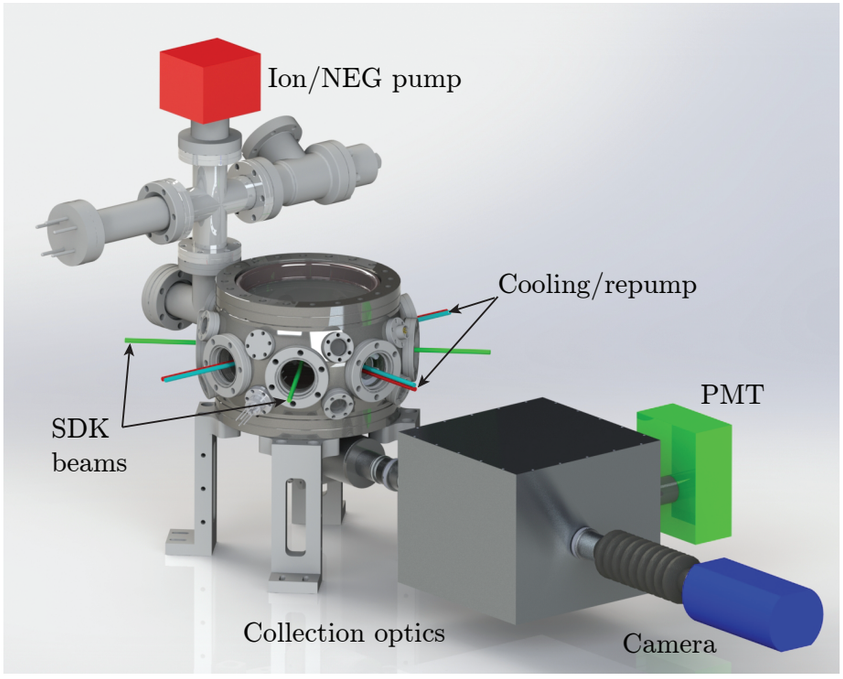

Figure 3.18: Rendering of the ion trap apparatus with the fluorescence collection optics shown in relation to the vacuum chamber.

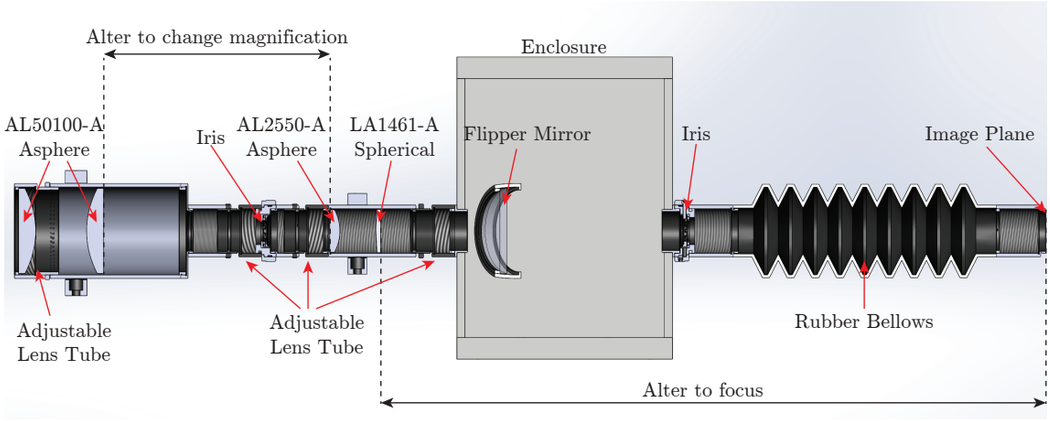

Figure 3.19: Cross-section of the imaging setup.

While the ion is being Doppler cooled it isotropically and spontaneously emits 493 nm photons. This fluorescence is collected through the bottom window of the vacuum chamber, as seen in Fig. 3.18 and is used to give insight on the ion's motional and internal state. Fig. 3.19 shows a more detailed, cross-section view of the fluores-

cence collection optics. Not shown is the elliptical mirror that redirects the emitted fluorescence to enable a horizontal layout for the imaging optics. The first two aspheres have large NA to efficiently collect the fluorescent photons. An iris acts as a spatial filter at the focus of the 2nd asphere. The next two lenses magnify and recollimate the light to be imaged on either a camera or a photomultiplier tube (PMT). A flipper mirror in the beamline allows switching between the two photodetectors. More details can be found in the document written by Adam West, it is linked in the "Imaging" tab in the experiment OneNote. The PMT used in fluoresence detection is the Hamamatsu H12386-210 and the current camera for imaging ions is the Thorlabs CS2100M-USB sCMOS camera. sCMOS cameras are a relatively new technology to be used in imaging atomic physics experiments; typically, an EM-CCD camera is used to quickly image the low light levels of a single fluorescing ion.

At first, the Rolera EM-C^2 EM-CCD camera was used to image the ions. When deciding on a scientific camera, there is a trade-off between cost and performance, on one end are the superb Andor EM-CCD cameras which come with a price tag greater than $10000 and require a special PCI card. The Rolera EM-C^2 was found on eBay for $2800. It worked well for years until the power supply stopped working; it was replaced, but the camera would turn off unprompted and wouldn't reliably turn back on. While a solution was being put together, a Thorlabs sCMOS camera was borrowed from the barium lab next door. It worked well, and a similar one was bought for the experiment. Table 3.1 compares the specifications of both cameras. On paper, the EM-C^2 seems better because of the higher SNR, but in reality, having the extra illuminated pixels when using the Thorlabs camera seemed to make micromotion compensation more precise and the hit to SNR didn't affect the ease of loading.

Single Ion Imaging					
Ion Size: 1231.5 μm^2		Exposure: 250 ms		Photon Flux: 60 kHz	
		Rolera		Thorlabs	
Dark current/px	I_D	0.06		20	
Dark shot noise/px	σ_D	0.12		2.24	
Read noise/px	σ_R	< 1		20	
Quantum efficiency (%)	QE	45		56	
Pixel size (μm^2)	d^2	64		25.4	
		Bright	Dark	Bright	Dark
Filled pixels	P	19	0	48	0
Signal/px	S	351	0	173	0
Shot noise/px	σ_s	18.7	0	13.2	0
Total noise/px	σ_{tot}	18.8	< 1	13.4	2.4
Signal-to-noise ratio/px	SNR	18.7	0	12.9	0

Table 3.1: Comparison of Rolera and Thorlabs camera specifications.

3.3.4 Deshelving

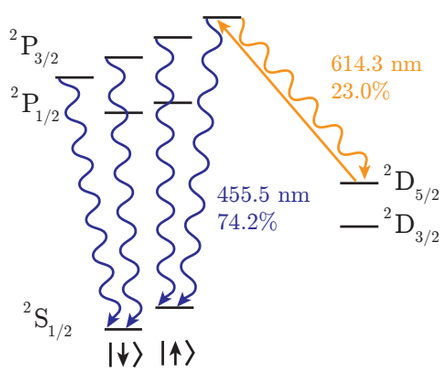

Figure 3.20: 614 nm light from the doubled gain chip ECDL moves the ion population from the $D_{5/2}$ manifold to the $P_{3/2}$ manifold, where it quickly decays back down to the $S_{1/2}$ manifold.

To take multiple experiments in a row, the ion needs to quickly return to the ground state, relying on spontaneous emission out of the $D_{5/2}$ state is too slow. As shown in Fig. 3.20, a 614 nm beam is applied to drive population from the $D_{5/2}$ manifold to the $P_{3/2}$ manifold, from where it will quickly fall back to the ground state manifold. The beam is applied until >99% of the population is moved into the $S_{1/2}$ manifold. The 614 nm light is generated by doubling the ouput of a 1228 nm Littrow ECDL, shown in Fig. 3.21. The 1228 nm "diode" is actually a gain chip, which is quite similiar to a diode, but is more sensitive to feedback and can usually generate higher powers. The 1228 nm light is doubled with an AdvR RSH-T0614-P98P63AL3 frequency doubler.

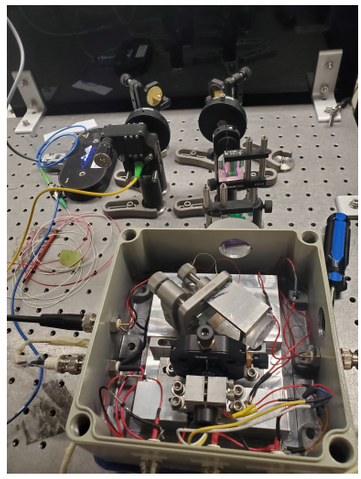

Figure 3.21: Setup for the doubled 1228 nm ECDL.

3.3.5 Raman Laser

Achieving fast momentum transfer to the ion requires a large Rabi frequency, necessitating high laser intensities. This can be accomplished with a pulsed laser, where the instantaneous intensity is much larger than a continuous-wave (CW) laser with the same time-averaged power. To generate such high intensities the Paladin SCAN-532-36000, a doubled, mode-locked, ND:YVO_4 laser is used. It is specified to output a Gaussian beam of 532 nm laser pulses at a 76 MHz repetition rate with a time-averaged power of 36 W. Each pulse is vertically polarized with a FWHM duration of less than 24 ps.

3.3.5.1 Passive Mode-Locking

Mode-locked lasers use saturable absorbers in the laser cavity with the gain crystal to generate pulsed light, the Paladin uses a saturable Bragg reflector (SBR). The intensity-dependent transmission of the SBR preferentially allows high-intensity light to circulate in the cavity. At first, the highest intensities will be from noise spikes, but as the light circulates in the cavity these spikes get preferentially transmitted by the SBR and amplified by the gain crystal. After a sufficient number of round trips, all the power in the cavity will be concentrated in a single pulse.

The theoretical electric field envelope from a passively mode-locked laser is $E_{1064}(t) = E_0 \operatorname{sech}(t/\tau) \Rightarrow I(t)_{1064} = \frac{E_0^2}{2Z_0} \operatorname{sech}^2(t/\tau)$ [Sie86]. The Paladin light is doubled, so the output intensity shape used for the experiment is $I_{532}(t) \propto I(t)^2_{1064} \propto \operatorname{sech}^4(t/\tau)$. In order to find the pulse width, τ, an intensity autocorrelation was performed following slide 19 in [Lab]. The analysis assumes a $\operatorname{sech}^2(1.76t/\tau_{\mathrm{FWHM}})$ pulse shape, which is also consistent for a $\operatorname{sech}^4(t/\tau)$ pulse shape since $\operatorname{sech}^2(x) \approx \operatorname{sech}(\frac{\pi}{2}x)$, and $\tau_{FWHM} = 1.76\tau$. The corresponding pulse bandwidth is then $\Delta f = 0.315/\tau_{\mathrm{FWHM}}$. The autocorrelation measurement yielded a pulse width of $\tau_{FWHM} = 16.4(5)$ ps, or a bandwidth of $\Delta f = 19.2$ GHz.

3.3.5.2 Pulse Shape Effects

The pulse shape changes the probability of transition derived in Sec. 2.20. From Rosen and Zener [RZ32], with a pulse of pulse area $\theta = \int \mathrm{d}t'\ \Omega(t')$, shape $\Omega(t) = \Omega_0 \operatorname{sech}(\pi t/\tau') = \Omega_0 \operatorname{sech}^2(2t/\tau') = \Omega_0 \operatorname{sech}^2(1.76t/\tau_{\mathrm{FWHM}})$, driving a transition $|0\rangle \rightarrow |1\rangle$ with splitting δ (the angular kind), the probability of transition after the pulse now becomes

$$P_{0\to1} = \sin^2\frac{\theta}{2}\operatorname{sech}^2\delta\tau'/2 = \sin^2\frac{\theta}{2}\operatorname{sech}^2(\delta\tau_{\mathrm{FWHM}}/1.76) \tag{3.8}$$

In order to get high population transfer, the pulse bandwidth should be much larger than the level splitting. As described in Sec. 2.11, high-intensity pulses can introduce a differential light shift between the levels, potentially decreasing transfer efficiency. While taking measures to minimize these effects, complete compensation remains as work for future endeavors. When the differential shift is negligible or sufficiently

minimized, the dominant splitting of $\delta = 2\pi \times 150$ MHz arises from the magnetic field-induced Zeeman effect. The max population transfer is near complete:

$$\text{sech}^2\left(\delta\tau_{\text{FWHM}}/1.76\right) = \text{sech}^2\left((2\pi \times 150 \text{ MHz})(16.4 \text{ ps})/1.76\right) = 0.9999; \tag{3.9}$$

3.3.5.3 Pulse Picker

The Conoptics 350-160-LA-AR@532 pulse picker is able to reliably transmit a target single laser pulse, while attenuating the remaining pulses. This is accomplished by placing a Pockels cell between two polarizers. Under normal circumstances no voltage is applied to the Pockels cell such that it does not affect the beam. The polarizers are turned perpendicular to one another so that light will be attenuated through the device. A voltage on the Pockels cell allows for transmission of a pulse as the Pockels cell rotates the polarization of light to allow it through the second polarizer. This voltage is controlled with the Conoptics 25D power supply and triggered using the LeCroy ArbStudio 1100 arbitrary function generator along with high frequency TTL comparators. The pulse patterns can be quite complex, as shown in Fig. 3.22, where reflections from the BNC cable can also be seen. The pulse picker used in these experiments utilizes polarizing beam splitters as the polarizers, allowing the "rejected" light to also be used for experiments. As shown in Fig. 3.23, the rejected light from the pulse picker is used to drive Raman transitions with a tunable, co-propagating beam.

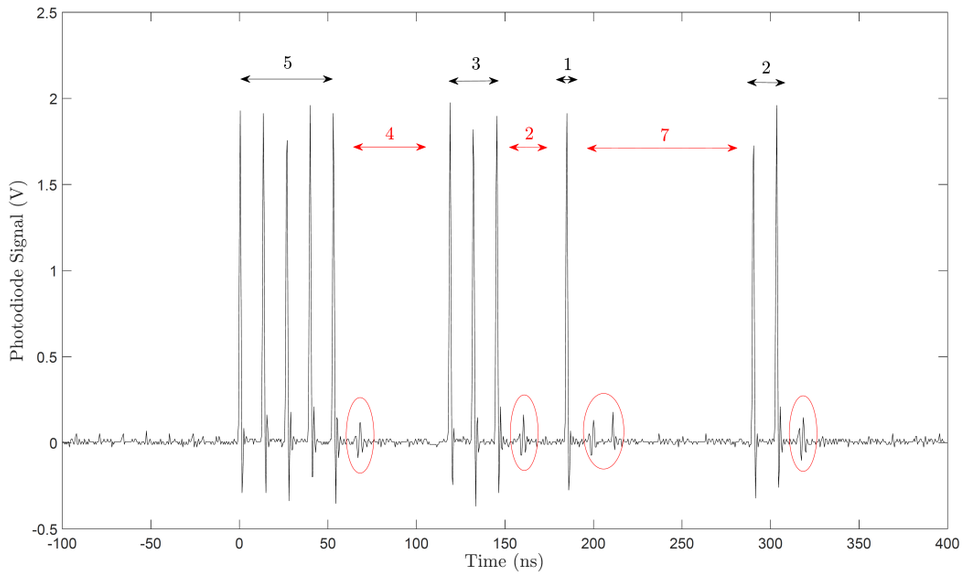

Figure 3.22: Pulse picker transmission detected on a Thorlabs DET20AFC: the arbitary function generator allows for complex pulse picking patterns. Circled pulses are from reflection in the BNC cable. Pulse heights only appear to be different due to the sampling of the oscilloscope.

3.3.5.4 Raman Laser Setup

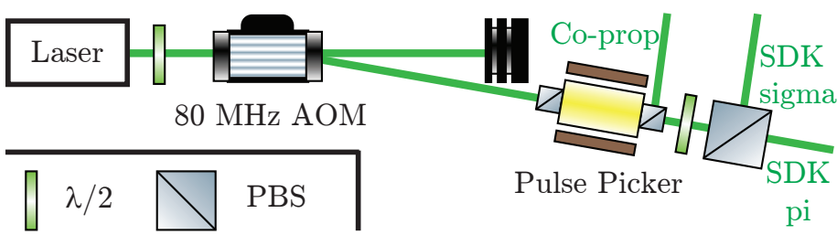

Figure 3.23: Condensed Raman laser setup

The light from the Paladin laser is split between two functions, the co-propogating beam and the sdk beams, as shown in Fig. 3.23.

3.3.5.5 Co-Propogating beam setup

Note: This setup is no longer in use. Exercise extreme caution when reviving this system. The co-propagating beam is engineered to tunably drive the Raman

transition without imparting momentum to the ion. The co-propagating setup is shown in Fig. 3.24, with measured power losses. A single beam is split into two paths. Each path gets its own frequency shift to tune the beatnote frequency. A delay stage is used to ensure the pulses in each beam are temporally overlapped when being recombined.

The co-propagating beatnote frequency can be tuned to drive the Raman transition when the qubit splitting is not an inteteger multiple of the reprate. The beatnote frequency is tuned using two AOMs set up in a double-pass configuration. The double-pass configuration is important to maintain the spatial overlap of the beams while shifting the AOM drive frequency. The first AOM divides the initial beam into two distinct paths: the diffracted portion is retroreflected for a second pass through the AOM and redirected by the PBS towards the delay stage. The undiffracted part is similarly processed by the second AOM, albeit with an opposite frequency shift.

To ensure temporal overlap of the two paths, two moveable mirrors allow for coarse path length adjustments. A delay stage in one of the paths is used for finer control. The beams are recombined with a PBS before being directed to a focusing lens and into the vacuum chamber.

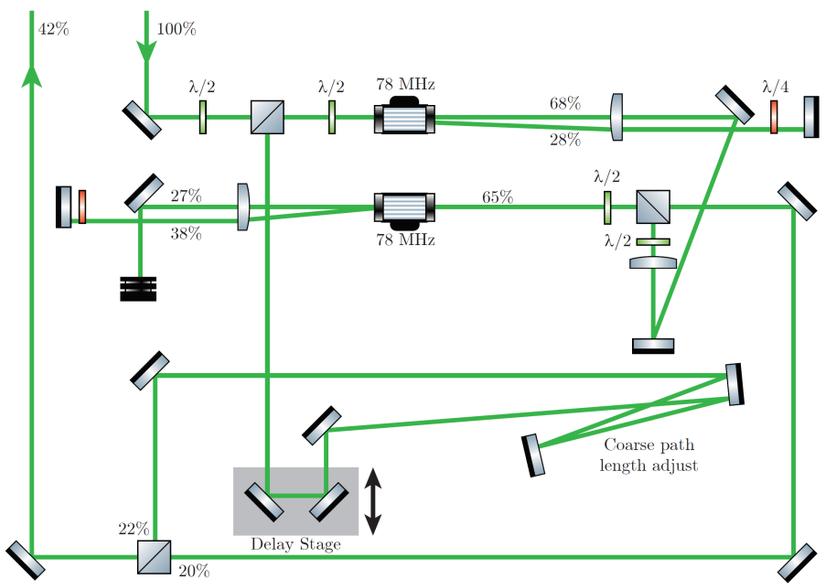

Figure 3.24: Co-propagating Raman laser setup showing power losses as a percentage of the input power.

3.3.5.6 SDK Beams Setup

The second function is the SDK, which requires perpendicular σ- and π-polarized beams, as described in Sec. 2.12. The SDK beams' paths, labeled "SDK sigma" and "SDK pi", are shown in Fig. 3.7. A polarizing beam splitter divides the primary beam into two distinct paths. Within each path, a $\lambda/4$ waveplate controls the beams' polarizations. Each beam is directed onto the ion using its respective focusing objective lens. Before these objective lenses, a telescope in each path expands the beam, achieving a reduced beam waist at the focus. Both focusing objective lenses are mounted on an xyz stage, primarily for precise longitudinal positioning due to the tight beam focus. While the xyz stage provides some focal adjustments, finer transverse beam pointing is achieved using a Polaris-K1S2P piezo-controlled mirror in each beam path. These electronic controls enable quick, precise scanning across the beam profile to pinpoint the focus.

In the current setup configuration, the sigma-beam path telescope is placed before the piezo mirror, whereas for the pi-beam path, the telescope follows the piezo mirror. This arrangement was primarily determined by table space constraints. Notably, having the telescope after the piezo mirror results in a more pronounced focus shift by the piezo compared to the configuration where the telescope precedes the piezo.

Calibration of the piezo mirrors is performed by redirecting the beam post-objective lens and positioning an Arducam 1080P IMX219 USB Camera at the focus. By applying a voltage to the piezo mirror and observing the beam's displacement on the camera, the calibration, in terms of µm of movement per volt on the piezo, is obtained. The current calibration for the piezo mirrors is [Placeholder for Calibration Data].

CHAPTER 4

Experimental Control

4.1 OK Board

An integrated pulse sequencer and RF generator unit were developed for use in atomic physics experiments [PK15]. The unit's core is the XEM6010 FPGA from Opal Kelly and a breakout board for outgoing TTL and RF signals, so the unit is referred to as the "OK Board". The OK Board synchronously generates TTL pulse sequences to trigger devices, reconfigures and outputs RF signals generated by on-board Direct Digital Synthesis (DDS) chips, and collects time-tagged photon counts from a photomultiplier tube (PMT). An on-board 100 MHz oscillator sets the timing resolution for operations. The PMT time-tagging takes full advantage of the oscillator frequency and has a timing resolution of 10 ns. The FPGA counter only increments once every four cycles of the oscillator, so the TTL triggers have a 40 ns resolution. The DDS programming takes a relatively long time, so the minimum timestep when switching DDS amplitudes is 500 ns. Switching the frequency takes even longer and the timestep shouldn't be less than 1 µs.

4.2 LabVIEW

Many LabVIEW VIs were developed to control and analyze the numerous devices in the lab. Only the *main_control.vi* program will be touched on in this section; a more detailed document is available in the lab files.

4.2.1 *main_control.vi*

In order to run experiments with the necessary timing control, the LabVIEW VI, *main_control.vi*, was developed. It triggers and writes pulse sequences to the OK

Board FPGA and DDSs while sending serial or ethernet commands to various devices. The front panel includes buttons to start and stop scans as well as several tabs. Most of the tabs are used to configure scans, while others offer manual controls used for device testing and troubleshooting. The variables used in the scans and variables setting device parameters get saved to .txt files in the "ExperimentData/LabviewVIs/Main Control" folder or corresponding subfolder and are loaded using the *INIT.vi* subVI when *main_control.vi* starts. Experimental data is also saved in .txt format in the "ExperimentData/PMTData" folder or corresponding subfolder and can be viewed using the VI *data_browser.vi*.

4.3 Laser Controllers

All the lasers need controllers for their temperature and current. Additionally, the ECDLs need piezo controllers.

The TOPTICA lasers are each controlled with a DLC Pro laser controller; the temperature, current, and piezo setpoints can be changed in the TOPAS software. The piezo voltage can also be varied with a NI DAQ BNC-2110, which outputs feedback voltages according to *lock_with_monitoring.vi* when the lasers are locked. A LabJack is also used to ramp the piezo voltages during ion loading.

The pulsed lasers have a complex heat management system using a chiller. These laser temperatures and currents were set by the manufacturer for the current calibration and should not be changed.

The two home-built lasers, 455 nm and 1228 nm, have a piezo controller built by the Physics Electronic Shop to vary the piezo voltage. The 455 nm laser has a single thermoelectric cooler (TEC) to stabilize the diode temperature which is controlled by an SRS LDC501 diode controller, which also controls the diode current. The 1228 nm laser has two TECs: one to maintain the gain chip temperature and another for the base plate. Both are controlled with the TECPak 585-04-08 Arroyo temperature controller. The 1228 nm laser current controller was built by the Physics Electronics shop.

To quickly switch laser beams on and off, the AOMs in Table 4.1 are used. All the

AOM RF signals are generated by the OK Board DDSs, gated using a Mini-Circuits ZASWA-2-50DRA+ TTL-controlled RF switch, amplified with a Mini-Circuits ZHL-3A or similar, before finally driving the AOM.

AOM purpose	**Model #**
493 nm cooling	Isomet 1206C -833
493 nm OP and 650 nm cooling	IntraAction ATM-802DA1
455 nm shelving	IntraAction ATM-1002DA1
614 nm deshelving	Brimrose TEM-250-50-614
All 3 Raman beam AOMs	IntraAction ASM-802B47

Table 4.1: Experiment AOM list.

4.4 Additional Controllers

- A TPI-1001-B RF synthesizer is used as a 2 GHz frequency reference for the OK Board DDSs. It just needs a USB connection to the computer for power and communication and is controlled with *TPI_control.vi*.

- The ion trap voltage controllers were built by the Physics Electronic shop. The RF voltages are generated by a large unit, the "MOTion box". Two smaller electronic boxes sitting near the chamber supply the DC voltages. The voltages are controlled with *electrode_control.vi*

- Two Novatech 409B DDSs generate RF signals for applications that require less precise timing control. Right now, one of the Novatechs provides RF to the cooling beam EOMs to efficiently cool the additional lines created by the large Zeeman splitting when running the experiment. The other Novatech controls an RF signal on one of the trap rods which is used to measure the ion secular frequency by way of "tickling" [VVE90]. The Novatech signals are controlled by the VI *Novatech 409B control.vi* and get amplified by a Mini-Circuits ZHL-3A or similar but don't use RF switches.

- A Power-One HCC5-6/OVP-AG linear AC-DC power supply is wired up to a

BNC breakout board outputting +5 V on the top row, and -5 V on the bottom row. This supply provides power for a number of devices and circuits: the PMT, laser piezo voltage adder circuit, line triggering circuit, and the Q-switch signal inverter, schematics in the OneNote "Electronics/Schematics" tab.

- Two HP power supplies, HP 6643A and HP 6553A, are wired up to a two-row BNC breakout board to output +15 V on the top row and +24 V on the bottom row, respectively. These supplies are mostly used to power RF amplifiers.

- Two more power supplies, HP 6683A and Agilent 6624A, are used to drive current in the main magnetic field coils and shim coils, respectively. The top and side coil are no longer being used. The latest calibration suggests a differential shift of the qubit states by 1.179 MHz/A and 1.439 MHz/A for the main and shim coil respectively.

- The piezo mirrors for steering the SDK beams are controlled using a piezo controller built by the Physics Electronic Shop. The voltages can be varied using the *piezo_mirror_control.vi* VI. The *main_control.vi* VI sends ethernet commands to *piezo_mirror_control.vi* when running scans, so make sure the VI is running if you want to do a piezo scan.

- As described in Sec. 3.3.5.3, the pulse picking sequence is controlled by a LeCroy ArbStudio 1100 arbitrary function generator. The electronic setup is shown in Fig. 4.1. The ArbStuidio is externally clocked to the laser's repetition rate by a fast photodiode detecting laser pulses from an auxiliary output port on the laser. Because of the finite speed of light, the ArbStudio clock signal is delayed relative to the laser oscillator by an amount set by the distance the light travels to the photodiode and the red cable length shown in Fig. 4.1. In the same way, the pulse sequence to the pulse picker will be delayed by the blue cable length. The red and blue cable lengths can be varied to set the delay time between the laser pulses and the pulse picker trigger voltage. The ArbStudio pulse sequence is controlled using the *arbstudio_control.vi*.

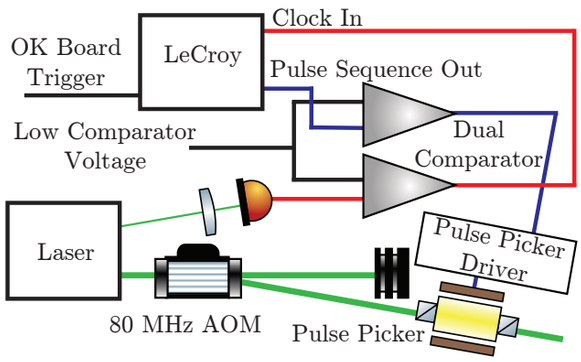

Figure 4.1: The electronic schematic for clocking the ArbStudio and driving the pulse picker.

CHAPTER 5

Results

Basically all the raw data is PMT fluorescence measurements. By thresholding the count rate, the population, or how frequently the ion is in the $|\downarrow\rangle$ or $|\uparrow\rangle$ state, is deduced. The main control VI saves the variables used in the scan and the PMT data in a .txt file. Matlab code is then used to parse and extract the data for analysis.

5.1 Trapping

5.1.1 Micromotion Compensation

To ensure efficient loading of the trap as discussed in Sec. 3.1.3, it's crucial for the ion's equilibrium position to be at the null of the RF field produced by the trapping rods. Construction imperfections and stray external electric fields can displace the ion from this ideal position. When positioned away from the null, the ion is subject to pronounced fluctuations from the trapping RF field, leading to substantial micromotion, increased temperature, and greater variability in ion loss during the distillation process. To counteract these influences, DC voltages are applied to the trap rods. Although various methods can achieve this compensation, the most effective strategy identified involved reducing the trap RF voltage from the max DDS value of 0.7 V to 0.4 V or lower while observing the ion's movement on the camera. As the RF voltage is lowered, stray fields shift the ion further from the null; the compensating DC voltages are then adjusted to realign the ion to its optimal position. This procedure is iterated since the applied DC voltages slightly alter the high voltage position as well. The process continues until the DDS voltage is lowered to 0.1 V and the ion position remains consistent with that seen at the higher voltage.

5.1.2 Secular Frequency Matching

Secular frequencies are matched by measuring them through a technique known as "tickling", followed by adjustments to the trap voltages to make the frequencies degenerate. "Tickling" is a method that applies an oscillating electric field to one of the trap rods. When the frequency of this oscillating field aligns with a secular frequency, it induces oscillation in the ion, leading to reduced fluorescence.

The standard configuration of the ion trap operates at the peak RF voltage, corresponding to a DDS value of 0.7 V. No additional voltages are applied to the rods, save for compensations for stray fields. This setup results in an axial secular frequency of approximately 32 kHz and radial frequencies near 90 and 100 kHz. Experimental adjustments to the RF voltages successfully matched all three secular frequencies to within 1 kHz, as depicted in Fig. 5.1 and outlined in the .

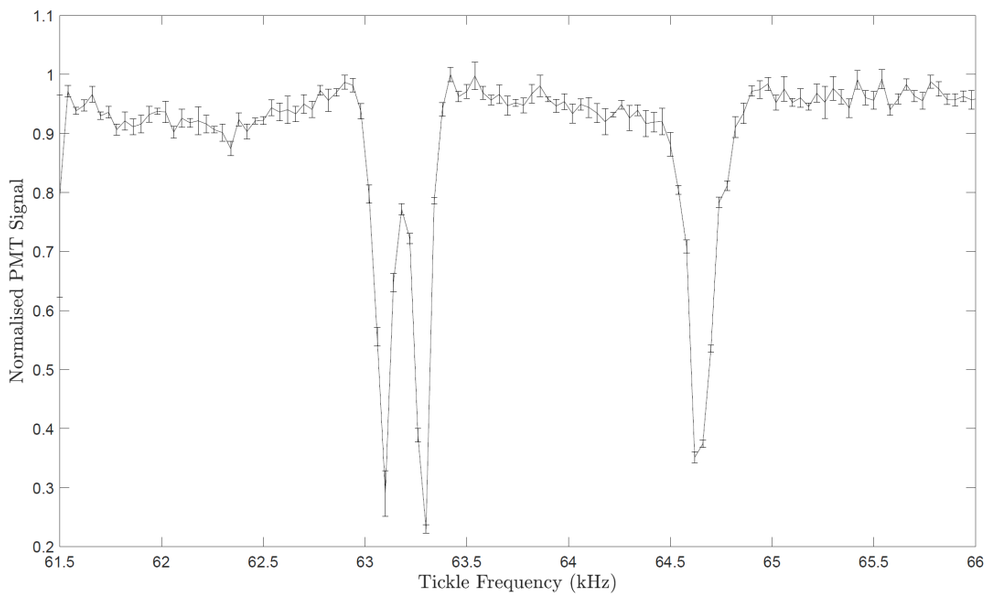

Figure 5.1: Secular frequencies matched to within 1 kHz of 64 kHz

5.2 State Preperation and Measurement

To effectively shelve the $S_{1/2},\ m_j = 1/2$ state, the 455 nm laser needs to be σ^+ polarized and resonant with the $S_{1/2},\ m_j = 1/2 m_j = 1/2 \rightarrow P_{3/2},\ m_j = 3/2$

transition. With a magnetic field of ≈ 55 G, the eight $S_{1/2} \rightarrow P_{3/2}$ transitions are split by about 50 MHz, only the stretched transitions are prominent in the scan, as shown in Fig. 5.2 where the shelving beam was linearly polarized in order to see the other transition resonances. Adding in a σ^+ polarized 493 nm beam pumps the ion to the $S_{1/2},\ m_j = 1/2$ state, and the $S_{1/2},\ m_j = -1/2 \rightarrow P_{3/2},\ m_j = -3/2$ transition is no longer driven, as shown in Fig. 5.3.

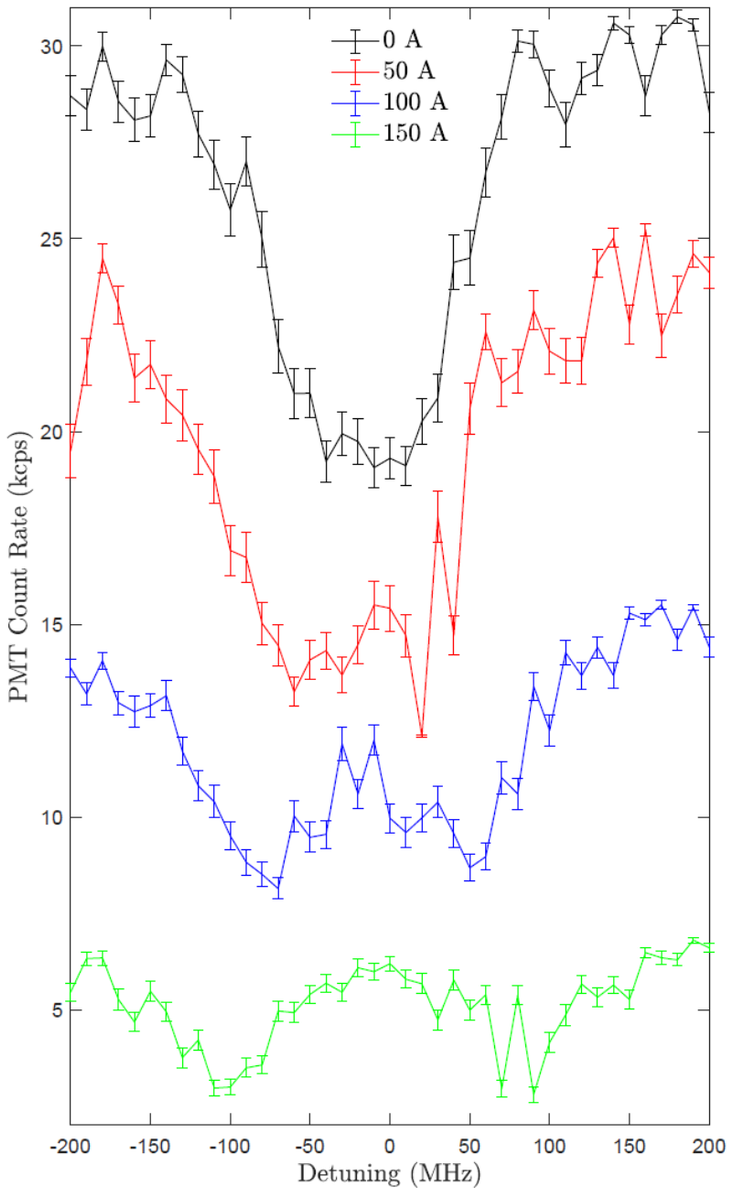

Figure 5.2: Four offset linescans of the shelving transition. The transition is probed using linear polarization at differing magnetic field values. Only the stretched state transitions are prominent. The laser frequency is scanned by varying the scanning cavity lock setpoint.

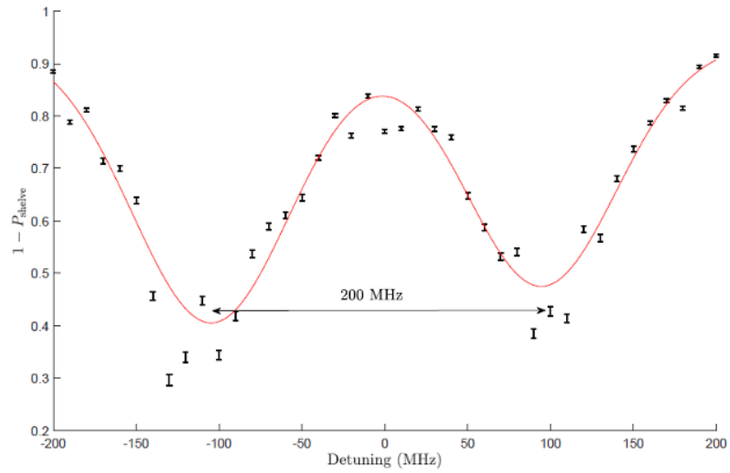

Adding in optical pumping (circularly polarised), should remove one of these peaks, say the left one, leaving us with just the f5 line:

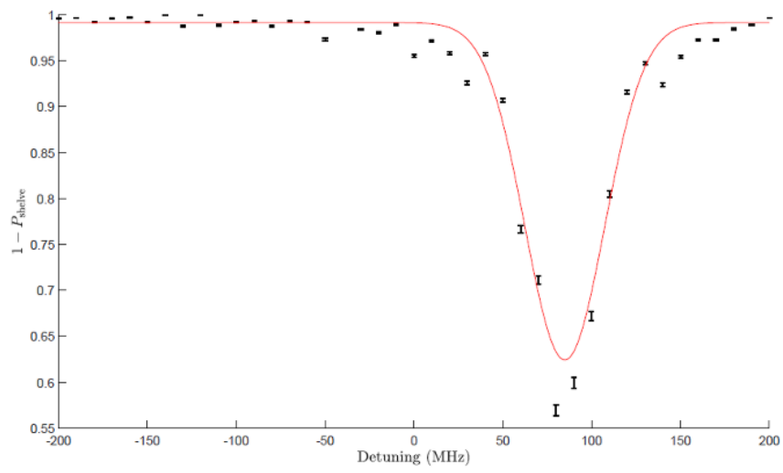

Figure 5.3: Two shelving linescans showing the effect of adding the optical pumping beam. Optical pumping moves the ion to the $S_{1/2},\ m_j = 1/2$ ground state, and only one stretched transition is driven. The shelving power in this scan is too low to fully shelve the ion.

5.3 Driving Between Zeeman Levels

The $S_{1/2},\ m_j = -1/2 \rightarrow S_{1/2},\ m_j = 1/2$ transition, which has frequency set by the magnetic field, 2.8 MHz/G, can be driven directly with a resonant microwave signal or by performing a stimulated Raman transition with an optical beat note at the transition resonance.

5.3.1 RF wire

A wire was placed in the vacuum chamber to directly drive between the ground state Zeeman levels. The microwave signal was amplified and controlled with one of the pulser's DDSs. To couple the signal into the chamber, a variable capacitor was tuned to 4 pF to match the LC resonance of the wire with the Zeeman transition resonance. At this capacitance, only 4% of the power was reflected from a directional coupler, as measured with a spectrum analyzer. With a max DDS power of 0 dBm, unknown amplification factor, the RF wire was only able to produce a Rabi frequency of $\Omega_{RF} = 2\pi \times 5$ kHz, and was not used further.

5.3.2 Raman

Since the laser is pulsed, it has a beat-note at multiples of its reprate. Instead of trying to vary this beat-note, the magnetic field can be varied until the Zeeman level splitting matches a multiple of the reprate. Twice the reprate is chosen so the Zeeman states are split far enough for state detection.

5.3.2.1 Single Beam

By applying a beam at an angle to the magnetic field, its polarization can have both π and σ components to drive the Raman transition in Fig. 2.2. A circularly polarized beam perpendicular to the magnetic field maximizes the Rabi frequency, and with this polarization, a single pulse of 38 nJ was able to completely drive population between $|\uparrow\rangle$ and $|\downarrow\rangle$, as shown in Fig. 5.4.

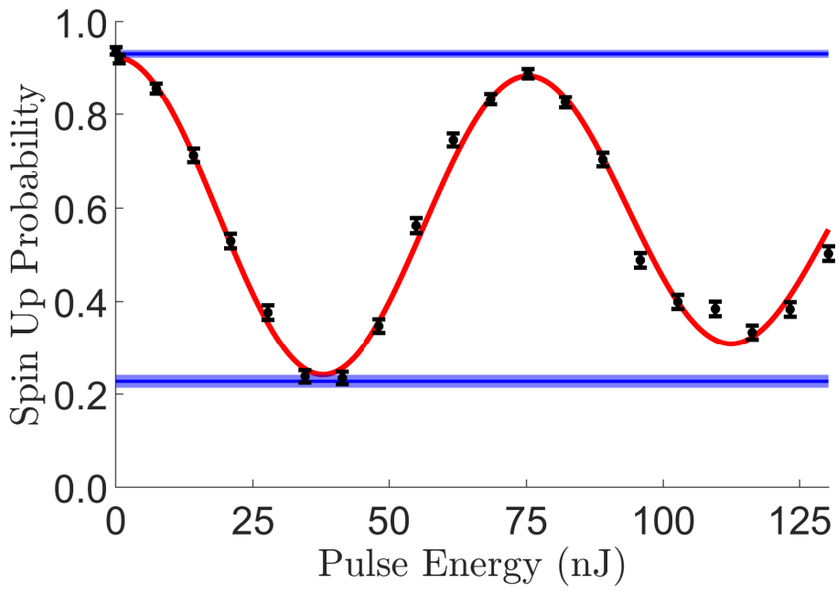

Figure 5.4: Power scan while sending a single pulse from the laser on the atom

---

5.3.2.2 Tunable Co-Propogating Beam

The beatnote frequency can be tuned using AOMs to provide additional frequency shifts. Two beams are given separate frequency shifts and overlapped to form a tunable, co-propogating Raman beam. By tuning the magnetic field away from twice the laser reprate and matching the beatnote frequency using the AOM shifts, the co-propogating beam drives Raman transitions while the other beams are off-resonant and can be analyzed without driving transitions. This allows for more flexibility with the type of experiments that can be performed. Fig. 5.5 shows a Ramsey experiment with the Ramsey $\pi/2$ pulses done by the co-propogating beam and the σ-polarized SDK beam remaining on during the Ramsey wait to provide an AC stark shift. The ion state probability, colormap (blue corresponding to low probabilities and yellow to high probabilities), is plotted against the Ramsey wait time, y-axis, and phase difference between the $\pi/2$ pulses on the x-axis. The Ramsey wait time is paramaterized in terms of the number of pulses ouput by the laser between the two $\pi/2$ pulses, with 13 ns the time between each pulse. The phase between the $\pi/2$

pulses was scanned using the phase of the co-propogating beam AOMs. The sigma-polarized beam causes a time-averaged differntial light shift of a few MHz resulting in the Ramsey fringes to be slanted.

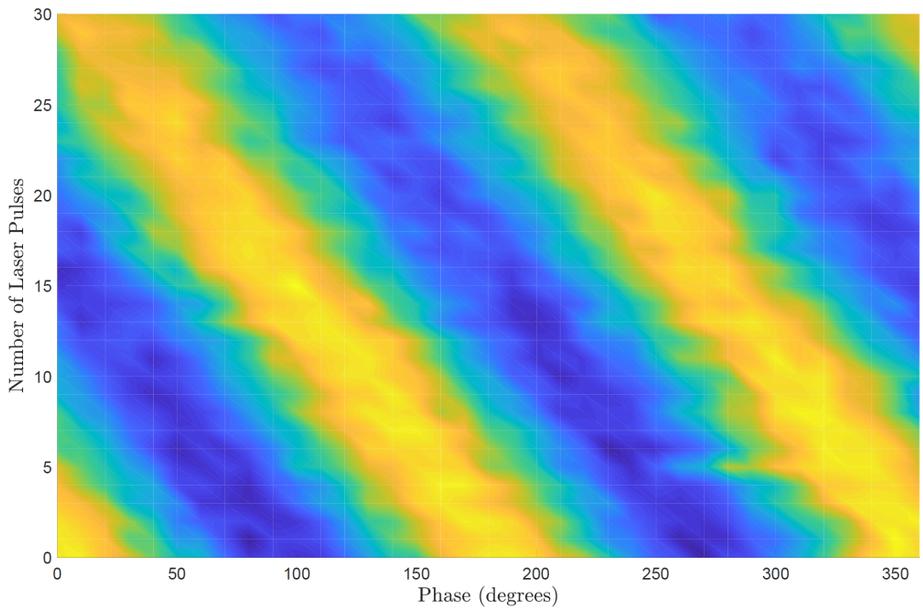

Figure 5.5: Co-propogating Ramsey experiment showing a few MHz time-averaged differential light shift.

5.4 Decoherence from Ion Motion

When running experiments, the ion position can fluctuate experiment to experiment. When the fluctuations are large enough, it can significantly affect the coherence of the Rabi flopping. The intensity at the ion can be parameterized as $I = \alpha I_0$. For Gaussian beams $\alpha = e^{-2r^2/w^2}$, where w is the $1/e^2$ waist of the beam. The probability of transition is then

$$P_{\downarrow} = \int_0^1 \mathrm{d}\alpha \; P_\alpha \left(\frac{1}{2} - \frac{1}{2} \cos\left(\alpha \Omega t\right) \right), \tag{5.1}$$

for Ω the two-photon Rabi frequency corresponding to intensity I_0 and P_α the probability distribution function for α. P_α can be found starting from the energy proba-

bility distribution P_E:

$$\int P_\alpha \, \mathrm{d}\alpha = \int P_r \, \mathrm{d}r = \int P_E \, \mathrm{d}E \tag{5.2}$$

$$\Rightarrow P_\alpha = P_r \frac{\mathrm{d}r}{\mathrm{d}\alpha} = P_E \frac{\mathrm{d}E}{\mathrm{d}r} \frac{\mathrm{d}r}{\mathrm{d}\alpha} \tag{5.3}$$

For a temperature T, the ion has a normalized energy distribution, $P_E = \frac{1}{k_B T} e^{-E/(k_B T)}$. The energy of the ion in the trap is $E = \frac{1}{2} m v^2 + \frac{1}{2} m \omega^2 r^2$. Using the virial theorem, $E = m\omega^2 r^2 \Rightarrow \frac{\mathrm{d}E}{\mathrm{d}r} = 2m\omega^2 r$. The radius in terms of α, $2r^2 = w^2 \ln(\alpha) \Rightarrow r \frac{\mathrm{d}r}{\mathrm{d}\alpha} = -\frac{w^2}{4\alpha}$. The distribution of intensity parameters with $g = \frac{m\omega^2 w^2}{2k_B T}$ is

$$P_\alpha = P_E \frac{\mathrm{d}E}{\mathrm{d}r} \frac{\mathrm{d}r}{\mathrm{d}\alpha} = \left(\frac{m\omega^2 r}{k_B T} \exp\left(-m\omega^2 r^2/(2k_B T)\right) \right) \frac{\mathrm{d}r}{\mathrm{d}\alpha} \tag{5.4}$$

$$= -\left(\frac{2m\omega^2 r}{k_B T} \exp\left(-m\omega^2 r^2/(k_B T)\right) \right) \frac{w^2}{4\alpha} \tag{5.5}$$

$$= -\frac{m\omega^2 w^2}{2\alpha k_B T} \exp\left(-m\omega^2 (w^2 \ln(\alpha))/(2k_B T)\right) \tag{5.6}$$

$$= -\frac{m\omega^2 w^2}{2\alpha k_B T} \alpha^g = g\alpha^{g-1}, \tag{5.7}$$

Plugging back into Eq. (5.1):

$$P_\downarrow = g \int_0^1 \mathrm{d}\alpha \; \alpha^{g-1} \left(\frac{1}{2} - \frac{1}{2} \cos(\alpha \Omega t) \right) \tag{5.8}$$

$$= \frac{1}{2} - \frac{1}{2} {}_1F_2 \left(\frac{g}{2}; \frac{1}{2}, \frac{g}{2} + 1; -\frac{\Omega^2 t^2}{4} \right) \tag{5.9}$$

where ${}_1F_2(a_1, b_1, b_2, x)$ is a generalized hypergeometric function. Fig. 5.6 shows the transition probability curves for a few values of g.

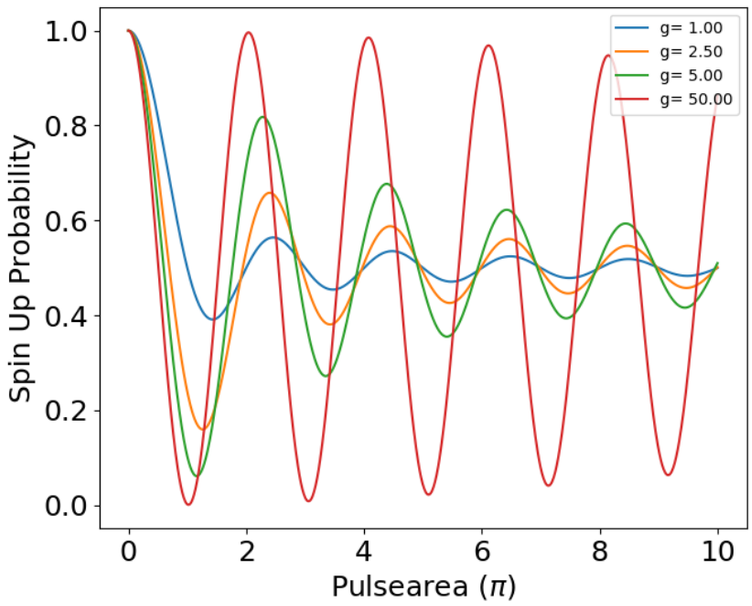

Figure 5.6: Spin up probability curves for varying values of g.

The ion exhibits similar behaviour in the experiment. Taken with a single beam, Fig. 5.7 shows the experimental stimulated Raman Rabi flopping decay time decrease with Rabi frequency.

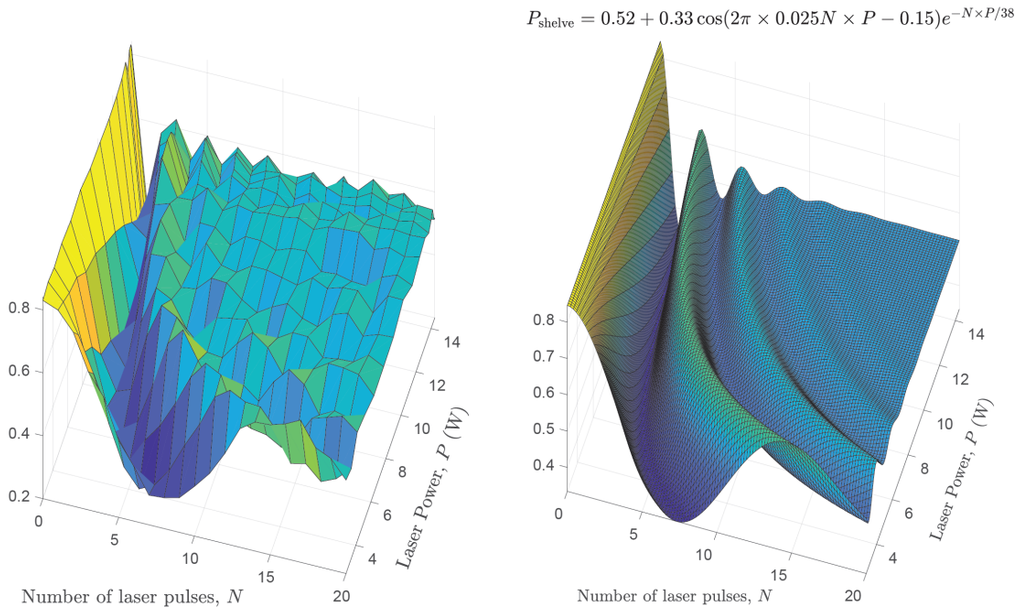

Figure 5.7: Experimental spin up proabability vs. time, or number of laser pulses, and power. The left plot is experimental data, the right plot shows a fit to the function displayed in the top right of the figure.

5.5 Two-Beam

To impart momentum on the ion, two pulsed beams with pure polarization are temporally overlapped at the ion.

Although the polarization of the beams is verified with a home-built polarimeter, the ion gives a more faithful test of the beam polarization. Due to small imperfections in the beam pointing and polarization, both the pi- and sigma-beam drive the Raman transition when applied individually, albeit with relatively small Rabi frequencies. Using the change of these individual-beam Raman Rabi frequencies compared to waveplate angle, the optimal polarizations for both the pi- and sigma-beam are found.

The pi-beam should be circularly polarized to maximize the two-beam Raman Rabi frequency, this polarization minimizes the individual-beam Raman Rabi frequency for the pi-beam. Using a quarter waveplate the polarization ellipticity can be changed to circular, $\hat{\epsilon}_\pi = \frac{1}{\sqrt{2}}(\hat{x} + i\hat{z}) = \frac{1}{2}\left(-\hat{\sigma}_+ + \hat{\sigma}_- + \sqrt{2}\hat{\pi}\right)$. This polarization will

maximize the individual-beam Raman Rabi frequency for the pi-beam. Thus, the optimal waveplate angle for the fastest two-beam Raman Rabi frequency according to the plot below is 71°.

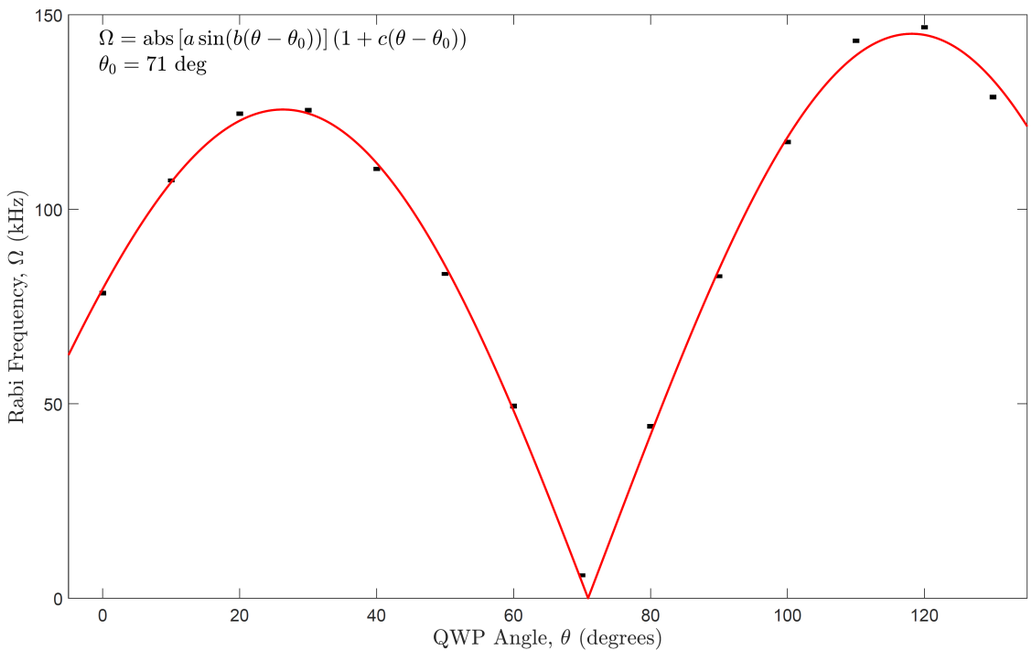

Figure 5.8: Rabi frequency as a function of pi-beam polarization. $\theta = 71°$ corresponds to linear, π, polarization and the maxima near 26° and 116°, circular.

The sigma-beam should be circularly polarized to maximize the two-beam Raman Rabi frequency, this polarization also maximizes the Raman Rabi frequency when only using the sigma-beam. Using a quarter waveplate, the polarization ellipticity can be changed to linear, $\hat{\epsilon}_\sigma = \hat{y}$. This polarization will minimize individual-beam Raman Rabi frequency for the sigma-beam. Thus, the optimal waveplate angle for the fastest two-beam Raman Rabi frequency according to the plot below is 17.4°.

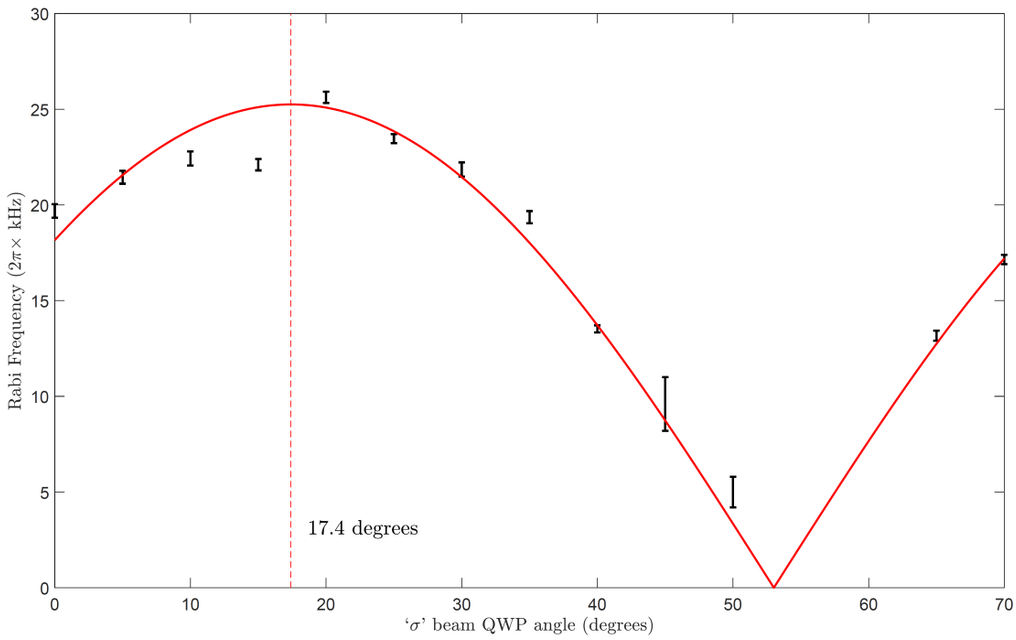

Figure 5.9: Rabi frequency as a function of sigma-beam polarization. $\theta = 17°$ corresponds to circular polarization and the minimum near 53°, linear

The pulses in the pi- and sigma-beam need to be temporally overlapped, which can be verified by the large increase in Rabi frequency. A large Rabi frequency translates to a broad resonance when scanning the magnetic field, as shown in the data below. First, the pi- and sigma-beam resonances are monitored individually. Then, both beams are applied simultaneously. When the pulses are temporally overlapped the magnetic field scan exhibits a much broader lineshape around resonance.

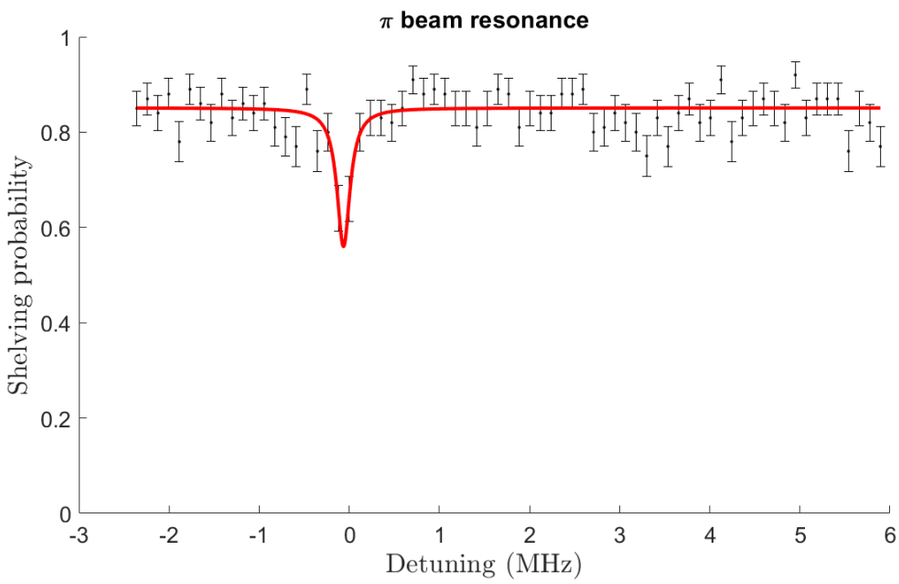

Figure 5.10: Raman resonance with only the pi-beam.

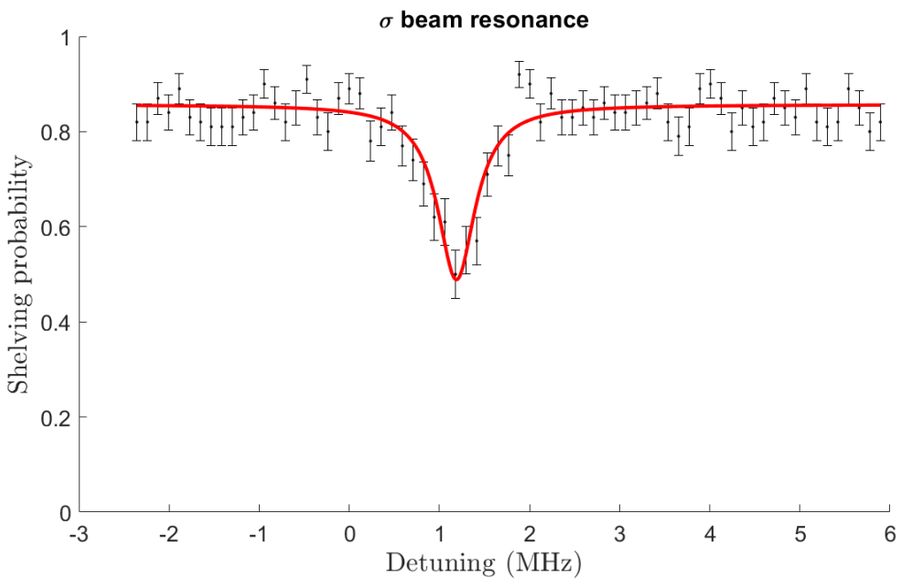

Figure 5.11: Raman resonance with only the sigma-beam.

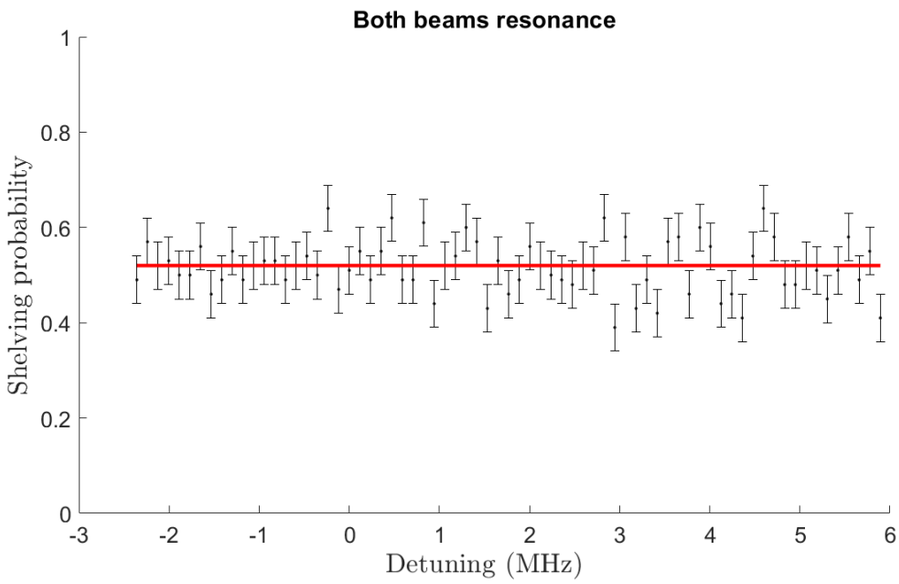

Figure 5.12: Raman resonance with both beams. The resonance width is much broader than both the individual-beam Raman Rabi frequencies.

More information regarding alignment procedures for both longitudinal and transverse overlap are in the OneNote, section "Lasers/SDK Lasers/Alignment".

5.6 Coupling to Transverse Motion

The following comes from Adam D West et al. "Tunable transverse spin–motion coupling for quantum information processing" Quantum Sci. Technol. 6 024003 (2021).

5.6.1 Abstract

Laser-controlled entanglement between atomic qubits ('spins') and collective motion in trapped ion Coulomb crystals requires conditional momentum transfer from the laser. Since the spin-dependent force is derived from a spatial gradient in the spin-light interaction, this force is typically longitudinal — parallel and proportional to the average laser k-vector (or two beams' k-vector difference), which constrains both the direction and relative magnitude of the accessible spin-motion coupling. Here, we show how momentum can also be transferred perpendicular to a single laser beam due to the gradient in its transverse profile. By controlling the transverse gradient at

the position of the ion through beam shaping, the relative strength of the sidebands and carrier can be tuned to optimize the desired interaction and suppress undesired, off-resonant effects that can degrade gate fidelity. We also discuss how this effect may already be playing an unappreciated role in recent experiments.

5.6.2 Introduction

Quantum computers based on trapped atomic ions use entanglement between the atomic qubits and collective motion to mediate conditional quantum logic between spatially separated qubits [BCM19]. This spin-motion entanglement is produced by applying a spatially-varying interaction with an electromagnetic field that gives a spin-dependent force. In laser-driven, ion-ion entangling gates, this force is derived from the longitudinal gradient of the electric field of a laser beam (or, for Raman processes, a pair of beams), in which case the direction of spin-motion coupling is fixed by the laser beam propagation axes [LBM03]. This precludes direct control of ion motion perpendicular to the beam, and also fixes the relative strengths of the resonant spin-only and spin-motion couplings. In many experiments using surface electrode traps, optical access is restricted to be parallel to the surface plane [RHS20]; this restriction makes it difficult to access motion perpendicular to the plane, both for cooling and coherent operations.

Two workarounds to access out-of-plane motion are the development of traps with tilted principal axes [SCR06, Wes08, LGA08, ASS10, SFH10, PBB19], or the introduction of time-dependent cross-coupling potentials [GSS14]. These indirect techniques take advantage of the approximate separability of the secular motion into components along the principal axes of the trap to provide access to part of the motion (the secular component), but direct access to the full motional state (for instance, to diagnose excess micromotion) remains challenging [ASS10, NDM11]. The method presented here has the additional benefit of only requiring a single beam to couple to motion. Alternative approaches for controlling spin-motion coupling using static and near-field gradients are being pursued by some groups [OLA08, OWC11, HSA16, SSB19, ZHM19, SBS19, SSB20], however these are constrained by the fixed electrode geometry and typically have a lower associated Rabi frequency than is possible with

the technique we describe here.

Here, we show that the transverse, as opposed to longitudinal, gradient of the spin-light interaction can also be used to produce and control spin-motion entanglement, even perpendicular to the laser propagation direction. By adjusting the spatial profile and/or position of the beam, the strength of motional sidebands can be tuned, even to the point where the carrier transition is fully suppressed. By extinguishing the carrier during sideband operations and extinguishing the sidebands during carrier operations, this flexibility has the potential to suppress errors from off-resonant transitions [OIB07]. As a proof of principle, we demonstrate this transverse spin-motion coupling using a single trapped ion. The stimulated Raman spectrum driven in a co-propagating beam geometry shows motional sidebands driven by the beam's transverse intensity gradient, and we show that their strength can be tuned by varying the ion temperature, in agreement with the model.

5.6.3 Theory

We consider a laser-driven electronic transition in a single trapped ion and show how the finite transverse extent of the beam can change the motional state perpendicular to the beam, even when the (conventional longitudinal) Lamb-Dicke factor is essentially zero. Since the technique presented here is applicable to every type of electronic transition used for quantum information processing (E2, E3, stimulated Raman, etc.), we present it without reference to the details of the internal state manipulation where possible and point out where differences may arise. We assume that the wavevector of the laser field (or wavevector difference, for stimulated Raman transitions) is aligned with $+\hat{\mathbf{z}}$, which we also assume is a principal axis of the trapping potential such that the longitudinal gradient cannot couple to motion in the x-y plane. For simplicity, we consider motion along only the x direction and neglect the other two; a full treatment that includes y and z can be constructed in a straightforward manner. We can write the matrix element associated with this transition as

$$\Omega_{n',n} = \Omega_0 \langle n'|f(x)|n\rangle \tag{5.10}$$

where n (n') is the initial (final) motional state along x and the function $f(x)$ is the transverse spatial profile of the laser-ion coupling, $\Omega(x) \equiv \Omega_0 f(x)$. We absorb all of the electronic transition details in Ω_0 and assume the atomic matrix element is proportional to f.[1]

While the beam profile can in principle have a variety of functional forms we will first assume it is Gaussian, with $f(x) \equiv \exp(-2x^2/w^2)$ (shortly, we also consider the case of a TEM_{10} mode). In the case of a stimulated Raman transition, $f(x)$ describes the product of the electric fields, $E_1 E_2^*$. Assuming a co-propagating configuration where the two frequency components have identical beam profiles, $w = w_0$, the Gaussian beam waist, defined as the $1/e^2$ intensity radius. In the case of a single photon transition (e.g. E2 or E3), $f(x)$ is the profile of the electric field and $w = \sqrt{2}w_0$.

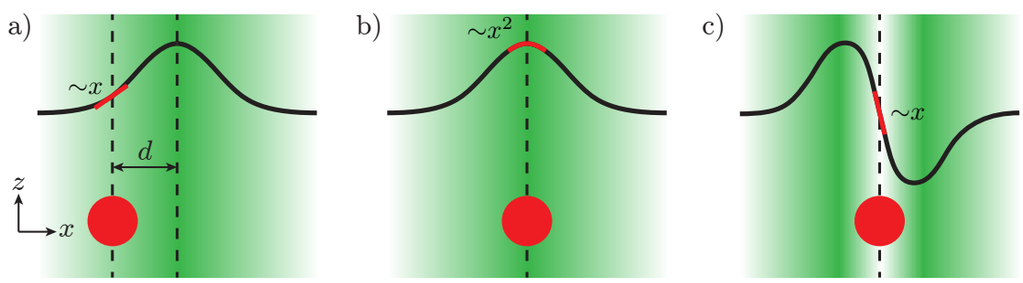

Figure 5.13: Schematic showing the geometry considered. A laser beam directed along z is incident on a trapped ion (red). a) and b) show the case where the interaction strength has a Gaussian (TEM_{00}) transverse profile (black solid line). Depending on the beam position, the profile at the ion can be approximately linear or quadratic (red solid line), coupling to first- or second-order sidebands, respectively. c) shows the case where the profile is produced by a TEM_{10} mode, which suppresses carrier transitions while still coupling to motion.

We will treat the spatial profile of the beam(s) by Taylor expanding about the ion's equilibrium position ($x = 0$) to second order in x. A Gaussian spatial profile that is offset from the ion's equilibrium position by a distance d (that is, $f(x-d)$, as

[1]Recent work has examined how a transverse electric field profile can drive an electronic, rather than motional, transition [SSK16], and how spin angular momentum, rather than linear momentum, of photons can provide a momentum kick to trapped ions [ACM20]

shown in figure 5.13a)) produces matrix elements of the following form (up to second order in x_0):

$$\Omega_{n',n} = \Omega_0 f(-d)\sqrt{\frac{n_>!}{n_<!}} \times \begin{cases} 1 + \frac{4x_0^2}{w^2}\left(\frac{4d^2}{w^2} - 1\right)(n + \frac{1}{2}) & \Delta n = 0 \\ \frac{4dx_0}{w^2} & |\Delta n| = 1 \\ \frac{2x_0^2}{w^2}\left(\frac{4d^2}{w^2} - 1\right) & |\Delta n| = 2 \end{cases}, \tag{5.11}$$

where $n_<$ ($n_>$) is the lesser (greater) of n and n', and $x_0 \equiv \sqrt{\hbar/2m\omega}$ is the motional mode's ground state wavefunction size, with m the mass and ω the secular frequency. We note that when $d = 0$ the Rabi frequency of all odd-order sidebands vanishes, as can be seen in Eq. 5.11 for $|\Delta n| = 1$. Exact expressions for $\Omega_{n',n}$ and are provided in 5.6.6.

In the Lamb-Dicke regime, a simple analytic expression describes the longitudinal spin-motion coupling, to lowest order in the Lamb-Dicke parameter $\eta \equiv kx_0$ (for wavevector k) [WMI98]. We compare this to the case of transverse spin-motion coupling by defining an effective Lamb-Dicke parameter, $\tilde{\eta}_{(s)}$, where s is the sideband order. As an example, if $d = w/2$, for the first order sidebands we have

$$\Omega_{n+1,n} = \tilde{\eta}_{(1)}\ \Omega_0 f(-w/2)\sqrt{n+1} \tag{5.12}$$

with

$$\tilde{\eta}_{(1)} \equiv \frac{2x_0}{w} \approx 0.014\sqrt{\frac{100\ \mathrm{amu}}{m}}\sqrt{\frac{2\pi \times 1\ \mathrm{MHz}}{\omega}}\frac{1\ \mu\mathrm{m}}{w}. \tag{5.13}$$

When $d = 0$, the effective Lamb-Dicke parameter associated with the second-order sidebands has the same form ($\Omega_{n+2,n} \propto \tilde{\eta}_{(2)}^2/2$, with $\tilde{\eta}_{(2)} = 2x_0/w$). Unlike longitudinal spin-motion coupling from a plane wave, where the pth order sideband term is approximately proportional to $\eta^p/(p!)$, the expressions for the sideband strengths from transverse coupling are a function of the beam profile and position, and should be calculated individually for each sideband order.

The intuitive conclusion that we can draw is that transverse coupling to the ion motion is significant once the wavefunction size, $\sqrt{n}x_0$, becomes comparable to the transverse profile size, w. As the spatial extent of the beam becomes smaller, the corresponding transverse momentum spread of each photon increases, in accordance with the uncertainty principle, and the nonzero variance of this transverse momentum can change the transverse momentum of an ion without violating conservation of

linear momentum. For the case of a stimulated Raman transition using a single focussed beam centred on the ion, one can associate an effective wavevector, $k_{eff} \equiv \tilde{\eta}/x_0 = 2/w_0$, with this momentum spread. An equivalent value of k_{eff} can be achieved with two infinite plane waves crossing at an angle equal to the half-cone divergence angle of the single beam, $\theta \equiv \frac{\lambda}{\pi w_0}$, i.e. the coupling strength with the single focussed beam is half that for a pair of crossed plane waves defined by the same angular acceptance. This is a spatial manifestation of Ramsey's famous factor of two [Kle13].

Having seen that transverse coupling to odd-order sidebands disappears with a centered TEM_{00} beam, we now show that coupling to even-order sidebands (and carrier) can be extinguished if $f(x)$ is an odd function of x, such as with a TEM_{10} mode (cf. figure 5.13c)) driving either a single photon transition (such as E2) or one of the arms of a stimulated Raman transition (with the other arm uniform intensity). Here, the Rabi frequency, $\Omega(x) \equiv \Omega_0 f(x)$, vanishes at the equilibrium position of the ion and has odd parity. For a TEM_{10} beam with waist w_0, this configuration produces the same Rabi coupling for the single-photon and Raman cases, $f(x-d) \equiv H_1(\sqrt{2}(x-d)/w_0)\exp(-(x-d)^2/w_0^2) = 2\sqrt{2}\frac{x-d}{w_0}\exp(-(x-d)^2/w_0^2)$ where $H_1(x)$ is the first Hermite polynomial. Once again expanding to second order in x_0 gives the matrix elements for the carrier and the first and second sidebands:

$$\Omega_{n',n} = \Omega_0\ 2\sqrt{2}\ e^{-d^2/w_0^2}\sqrt{\frac{n_>!}{n_<!}} \times \begin{cases} -\frac{d}{w_0}\left(1 - \frac{6x_0^2}{w_0^2}(1 - \frac{2d^2}{3w_0^2})(n+\frac{1}{2})\right) & \Delta n = 0 \\ \frac{x_0}{w_0}(1 - \frac{2d^2}{w_0^2}) & |\Delta n| = 1 \\ \frac{d}{w_0}\frac{3x_0^2}{w_0^2}(1 - \frac{2d^2}{3w_0^2}) & |\Delta n| = 2 \end{cases} . \tag{5.14}$$

Since $f(x)$ is odd, when $d = 0$ the carrier and all even order sidebands vanish to all orders in x_0 (the exact expression for $\Omega_{n',n}$ and arbitrary order Hermite-Gaussian profile can be found in 5.6.6). This suggests that by switching between transverse spatial modes, the carrier or first sidebands can be suppressed as the application demands, which can be used to reduce undesired off-resonant effects. For example, using a TEM_{10} could allow for Mølmer-Sørensen type gates [MS99] to be used at higher temperatures as the strengths of the carrier and second sidebands are greatly reduced. A related effect in the longitudinal direction has been explored for optical standing waves [CBZ92, WMI98, Jam98, RAM14, UAK20], but the motional coupling

in that case is still constrained to be along the longitudinal direction.

The appearance of sidebands (i.e. motional coupling) from the transverse spatial profile of a laser beam can be understood semi-classically in the time domain by considering that the oscillatory motion of an ion into and out of a laser beam gives an intensity modulation that produces sidebands at this oscillation frequency, which can in turn drive motional-state-changing transitions.

Alternatively, one can consider the associated Bloch sphere. In a frame rotating at the qubit splitting, the Bloch vector precesses azimuthally at a frequency equal to the detuning, Δ. With negligible ion motion, no significant population transfer occurs (assuming $\Omega \ll \Delta$). With ion oscillation comparable to the beam size, the Rabi frequency will be modulated at ω and 2ω, associated with the linear and quadratic parts of $f(x)$, respectively. When $\Delta = \omega$, or 2ω, the precession and intensity modulation are synchronized. The result is a Bloch vector that 'spirals' up or down the Bloch sphere even for $\Omega \ll \Delta$ (see Supplemental Material).

5.6.4 Experiment

The analysis we have presented indicates that if motional coupling can be driven by the transverse profile of a laser beam, sidebands should appear even for a co-propagating stimulated Raman transition (for our setup, this gives a longitudinal Lamb-Dicke parameter of $\eta \approx 10^{-7}$; note that the two frequencies required for the Raman transition are produced by the laser's pulsed nature, ensuring collinearity). The experiment we perform to observe these sidebands is shown schematically in figure 5.14. Briefly, we trap a single laser-cooled $^{138}Ba^{+}$ ion in a linear Paul trap made with four segmented cylindrical rods. The diagonal surface-to-surface distance between the rods is $2r_0 = 2\ cm$. RF voltages are applied to the central segments at a frequency of 1 MHz to produce radial secular frequencies $\omega_{rad} \approx 2\pi \times 100\ \mathrm{k}Hz$. The axial secular frequency is $\omega_{ax} = 2\pi \times 36\ \mathrm{k}Hz$.

We define a Zeeman qubit with the two electron spin states ($|\downarrow\rangle$, $|\uparrow\rangle$) of the $^2\mathrm{S}_{1/2}$ ground state manifold, which are split by 151.8 MHz by the application of a magnetic field of around 5.5 mT. Preparation of the qubit states is performed via optical pumping with circularly polarised light on the $^2\mathrm{S}_{1/2} \leftrightarrow {}^2\mathrm{P}_{1/2}$ transition. Readout of

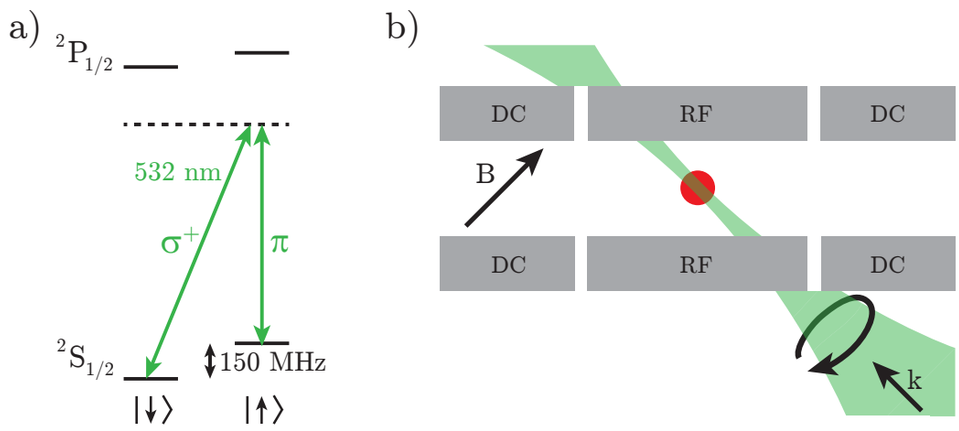

Figure 5.14: a) Structure of the $^{138}Ba^+$ Zeeman qubit showing the laser field applied to drive stimulated Raman transitions b) Schematic of ion trap showing two of the four segmented rods and the single circularly polarised beam used to drive the Raman transitions.

the qubit state is achieved via electron shelving; circularly polarised light at 455 nm selectively optically pumps one of the qubit states to the long lived ($\tau \approx 30$ s) $^2D_{5/2}$ manifold via the $^2P_{3/2}$ manifold. Coherent transfer between the qubit states is driven by a far-detuned stimulated Raman transition via a mode-locked Nd:YVO_4 laser[2]. The qubit splitting is close to twice the repetition rate of the laser such that different frequency components of the laser light can resonantly drive the qubit transition when the magnetic field tunes the qubit splitting into resonance. Using the frequency comb structure of a mode-locked laser for this type of manipulation has previously been demonstrated in work with hyperfine qubits [HMM10], but to our knowledge this is the first application to a Zeeman qubit[3].

To observe sidebands, we direct a single (i.e. 'co-propagating') circularly polarized beam at 45° to the axis of the trap and at 90° degrees to the quantization axis defined by the applied magnetic field (see figure 5.14). Even though none of the principal axes of the trap is perpendicular to the laser beam, traditional (i.e. longitudinal) spin-motion coupling will be effectively absent for this co-propagating geometry, and

[2]Coherent Paladin SCAN 532-36000.

[3]A mode-locked laser has been used to coherently manipulate a Zeeman qubit, but employing acousto-optic elements to generate the necessary beat note [ICL17]

the appearance of sidebands will be entirely due to transverse spin-motion coupling. We perform Rabi spectroscopy on the Raman transition by measuring the spin flip probability while varying the applied magnetic field with a shim coil.

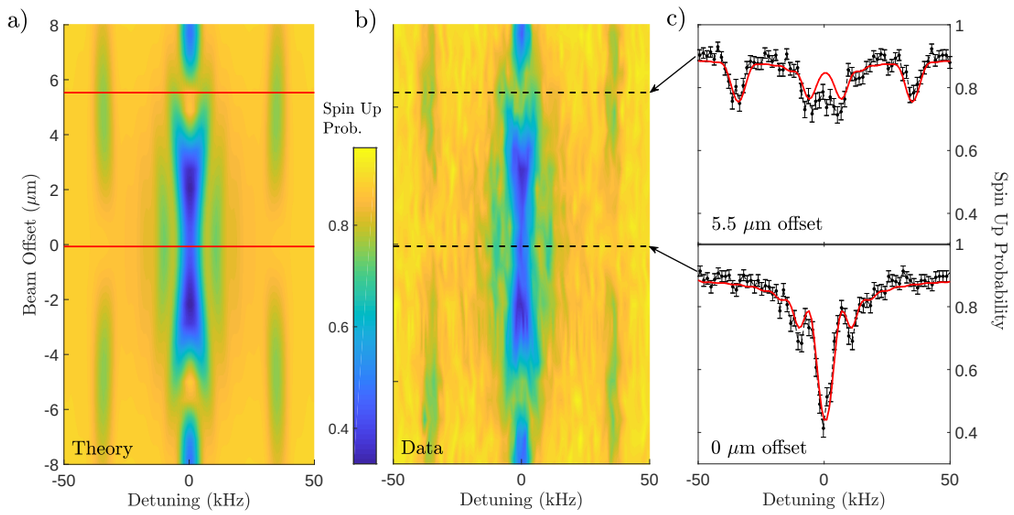

Figure 5.15: Appearance of transverse spin-motion coupling from a misaligned beam. a) Calculated and b) measured single-beam stimulated Raman spectra of the qubit as a function of beam position show sidebands for axial ion motion when the beam is off center. Horizontal lines indicate the slices shown in c). The only free parameter used to generate the theory plots is the ion's motional temperature, which is 3 mK.

Figure 5.15 shows the probability of a stimulated Raman transition (with state preparation and measurement errors included) as a function of the detuning and beam offset. When the beam is misaligned, sidebands associated with motion along the trap axis are clearly visible at detunings of ± 36 kHz, equal to the axial secular frequency. These sidebands vanish when the beam is centered on the ion as the gradient of the beam profile disappears, cf. Fig. 5.13.

The plot in Fig. 5.15a) shows the numerical solution of the Schrodinger equation with Rabi frequencies calculated as previously described. The ion temperature is the only free parameter used to match the experimental data (see Supplemental Material). The transverse Lamb-Dicke parameter for the first-order axial sideband ranges from $\tilde{\eta}_{(1)} = 0$ to 0.021 in Fig. 5.15. While this Lamb-Dicke parameter is small, the 3 mK mean occupation number of $\bar{n}_z = 1800$ can produce significant transverse

motional coupling.

5.6.5 Discussion

Spin-motion coupling due to the transverse electric-field profile presents an additional tool with which to manipulate trapped ions. However, it may also represent an additional source of infidelity in trapped ion quantum computers. In many cases, single-site addressability is required and achieved via tightly focused laser beams which introduces spin-motion coupling for the transverse directions. It has already been shown that residual motion transverse to such beams can produce gate infidelities [CEN20], but we now draw attention to the possibility that these beams can also impart momentum in the transverse directions.

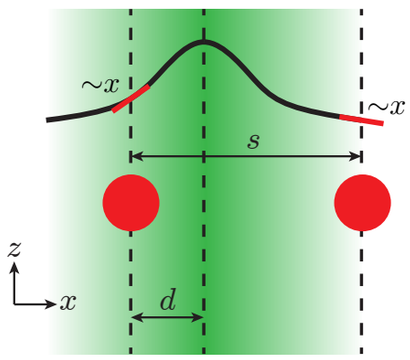

Figure 5.16: Laser incident on two ions, misaligned from a 'target' ion (left) by d. The transverse spatial profile of the interaction strength is approximately linear for both the target ion and the neighbouring ion, which can produce spin-motion coupling along the x direction.

With reference to figure 5.16, we consider as an example the trapped ion quantum processor of Debnath *et al.* [DLF16]. Individual $^{171}Yb^{+}$ ions, spaced by $s \approx 5$ μm in a trap with axial secular frequency $\omega/2\pi = 270$ kHz, are addressed by a pair of stimulated Raman beams. One of the beams provides a uniform intensity, while the other has waist $w \approx 1.5$ μm. Assuming a misalignment of $d = w/2$, we use Eq. (5.11) to calculate the transverse Lamb-Dicke parameters associated with the target ion to be $\tilde{\eta}_{(1)} \approx 0.0098$ and $\tilde{\eta}_{(2)} = 0$ for the first and second sidebands, respectively. Similarly for the neighbouring ion, $\tilde{\eta}_{(1)} \approx 0.037$ and $\tilde{\eta}_{(2)} \approx 0.035$.

If the quoted crosstalk in [DLF16] of 4 % (interpreted as the ratio of carrier Rabi frequencies between adjacent ions) were solely due to beam misalignment, this would imply $d \approx 1.8$ μm and hence $\tilde{\eta}_{(1)} \approx 0.017$, $\tilde{\eta}_{(2)} \approx 0.014$ ($\tilde{\eta}_{(1)} \approx 0.030$, $\tilde{\eta}_{(2)} \approx 0.028$) for the target (neighbouring) ion. Transverse spin-motion coupling would, in general, lead to residual spin-motion entanglement in a two-qubit gate. We estimate that for a Mølmer-Sørensen type interaction [MS99, SM99], with the parameters we have outlined and assuming the axial modes are cooled to the Doppler limit, this would produce an infidelity at approximately the 10^{-5} level. While this is too small to be of concern, it could become problematic for longer ion chains, or for traps where the axial modes are less far detuned from the mode used for computation; a fourfold reduction in detuning would produce an infidelity at the 10^{-3} level.

5.6.6 Exact Expression for Transverse Rabi Frequency

While the use of a Taylor series in eqs. (5.11) and (5.14) provides intuition about how coupling between motional states depends on the transverse profile, an exact analytic expression for the Rabi frequency also exists. The equations below give the Rabi frequency associated with driving a transition from motional state n to motional state n' using transverse spin-motion coupling from a laser beam with a specific transverse spatial mode (along the motional mode direction) that is displaced by a distance d from the trap centre. We write the Rabi frequency in terms of the function $J_{n',n,p}$ as

$$\frac{\Omega_{n',n,p}}{\Omega_0} = \langle n' |\, H_p\left[\sqrt{2}(x-d)/w_0\right] e^{-(x-d)^2/w^2} \,|n\rangle \;= \frac{J_{n',n,p}(\alpha,\beta,\delta)}{\sqrt{\pi\; 2^{n'+n}\; n'!\; n!}} \tag{5.15}$$

where

$$\alpha(w) \equiv \left(\frac{2x_0}{w}\right)^2, \qquad \beta \equiv \frac{2x_0}{w_0}, \quad \text{and} \quad \delta \equiv \frac{d}{\sqrt{2}x_0}. \tag{5.16}$$

(Recall that in the case of a Raman transition with one TEM_{p0} beam and one TEM_{00} beam, we identify $w = w_0$, whereas for either a Raman transition with one TEM_{p0} beam and one uniform beam, or for a single-photon transition driven by a TEM_{p0} beam, we use $w = \sqrt{2}w_0$.)

The integral $J_{n',n,p}$ is given by

$$J_{n',n,p}(\alpha,\beta,\delta) \equiv \int_{-\infty}^{\infty} \mathrm{d}\xi \; e^{-\alpha(\xi-\delta)^2-\xi^2} H_{n'}(\xi)\, H_n(\xi)\, H_p(\beta(\xi-\delta)) \tag{5.17}$$

$$\begin{aligned}
&= \sqrt{\frac{\pi}{1+\alpha}}\, \exp\left[\frac{\alpha^2\delta^2}{1+\alpha} - \alpha\delta^2\right] n'!\; n!\; p! \\
&\times \sum_{s=0}^{\min[n',n]} \sum_{q=0}^{\min[n'-s,p]} \sum_{r=0}^{\min[n-s,p-q]} \left\{ \frac{\left(\frac{2}{1+\alpha}\right)^{s+q+r} \beta^{q+r} (-i)^{n'+n+p-2(s+q+r)}}{s!\; q!\; r!\; (n'-s-q)!\; (n-s-r)!\; (p-q-r)!} \right. \\
&\times \left(\frac{-\alpha}{1+\alpha}\right)^{(n'+n-q-r-2s)/2} \left(\frac{\beta^2}{1+\alpha} - 1\right)^{(p-q-r)/2} \\
&\times \left. H_{n'-s-q}\left(\delta\sqrt{\frac{\alpha}{1+\alpha}}\right)\; H_{n-s-r}\left(\delta\sqrt{\frac{\alpha}{1+\alpha}}\right)\; H_{p-q-r}\left(\beta\delta\frac{\left(\frac{\alpha}{1+\alpha}-1\right)}{\sqrt{1-\frac{\beta^2}{1+\alpha}}}\right) \right\},
\end{aligned} \tag{5.18}$$

where $\xi = x/\sqrt{2}x_0$ has been used as a normalised spatial coordinate.

To compare different values of p for the same optical power in the TEM_{p0} mode, eq. (5.15) should be multiplied by $1/\sqrt{p!\; 2^p}$. In this case, the effective Lamb-Dicke factor for the first order sideband in the regime where $w_0 \gg x_0\sqrt{n}$ scales approximately as $\tilde{\eta}_{(1)} \propto p^{\frac{1}{4}}$.

5.6.7 Simulated Spectra

Figure 3 in the main paper shows spectroscopy of a Raman transition, both from experimental measurements and theory. The theory data are calculated via numerical solution of the Schrodinger equation. Thermal averaging is incorporated by averaging the result over a Boltzmann distribution of the initial motional states, n_x, n_y, n_z. We include all motional transitions that alter the total number of motional quanta by at most two i.e. $|(n'_x - n_x)| + |(n'_y - n_y)| + |(n'_z - n_z)| \leq 2$. The only fit parameter is the (isotropic) temperature of the ion. The other parameters used in the calculation are obtained as follows:

1. Rabi frequency: By observing Rabi flopping when the beam is aligned with the ion we directly measure the Rabi frequency. This is then modified for different beam offsets according to the beam profile. With knowledge of the beam profile we can then calculate the Rabi frequencies for the various motional transitions as described in the main paper.

2. Beam waist: By scanning the beam across the ion and observing the change in Rabi frequency we directly obtain the beam profile and extract the waist.

3. Beam offset: We find the position with zero offset by computing the centre of mass of the experimental data, i.e. when the beam offset is calibrated correctly, the signal integrated along the positive and negative directions of the beam position is equal. This value was also found to be in good agreement with the value obtained using the profiling technique described in the previous point.

4. Secular frequency: This was measured directly via a 'tickle scan'; an RF tone of varying frequency was applied to trap electrodes to determine the frequency at which resonant excitation of the ion's motion occured.

5. Raman pulse duration: This is precisely defined by the experimental sequence.

6. Detuning: The repetition rate of our laser defines the frequency of the beat note which drives the stimulated Raman transition. This frequency is measured precisely and allows us to calibrate the detuning axis.

The following parameters were used to produce the fits in figure 5.15:

1. Ion temperature: 3 mK

2. Rabi frequency when aligned with ion: $\Omega = 2\pi \times 9.5$ kHz

3. Beam waist: 9.5 µm along x, 11.5 µm along y

4. Secular frequency: $\omega = 2\pi \times 34.7$ kHz

5. Raman pulse duration: 180 µs, $\Omega t \approx 3.5\pi$

Note that the x and y coordinates here are defined with a z axis along the propagation direction of the beam (as opposed to according to the trap principal axes). A boxcar average of width 6 kHz is applied to the calculated spectrum to account for the presence of magnetic field noise in our system.

5.6.8 Semi-Classical Picture

The driving of motional sidebands can also be understood by considering the classical trajectory of an ion in a harmonic potential (trap frequency ω) and the resulting evolution of the Bloch vector. In a frame rotating at the transition frequency, with an applied field detuned by Δ, the motion of the Bloch vector is derived from two contributions: precession about the z axis at a frequency Δ and rotation about the x ($|0\rangle \pm |1\rangle$) axis at the instantaneous Rabi frequency, $\Omega(t)$. For constant $\Omega \ll \Delta$, little population transfer occurs — starting at $|1\rangle$, the Bloch vector rotates about x towards $|0\rangle$ for half a precession period then back towards $|1\rangle$ for half a precession period. For a beam aligned with the trap centre, ion motion modulates Ω at a frequency 2ω:

$$\Omega(t) = \Omega_0 \exp\left(-2x_0^2 \sin^2(\omega t + \phi)/\mathrm{w}^2\right) \tag{5.19}$$

where x_0 is the amplitude of motion, ϕ is the phase of the motional oscillation and w is the beam waist. When the precession frequency and modulation frequency are equal ($\Delta = 2\omega$), the Bloch vector will rotate quickly about x towards $|0\rangle$ for half a precession period and then slowly towards $|1\rangle$ for half a precession period. This produces the spiral trajectory illustrated in the left-hand plot of figure 5.17 for a coherent motional state.[4]

The result is that population transfer occurs on a motional sideband, without the need for counter-propagating beams. This behaviour persists when we consider a thermal ensemble which provides a distribution of x_0 and ϕ. When we average over the thermal distribution, the coherence between the $|0\rangle$ and $|1\rangle$ states is lost. If we consider an ensemble Bloch vector which is the average of individual particle Bloch vectors, the loss of coherence causes this ensemble vector to lie along $\pm z$. This behaviour is shown in the right-hand plot of figure 5.17. The distribution of motional states in the thermal ensemble also limits the transfer from $|0\rangle$ to $|1\rangle$ when averaging over the distribution; the minimum z coordinate of the Bloch vector trajectory is higher in this plot than in the left-hand one.

[4]This example corresponds to a second order sideband, but the same reasoning applies to a misaligned beam for a first order sideband

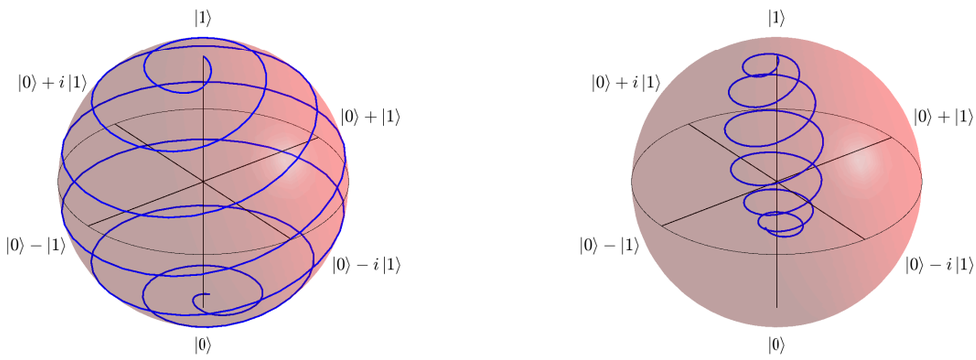

Figure 5.17: Plot of Bloch vector evolution for particles oscillating in a harmonic potential whilst addressed with an off-resonant laser beam with a Gaussian profile. Left: Single particle. Right: Average Bloch vector for 10 particles with different amplitudes and phases of motion.

5.7 Single Pulse SDK

The following comes from R. Putnam et al. "Impulsive Spin-Motion Entanglement for Fast Quantum Computation and Sensing." *preprint available, arXiv:2307.11287* (2023)

5.7.1 Abstract

We perform entanglement of spin and motional degrees of freedom of a single, ground-state trapped ion through the application of a 16 ps laser pulse. The duration of the interaction is significantly shorter than both the motional timescale (30 μs) and spin precession timescale (1 ns) , demonstrating that neither sets a fundamental speed limit on this operation for quantum information processing. Entanglement is demonstrated through the collapse and revival of spin coherence as the spin components of the wavefunction separate and recombine in phase space. We infer the fidelity of these single qubit operations to be $(97^{+3}_{-4})\%$.

5.7.2 Introduction

Spin-motion entanglement is at the heart of many trapped-ion quantum computers. Entanglement between the internal qubit states of ions is produced via ion-ion inter-

actions. These interactions are mediated by motion within the trap and modulated by the application of spin-dependent forces [CZ95, MS99, SM99, SM00, GTL16, WWC18]. In order to avoid the problem of spectral crowding, gates have been operated in the strong excitation regime, where the applied spin-dependent forces are impulsive, or applied much faster than the ions' motional mode period [GZC03, Dua04, BCK13, SIH14]. These impulsive forces, known as spin-dependent kicks (SDKs), dynamically impart momentum to the ion, with the direction of the kick dependent upon the ion's internal qubit state.

Previous work has demonstrated both single- and two-qubit gates with ultrafast pulses [MMM06, CMQ10, MSN13, WMJ17, GWH22]. While the picosecond duration of a single pulse from a mode-locked laser makes it attractive for building gates in the strong excitation regime, single pulses do not tend to produce the desired outcome with hyperfine qubits. Single pulse operations have been performed using resonant excitation as well as stimulated Raman transitions. In the resonant case, a π-rotation was performed using a single ultrafast pulse with 98.1% fidelity [GWH22], but the scheme could not be used to perform arbitrary single qubit rotations. Single-pulse, single qubit gates using stimulated Raman transitions in the hyperfine qubit of $^{171}Yb^{+}$ were limited by the finite qubit splitting while two-qubit gate fidelity using single-pulse spin-dependent kicks (SDKs) was limited by multi-photon transitions that produce unwanted higher-order momentum modes [CMQ10, MSN13, WMJ17]. In both schemes, to achieve high-fidelity two-qubit gates, multi-pulse sequences that are many times longer than the single pulse duration are necessary. This in turn makes two-qubit gates longer than the attractively-short duration of the atom-light interaction in a single laser pulse.

Aside from applications in quantum information processing, high-fidelity spin-dependent kicks are also a key feature of atom interferometry. Increasing wavepacket separation by large momentum transfer beamsplitter operations enhances interferometer sensitivity [CSP09, CMC08, MCH09, CKC11, PYZ18, JXH18, PZP19]. The ability to perform high-fidelity ultrafast spin-dependent kicks would enable even higher momentum transfer, a key ingredient to the recently proposed ion gyroscope interferometer [CH17, Wes19].

Here we demonstrate high-fidelity, ultrafast qubit rotations and spin-motion entanglement using a single, 16 ps laser pulse to drive a stimulated Raman transition in the ground-state Zeeman qubit of $^{138}Ba^{+}$. By observing the decay and revival of interference fringe visibility using a Ramsey pulse sequence, we verify the generation of spin-motion entanglement of a Zeeman qubit using a single laser pulse. Working with a Zeeman qubit offers improvements in both gate speed and simplicity compared to hyperfine qubits. The smaller qubit splitting allows for single-pulse single qubit gate fidelity comparable with current state of the art. Further, using polarization selectivity, a spin-dependent kick can be performed in a Zeeman qubit with a single laser pulse without producing higher-order momentum modes. Zeeman qubits are also the natural choice for a gyroscope interferometer, as the magnetic moment associated with the ion's motion, which can mask the desired rotation phase in the presence of a magnetic field, can be canceled by the Zeeman qubit's spin magnetic moment, essentially making this a clock qubit for the interferometer [CH17].

5.7.3 Experimental Setup

Our apparatus utilizes a single $^{138}Ba^{+}$ ion trapped in a four-rod, linear Paul trap with axial secular frequency $\omega = 2\pi \times 32.4$ kHz and radial secular frequencies $\omega_{\text{rad}} \approx 2\pi \times 100$ kHz. The stimulated Raman transition as shown in Fig. 5.18(a), can be driven using pulses from a 532 nm, mode-locked Nd:YVO_4[5] laser with a repetition rate of 76 MHz [WPC21]. An intensity autocorrelation measurement yields a sech pulse shape, with a full width at half max of $\tau_{\text{pulse}} = 16.4(5)$ ps, corresponding to a spectral bandwidth $\Delta f \approx 0.315/\tau_{\text{pulse}} \approx 19$ GHz. Arbitrarily gated patterns of laser pulses can be generated through the use of an electro-optic pulse picker. To achieve a π pulse within a single laser pulse, we tightly focus a beam to a $1/e^2$ intensity radius of $w_0 = 8.5(4)\,\mu$m. Single-pulse SDKs, which require differing wavevectors, are achieved by splitting the laser beam into an additional, orthogonally directed beam with a waist of $w_0 = 20(2)\,\mu$m. Temporal overlap of the Raman beams is achieved with an optical interferometer to measure the electric field autocorrelation and is subsequently refined using the response of the ion.

[5] Coherent Paladin SCAN 532-36000.

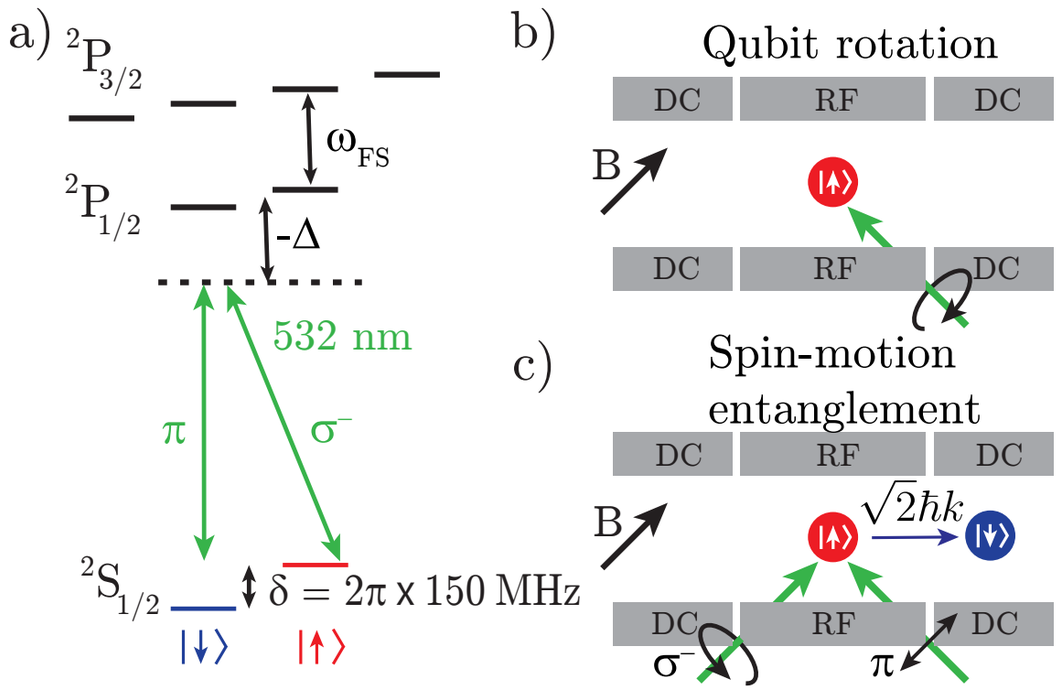

Figure 5.18: a) Energy levels relevant for the stimulated Raman transition. On the right, a top-down view of the ion (colored circle) with surrounding trap electrodes. The Raman beam directions with their polarizations are shown in green and the magnetic field direction in black. b) Schematic of ultrafast qubit rotation. A single, circularly-polarized beam drives the ion from $|\uparrow\rangle$ to $|\downarrow\rangle$. c) Schematic of spin-dependent kick, with the resulting momentum kick.

5.7.4 Single-Pulse Single Qubit Rotations

The finite bandwidth of the Raman pulse can only fully transfer population between degenerate levels, and any energy splitting leads to an effective detuning of the two-photon resonance, resulting in incomplete population transfer. The fidelity of a hyperbolic secant pulse with pulse area $\theta = \int \mathrm{d}t'\ \Omega(t')$ and temporal width τ_{pulse} driving population between a pair of states split by δ has been provided by Rosen and Zener [RZ32]:

$$\mathcal{F} = \sin^2\left(\frac{\theta}{2}\right)\mathrm{sech}^2(\delta\tau_{\mathrm{pulse}}/1.76). \tag{5.20}$$

First we demonstrate ultrafast single qubit rotations using a single, circularly-polarized beam directed orthogonal to the applied magnetic field (see Fig. 5.18(b)). For the given geometry, this polarization maximizes the two-photon Rabi frequency,

$\Omega_{2\gamma}$,

$$\Omega_{2\gamma} = \frac{\sqrt{2}}{6\Delta}\frac{d^2}{\hbar^2}\left(\frac{2\Delta}{\Delta - \omega_{\mathrm{FS}}} - 1\right)\left(E_\pi^* E_{\sigma_-} + E_{\sigma_+}^* E_\pi\right), \tag{5.21}$$

while canceling the differential light shift, $\delta_{2\gamma}$,

$$\delta_{2\gamma} = \frac{d^2}{6\hbar^2\Delta}\left(\frac{2\Delta}{\Delta - \omega_{\mathrm{FS}}} + 1\right)\left(|E_{\sigma^+}|^2 - |E_{\sigma^-}|^2\right), \tag{5.22}$$

with ω_{FS} the fine structure splitting, as shown in Fig. 5.18(a); $\Delta = \omega - \omega_0$ the difference between the laser frequency $\omega = c|\vec{k}|$, with $\vec{k}$ the laser wavevector, and the $^2\mathrm{S}_{1/2} \rightarrow {}^2\mathrm{P}^o_{1/2}$ transition resonance, ω_0; d the dipole moment of the same transition; and E_j the complex electric field amplitude for polarization j. The beam waist is measured to be $w_0 = 8.5(4)$ μm and the maximum pulse energy is 129(5) nJ. Preparing the ion in $|\uparrow\rangle$, applying a single laser pulse with varying energy, and reading out the final state we map out Rabi flopping curves such as that shown in Fig. 5.19. The maximum theoretical fidelity of $\mathcal{F}_{\mathrm{max}} = 0.9999$ is given by Eq. (5.20), and is high due to the small qubit energy splitting, $\delta/(2\pi) = 150\ \mathrm{M}Hz$, compared to the $\Delta f \approx 19\,\mathrm{GHz}$ bandwidth of the single pulse. To compare, using a hyperfine qubit with 10 GHz splitting, would limit the fidelity to 72%, demonstrating the benefit of the small splitting of a Zeeman qubit.

In the experiment, we see additional sources of infidelity. In Fig. 5.19 we see that the visibility scales inversely with the pulse area, or peak Rabi frequency. The additional infidelity can be explained by a thermal spread in the ion's initial position causing different regions of the laser beam to be sampled experiment to experiment. The distribution of Rabi frequencies leads to a decay in the visibility. This type of infidelity in ion traps was studied previously [CEN22], and an analytic solution for the transition probability can be found [Jaf18]

$$P_\downarrow = \frac{1}{2}\left(1 - {}_1F_2\left[\frac{g}{2}; \frac{1}{2}, 1 + \frac{g}{2}; -\theta^2\right]\right), \tag{5.23}$$

where ${}_1F_2[a; b, c; x]$ is a hypergeometric function, $g = \frac{w_0^2}{2\sigma_{\mathrm{ion}}^2}$ is the ratio of the beam waist to the thermal spread of the ion's position $\sigma_{\mathrm{ion}} = \sqrt{\frac{k_B T}{m\omega^2}}$ [KHB12], with m the ion mass, T the ion temperature, ω the trap frequency. Fitting the data to this function we extract the needed energy for a single laser pulse to perform a π rotation, 38(2) nJ, as well as the ion temperature, T =0.5(1) mK. Using the state

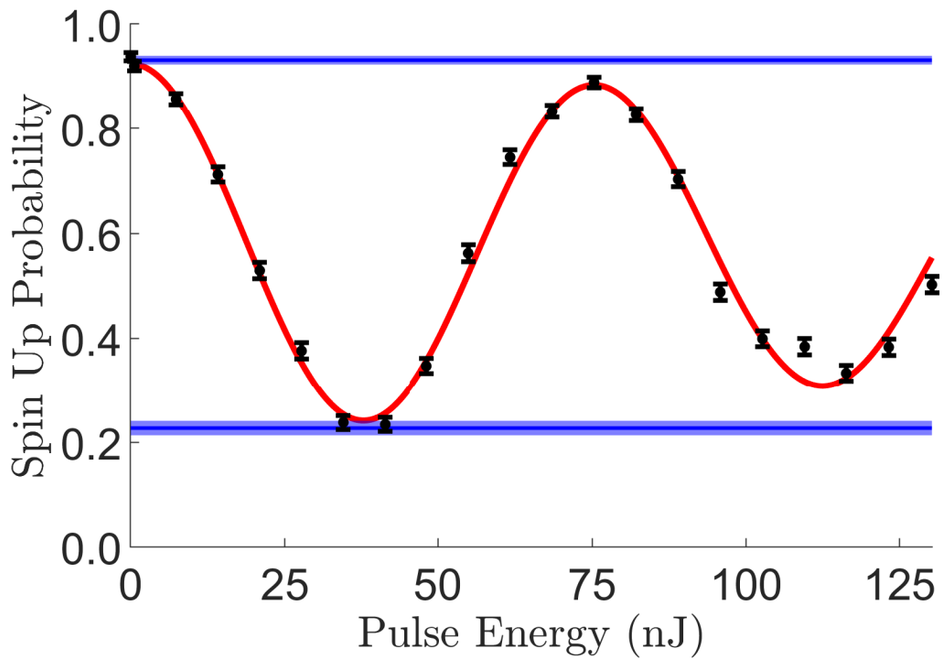

Figure 5.19: Ultrafast qubit rotations: a Rabi flopping curve produced by applying a single laser pulse of varying energy to an ion initially prepared in the $|\uparrow\rangle$ state. Black: data points with statistical error bars from 1000 repetitions of the experiment. Red: fit to the data, $\mathcal{V}_{\text{fit}} = 0.68$. Blue: bars indicate average state preparation and measurement (SPAM) limits for $|\downarrow\rangle$ and $|\uparrow\rangle$, $\mathcal{V}_{\text{SPAM}} = 0.70$. The width of the bars indicates the standard deviation of multiple SPAM measurements.

preparation and measurement (SPAM) limits shown in Fig. 5.19, we applied the Feldman-Cousins method to determine the 90% confidence interval for the SPAM-corrected fidelity of a π-pulse, $\mathcal{F}_{\text{thermal}} = (97^{+3}_{-4})\%$. The fidelity central value is given as the ratio of the visibility of the curve, $\mathcal{V}_{\text{fit}} = 0.68$, to the SPAM visibility, $\mathcal{V}_{\text{SPAM}} = 0.7$, with the visibility taken as the difference between the highest and lowest transition probabilities.

5.7.5 Single-Pulse Spin-Motion Entanglement

Next, we investigate spin-dependent kicks, a key component for two-qubit gates and matter wave interferometry. We drive stimulated Raman transitions of the qubit in a non-copropagating configuration (Fig. 5.18(c)), such that the internal state (spin) and motional state are left entangled. The polarization of the light is now

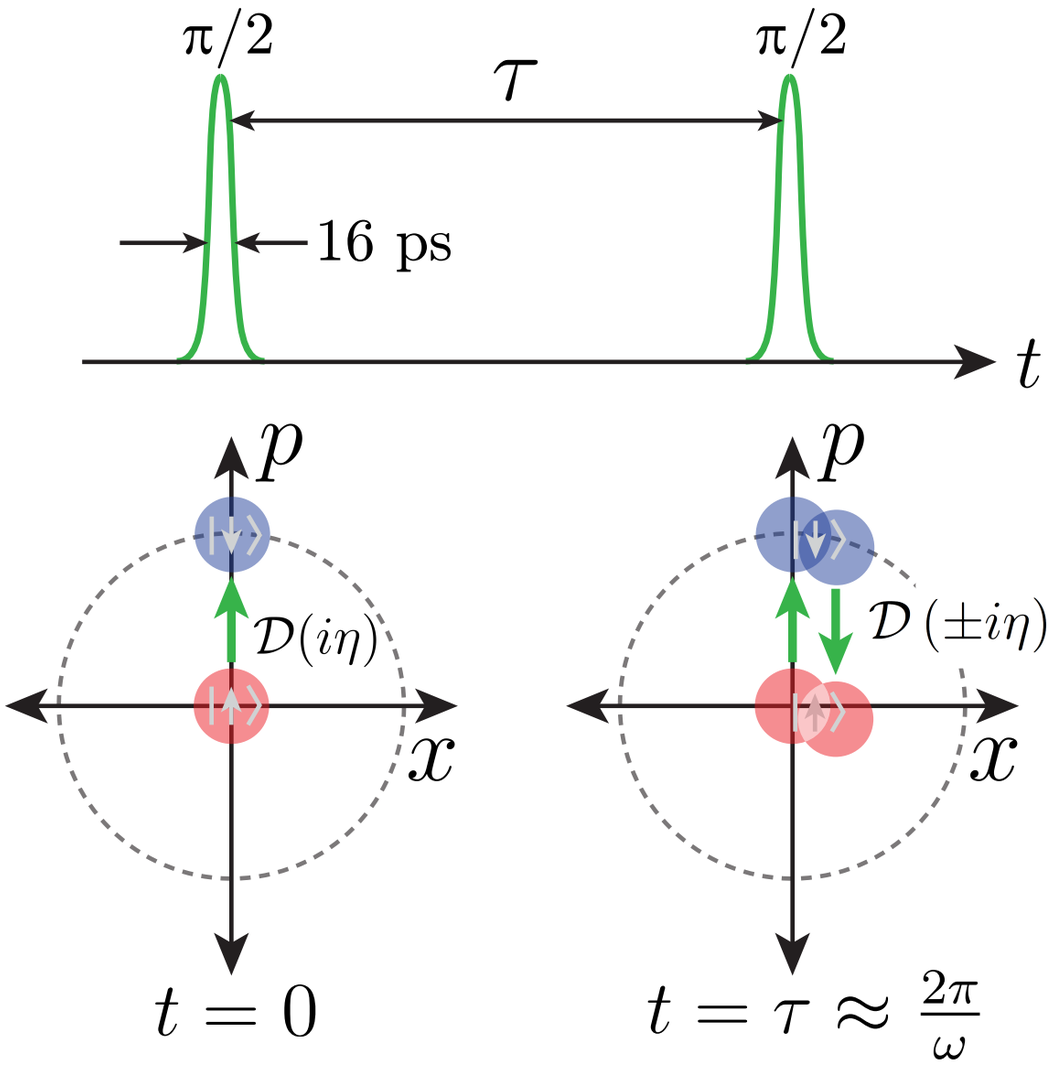

Figure 5.20: Modulation of wavepacket overlap due to spin-motion entanglement during Ramsey sequence. The evolution of the ion's coherent state is shown in phase space. Left: $\pi/2$ pulse splits wavepacket due to SDK and the kicked wavepacket will oscillate in the harmonic potential. Right: second $\pi/2$ pulse kicks remaining population. Overlap of wavepackets determines fringe visibility.

correlated with the direction of propagation such that population transfer can only occur by exchanging one photon from each beam, producing a spin-dependent kick: an ion initially in $|\uparrow\rangle$ ($|\downarrow\rangle$) receives a momentum kick of $\hbar\vec{k}_{\text{eff}}$ ($-\hbar\vec{k}_{\text{eff}}$) along the trap axial direction, where $\vec{k}_{\text{eff}}$ is the wavevector difference between the two beams, $\vec{k}_\sigma - \vec{k}_\pi$. This is equivalent to a displacement, $\mathcal{D}(i\eta)$, in phase space (Fig. 5.20), with $\eta \equiv |\vec{k}_{\text{eff}}|\sqrt{\frac{\hbar}{2m\omega}} = 0.56$ the effective Lamb-Dicke parameter. The kicks are

accompanied by a spin flip. Since the pulse width is much shorter than the trap period, we approximate the ultrafast kicks as instaneous momentum displacements and the time evolution operator for an impulsive SDK pulse between degenerate Raman levels becomes:

$$U(\theta) = \cos\left(\tfrac{\theta}{2}\right)\mathbb{1} + i\sin\left(\tfrac{\theta}{2}\right)[\mathcal{D}(i\eta)\hat{\sigma}_- + \mathcal{D}(-i\eta)\hat{\sigma}_+]\,, \tag{5.24}$$

where $\hat{\sigma}_+$ and $\hat{\sigma}_-$ are the qubit raising and lowering operators, which act on the internal state of the ion and are composed of the usual spin Pauli matrices, $\hat{\sigma}_x$, $\hat{\sigma}_y$, such that $\hat{\sigma}_\pm = \frac{1}{2}\left(\hat{\sigma}_x \pm i\hat{\sigma}_y\right)$.

To explicitly demonstrate the spin-dependent kick, we prepare the ion in $|\uparrow\rangle$ and perform a Ramsey pulse sequence consisting of two SDK $\pi/2$ pulses separated by a variable time, τ, set by the pulse picker, during which the ion undergoes harmonic motion in the trap (Fig. 5.20). For each wait time Ramsey interference fringes (see insets of Fig. 5.21) were mapped versus detuning, δ, by scanning the qubit splitting via the static magnetic field. The first SDK $\pi/2$ pulse produces a momentum kick described by a displacement operator $\mathcal{D}(i\eta)$. The time evolution operator during the Ramsey wait time, U_{wait}, causes the qubit internal state, $|\psi\rangle$, to pick up a phase $\phi_{\uparrow(\downarrow)} = (-)\delta\tau/2$ and the coherent state evolution, $|\alpha\rangle \rightarrow |\alpha e^{-i\omega\tau}\rangle$, as the ion oscillates in the trap. The degree of wavepacket overlap is encoded in the Ramsey interference fringe visibility $\mathcal{V}$ and is dependent on the timing of the second $\pi/2$ pulse as illustrated in Fig. 5.20.

The wavepacket overlap after the second $\pi/2$ pulse depends on the initial motional distribution of the ion. Doppler cooling prepares the ion in a thermal state with a mean occupation number $\bar{n}$ in the harmonic oscillator potential. The thermal distribution creates a mixed state, which can be expressed using the Glauber-Sudashan distribution $\rho = \int \mathrm{d}\alpha\ P_G(\alpha)|\psi,\alpha\rangle\langle\psi,\alpha|$, with $P_G(\alpha) = \frac{1}{\pi\bar{n}}e^{-|\alpha|^2/\bar{n}}$ for a thermal distribution of coherent states, $|\alpha\rangle$, with an average occupation number $\bar{n}$. The final density matrix is found by evolving the wavefunction according to Eq. (5.24), $|\psi_{\text{f}},\alpha_{\text{f}}\rangle = U(\frac{\pi}{2})U_{wait}U(\frac{\pi}{2})|\psi_{\text{i}},\alpha_{\text{i}}\rangle$. The population of the ion's internal states is then found by tracing out the motion from the density matrix: $P_\uparrow = \langle\uparrow|\text{Tr}_\alpha(\rho)|\uparrow\rangle$ [JNM15].

Leading to the probability to remain in the $|\uparrow\rangle$ state, with $\gamma = \delta\tau + \eta^2 \sin\omega\tau$:

$$P_\uparrow = \frac{1}{2} - \frac{1}{2}\cos(\gamma)\exp\left[-\eta^2(1-\cos\omega\tau)(2\bar{n}+1)\right]. \tag{5.25}$$

Scanning over the detuning gives a sinusoidal fringe from which we determine the visibility, $\mathcal{V}$, the difference between the maximum and minimum transition probability:

$$\mathcal{V} = \exp[-\eta^2(1-\cos\omega\tau)(2\bar{n}+1)]. \tag{5.26}$$

Initially, as the wavepackets separate, the visibility rapidly decays. The wavepackets re-overlap in phase space after an integer number of trap periods, $T = 2\pi/\omega$, and the fringe visibility revives as shown in the top plot of Fig. 5.21. The width of the decay and revivals is dependent on the combination of ion parameters $2\eta^2(2\bar{n}+1)$.

Fitting the fringe visibility at each value of the wait time gives the data plotted in Fig. 5.21, with error bars given by the fit uncertainty. Representative Ramsey fringes with their fits are inset with arrows indicating the corresponding Ramsey wait time. The red line is a fit to the data according to Eq. (5.26) with an additional offset $A = 0.036(4)$ that accounts for quantum projection noise during data collection, as well as an overall scaling factor, $B = 0.41(2)$ accounting for the finite fidelity of this operation and our readout procedure:

$$\mathcal{V} = A + B\exp\left[-\eta^2(1-\cos\omega\tau)(2\bar{n}+1)\right]. \tag{5.27}$$

From this fit we extract a revival time of $\tau_{\text{rev}} = 30.864(1)$ μs. The corresponding secular frequency of $\omega = 2\pi\times$ 32.400(1) kHz is in good agreement with an independent measurement of the axial secular frequency using the "tickle scan" method [DMM04]. The fit value for the mean occupation number $\bar{n} = 1059(80)$ implies a temperature of 1.6(1) mK.

Using known sources of infidelity, we can account for the max fringe visibility, $\mathcal{V}_{\text{max}} = 0.45(2)$, of the spin-motion entanglement. The visibility is reduced due to the limited SPAM visibility, the infidelity of the SDK pulses, and the ion coherence time. Unlike in the single-beam single-qubit rotation experiment, the electric field polarization at the ion when using two beams has no σ^+ component. This leads to a differential light shift of the qubit states dependent on the strength of the σ^-

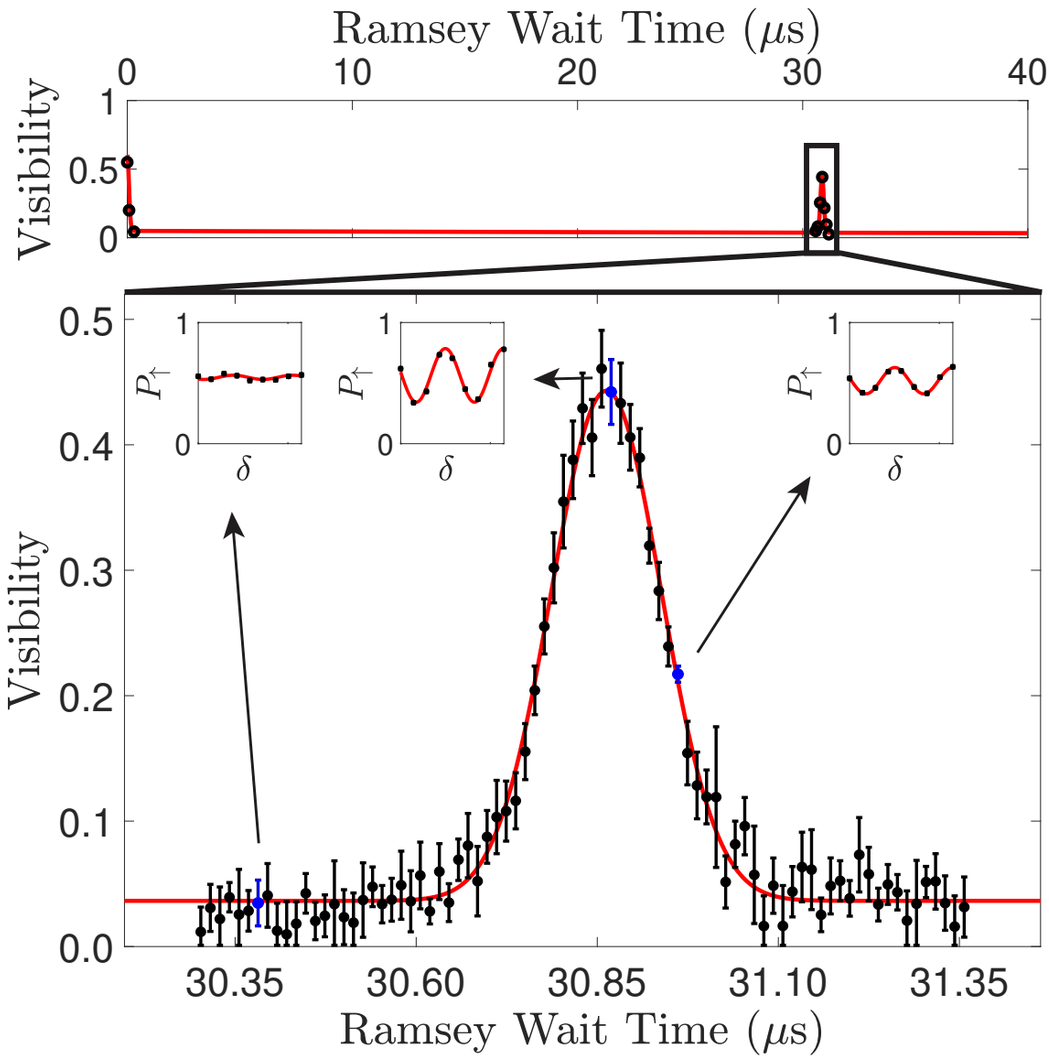

Figure 5.21: Collapse and revival of spin coherence at the trap period. The topmost plot shows the decay and revival of the Ramsey fringe visibility after the ion has oscillated through one axial trap period. The main plot shows the revival from the top plot and the data points are the best-fit amplitude values of Ramsey fringes as a function of the applied wait time, the red line is a fit to Eq. (5.27). Inset shows some representative fringes.

polarized beam, as seen in Eq. (5.22). Lowering the intensity of the σ^- polarized beam reduces the differential shift but requires higher intensity of the π polarized beam to maintain the same Rabi frequency. Numerically solving the Schrodinger equation, we find that with a pulse energy of 14 nJ for the σ^- polarized beam at about half the energy of the π-polarized beam (24 nJ) the differential light shift

limits our fidelity to $\mathcal{F}_{\text{lightshift}} = 0.95(1)$. We calculate the overall visibility $\mathcal{V}_{\text{tot}} = \mathcal{V}_{\text{SPAM}} \times \mathcal{F}_{\text{SDK}} \times \exp(-\tau_{\text{rev}}/T_2) = 0.47(4)$, taking $\mathcal{V}_{\text{SPAM}} = 0.70(3)$ from Fig. 5.19, $\mathcal{F}_{\text{SDK}} = \mathcal{F}_{\text{thermal}} \times \mathcal{F}_{\text{lightshift}} = 0.92(3)$, and from auxiliary measurements, the Zeeman qubit coherence time, $T_2 \approx 100$ μs.

5.7.6 Conclusion

We have demonstrated ultrafast control of a trapped ion Zeeman qubit. Using a high-intensity mode-locked laser to drive a Raman transition, we can perform a single qubit π-rotation using a single laser pulse, in approximately 16.4(5) ps. The fidelity of this qubit rotation is estimated to be $(97^{+3}_{-4})\%$, currently limited by the ion's thermal position spread. Operating in a non-copropagating geometry, the same Raman transition was used to perform ultrafast spin-motion entanglement, a key ingredient for two-qubit gates and matter-wave interferometry. The momentum imparted by the resulting spin-dependent kick leads to a reduction in the fringe visibility of a Ramsey pulse sequence as the wavepackets separate. Revival of the visibility is observed at a time equal to the trap period, and the variation of the visibility allows us to infer both the efficiency of spin-motion entanglement and the mean occupation number of the trapped ion.

In contrast to previous work with hyperfine qubits [MMM06, CMQ10, MSN13, WMJ17], the fideltiy of the spin-motion entanglement is not limited by multi-photon transitions. Polarization selectivity precludes diffraction of the atomic wavepacket into multiple momentum orders. For applications, such as matter wave interferometry, where higher momentum transfer is beneficial, retroreflecting the SDK beams can double the momentum transfer while returning the ion to its initial state, enabling SDKs to be applied at the repetition rate of the laser.

Further improvements can be achieved by increasing the fidelity of the state readout, decreasing the ion's thermal position spread, decreasing the differential light shift, and increasing the qubit coherence. Increasing the SPAM fidelity will increase the Ramsey fringe visibility and enable a more precise measurement of the fidelity of ultrafast qubit operations. This can be achieved by using the narrow $^2\text{S}_{1/2} \leftrightarrow {}^2\text{D}_{5/2}$ transition to perform electron shelving [DKN10, YMD17]. The ion's

spread in position is strongly dependent on the trap secular frequency. For a $^{138}Ba^{+}$ ion cooled to the Doppler limit in a trap with $\omega_{\text{sec}} = 2\pi \times 200$ kHz this source of infidelity is reduced to the 10^{-5} level. By choosing a laser at the "magic" wavelength ($\lambda \approx 480\,\text{nm}$ Ba^{+}, corresponding to frequency $\omega = \omega_0 + \omega_{\text{FS}}/3$), the differential light shift can be nulled, as seen in Eq. (5.22). The coherence time can be increased by using permanent magnets to decrease the magnetic field noise. Zeeman qubits coherence times exceeding 1 s were demonstrated in [RSK16]. The spin-dependent kick scheme that we have demonstrated here will be harnessed to perform trapped-ion interferometry [CH17, Wes19].

CHAPTER 6

Conclusion

Using a single, high-intensity pulse from a mode-locked laser, ultrafast control of a trapped ion Zeeman qubit has been demonstrated. Single-pulse stimulated Raman transitions using Zeeman qubits, contrasted to previous work with hyperfine qubits [MMM06, CMQ10, MSN13, WMJ17], are not as suseptible to the single-qubit-rotation infidelity due to the laser pulse's finite bandwidth. The state-dependent momentum transfer using stimulated Raman transitions in Zeeman qubits is not limited by multi-photon transitions due to polarization selectivity, preventing diffraction of the atomic wavepacket into multiple momentum orders. Single qubit rotations are performed in approximately 16.4(5) ps, the laser pulse length, and the fidelity of this qubit operation is estimated to be $(97^{+3}_{-4})\%$, currently limited by the ion's thermal position spread. Stimulating Raman transitions in a non-copropagating geometry, a single laser pulse generated entanglement between the ion's momentum and internal spin state. The momentum imparted by the resulting spin-dependent kick leads to separation of the different spin states. The wavepacket separation can be observed from the reduction of fringe visibility when performing Ramsey experiments. Revival of the visibility is observed as the wavepackets re-overlap in phase space due to the harmonic potential provided by the ion trap. The efficiency of spin-motion entanglement and the mean occupation number of the trapped ion are inferred from the variation of the fringe visibility.

In light of the results presented here, the original idea of constructing a trapped ion interferometer gyroscope becomes more feasible. To realize a high-sensitivity ion gyroscope as described in the original experiment proposal [CH17], the current experimental setup will need to advance in several areas. First, to be sensitive to the Sagnac effect, the interferometer paths must enclose a non-zero area. The research presented here only investigated 1D interferometry with spin-dependent kicks along

a single axis. As mentioned in [CH17], the ion orbits can be constructed from a kick and a displacement. The kicking operation has been shown in this research and a DC voltage step on the trapping electrodes can be used to displace the ion from the trap center. This operation needs to be studied and characterized. Second, large-momentum beamsplitter operations must be investigated. The SDK scheme shown here will cause consecutive kick momentum to cancel out. To avoid this, the beam polarization can be quickly switched, but a simpler implementation would be to retro-reflect the pulses to the ion such that the momentum transfer from consecutive pulses adds together. Finally, the experiment proposal supposes 100 kicks and 100 ion orbits while this research has only investigated single SDKs and interferometer operation on the order of a single ion trap period. With the current kick fidelity of 95%, the Ramsey fringe visibility will be washed out after just 14 kicks: $(0.95)^{14} < 0.5$. The observed Ramsey fringe decoherence of $T_2 = 100$ μs will limit the number of ion orbits to less than 4 for the trap period used here of 30 μs.

Further improvements of the SDK operations include increasing the fidelity of the state readout, decreasing the ion's thermal position spread, decreasing the differential light shift, and increasing the qubit coherence. Increasing the SPAM fidelity will increase the Ramsey fringe visibility and enable a more precise measurement of the fidelity of ultrafast qubit operations. This can be achieved by using the narrow $^2S_{1/2} \leftrightarrow {}^2D_{5/2}$ transition to perform electron shelving [DKN10, YMD17]. The ion's spread in position can be decreased by increasing the trap secular frequency. Operating with a $^{138}Ba^+$ ion cooled to the Doppler limit in a $\omega_{sec} = 2\pi \times 200$ kHz trap would reduce this source of infidelity to the 10^{-5} level. As seen in Eq. (5.22), the differential light shift can be nulled by choosing a laser at the "magic" wavelength ($\lambda \approx 480\,\text{nm}$ Ba^+, corresponding to frequency $\omega = \omega_0 + \omega_{FS}/3$). The ion coherence time can be increased by using permanent magnets to decrease the magnetic field noise. Zeeman qubits coherence times exceeding 1 s have been demonstrated in [RSK16].

The End

[ACM20] Andrei Afanasev, Carl E. Carlson, and Asmita Mukherjee. "Recoil Momentum Effects in Quantum Processes Induced by Twisted Photons.", 2020.

[ASS10] D T C Allcock, J A Sherman, D N Stacey, A H Burrell, M J Curtis, G Imreh, N M Linke, D J Szwer, S C Webster, A M Steane, and D M Lucas. "Implementation of a symmetric surface-electrode ion trap with field compensation using a modulated Raman effect." *New Journal of Physics*, **12**(5):053026, 05 2010.

[BCK13] C D B Bentley, A R R Carvalho, D Kielpinski, and J J Hope. "Fast gates for ion traps by splitting laser pulses." *New Journal of Physics*, **15**(4):043006, 04 2013.

[BCM19] Colin D. Bruzewicz, John Chiaverini, Robert McConnell, and Jeremy M. Sage. "Trapped-ion quantum computing: Progress and challenges." *Applied Physics Reviews*, **6**(2):021314, 2019.

[CBZ92] J. I. Cirac, R. Blatt, P. Zoller, and W. D. Phillips. "Laser cooling of trapped ions in a standing wave." *Phys. Rev. A*, **46**:2668–2681, 09 1992.

[CEN20] M. Cetina, L. N. Egan, C. A. Noel, M. L. Goldman, A. R. Risinger, D. Zhu, D. Biswas, and C. Monroe. "Quantum Gates on Individually-Addressed Atomic Qubits Subject to Noisy Transverse Motion.", 2020.

[CEN22] M. Cetina, L.N. Egan, C. Noel, M.L. Goldman, D. Biswas, A.R. Risinger, D. Zhu, and C. Monroe. "Control of Transverse Motion for Quantum Gates on Individually Addressed Atomic Qubits." *PRX Quantum*, **3**:010334, 03 2022.

[CH17] W C Campbell and P Hamilton. "Rotation sensing with trapped ions." *Journal of Physics B: Atomic, Molecular and Optical Physics*, **50**(6):064002, 02 2017.

[CKC11] Sheng-wey Chiow, Tim Kovachy, Hui-Chun Chien, and Mark A. Kasevich. "102$\hbar k$ Large Area Atom Interferometers." *Phys. Rev. Lett.*, **107**:130403, 09 2011.

[CMC08] Malo Cadoret, Estefania de Mirandes, Pierre Cladé, Saïda Guellati-Khélifa, Catherine Schwob, Fran çois Nez, Lucile Julien, and Fran çois Biraben. "Combination of Bloch Oscillations with a Ramsey-Bordé Interferometer: New Determination of the Fine Structure Constant." *Phys. Rev. Lett.*, **101**:230801, 12 2008.

[CMQ10] W. C. Campbell, J. Mizrahi, Q. Quraishi, C. Senko, D. Hayes, D. Hucul, D. N. Matsukevich, P. Maunz, and C. Monroe. "Ultrafast Gates for Single Atomic Qubits." *Phys. Rev. Lett.*, **105**:090502, 08 2010.

[CSP09] Alexander D. Cronin, Jörg Schmiedmayer, and David E. Pritchard. "Optics and interferometry with atoms and molecules." *Rev. Mod. Phys.*, **81**:1051–1129, 07 2009.

[CZ95] J. I. Cirac and P. Zoller. "Quantum Computations with Cold Trapped Ions." *Phys. Rev. Lett.*, **74**:4091–4094, 05 1995.

[DKN10] M. R. Dietrich, N. Kurz, T. Noel, G. Shu, and B. B. Blinov. "Hyperfine and optical barium ion qubits." *Phys. Rev. A*, **81**:052328, 05 2010.

[DLF16] S. Debnath, N. M. Linke, C. Figgatt, K. A. Landsman, K. Wright, and C. Monroe. "Demonstration of a small programmable quantum computer with atomic qubits." *Nature*, **536**(7614):63–66, 08 2016.

[DMM04] M. Drewsen, A. Mortensen, R. Martinussen, P. Staanum, and J. L. Sørensen. "Nondestructive Identification of Cold and Extremely Localized Single Molecular Ions." *Phys. Rev. Lett.*, **93**:243201, 12 2004.

[Dua04] L.-M. Duan. "Scaling Ion Trap Quantum Computation through Fast Quantum Gates." *Phys. Rev. Lett.*, **93**:100502, 09 2004.

[GSS14] Dylan J Gorman, Philipp Schindler, Sankaranarayanan Selvarajan, Nikos Daniilidis, and Hartmut Häffner. "Two-mode coupling in a single-ion oscillator via parametric resonance." *Phys. Rev. A*, **89**:062332, 06 2014.

[GTL16] J. P. Gaebler, T. R. Tan, Y. Lin, Y. Wan, R. Bowler, A. C. Keith, S. Glancy, K. Coakley, E. Knill, D. Leibfried, and D. J. Wineland. "High-Fidelity Universal Gate Set for $^{9}Be^{+}$ Ion Qubits." *Phys. Rev. Lett.*, **117**:060505, 08 2016.

[GWH22] W.-X. Guo, Y.-K. Wu, Y.-Y. Huang, L. Feng, C.-X. Huang, H.-X. Yang, J.-Y. Ma, L. Yao, Z.-C. Zhou, and L.-M. Duan. "Picosecond ion-qubit manipulation and spin-phonon entanglement with resonant laser pulses." *Phys. Rev. A*, **106**:022608, Aug 2022.

[GZC03] J. J. García-Ripoll, P. Zoller, and J. I. Cirac. "Speed Optimized Two-Qubit Gates with Laser Coherent Control Techniques for Ion Trap Quantum Computing." *Phys. Rev. Lett.*, **91**:157901, 10 2003.

[HMM10] D. Hayes, D. N. Matsukevich, P. Maunz, D. Hucul, Q. Quraishi, S. Olmschenk, W. Campbell, J. Mizrahi, C. Senko, and C. Monroe. "Entanglement of Atomic Qubits Using an Optical Frequency Comb." *Phys. Rev. Lett.*, **104**:140501, 04 2010.

[HSA16] T. P. Harty, M. A. Sepiol, D. T. C. Allcock, C. J. Ballance, J. E. Tarlton, and D. M. Lucas. "High-Fidelity Trapped-Ion Quantum Logic Using Near-Field Microwaves." *Phys. Rev. Lett.*, **117**:140501, 09 2016.

[ICL17] I. V. Inlek, C. Crocker, M. Lichtman, K. Sosnova, and C. Monroe. "Multispecies Trapped-Ion Node for Quantum Networking." *Phys. Rev. Lett.*, **118**:250502, 06 2017.

[IS08] E. Iskrenova-Tchoukova and M. S. Safronova. "Theoretical study of lifetimes and polarizabilities in Ba^{+}." *Phys. Rev. A*, **78**:012508, 07 2008.

[Jaf18] Matthew Jaffe. *Atom interferometry in an optical cavity.* PhD thesis, University of California, Berkeley, 2018.

[Jam98] D. F. V. James. "Quantum dynamics of cold trapped ions with application to quantum computation." *Applied Physics B*, **66**(2):181–190, 02 1998.

[JNM15] K. G. Johnson, B. Neyenhuis, J. Mizrahi, J. D. Wong-Campos, and C. Monroe. "Sensing Atomic Motion from the Zero Point to Room Temperature with Ultrafast Atom Interferometry." *Phys. Rev. Lett.*, **115**:213001, 11 2015.

[JXH18] Matt Jaffe, Victoria Xu, Philipp Haslinger, Holger Müller, and Paul Hamilton. "Efficient Adiabatic Spin-Dependent Kicks in an Atom Interferometer." *Phys. Rev. Lett.*, **121**:040402, 07 2018.

[KHB12] S. Knünz, M. Herrmann, V. Batteiger, G. Saathoff, T. W. Hänsch, and Th. Udem. "Sub-millikelvin spatial thermometry of a single Doppler-cooled ion in a Paul trap." *Phys. Rev. A*, **85**:023427, 02 2012.

[Kle13] Daniel Kleppner. "Norman Ramsey and his method." *Physics Today*, **66**:25, 01 2013.

[Kni81] R. D. Knight. "Storage of ions from laser-produced plasmas." *Applied Physics Letters*, **38**(4):221–223, 02 1981.

[Lab] Mittleman Lab. "Measuring Ultrashort Laser Pulses I: Autocorrelation." Available at https://www.brown.edu/research/labs/mittleman/sites/brown.edu.research.labs.mittleman/files/uploads/lecture14.pdf.

[LBM03] D. Leibfried, R. Blatt, C. Monroe, and D. Wineland. "Quantum dynamics of single trapped ions." *Rev. Mod. Phys.*, **75**:281–324, 03 2003.

[LGA08] Jaroslaw Labaziewicz, Yufei Ge, Paul Antohi, David Leibrandt, Kenneth R. Brown, and Isaac L. Chuang. "Suppression of Heating Rates in Cryogenic Surface-Electrode Ion Traps." *Phys. Rev. Lett.*, **100**:013001, 01 2008.

[Mar97] Raymond E. March. "An Introduction to Quadrupole Ion Trap Mass Spectrometry." *Journal of Mass Spectrometry*, **32**(4):351–369, 1997.

[MCH09] Holger Müller, Sheng-wey Chiow, Sven Herrmann, and Steven Chu. "Atom Interferometers with Scalable Enclosed Area." *Phys. Rev. Lett.*, **102**:240403, 06 2009.

[MMK96] C. Monroe, D. M. Meekhof, B. E. King, and D. J. Wineland. "A "Schrödinger Cat" Superposition State of an Atom." *Science*, **272**(5265):1131–1136, 1996.

[MMM06] M. J. Madsen, D. L. Moehring, P. Maunz, R. N. Kohn, L.-M. Duan, and C. Monroe. "Ultrafast Coherent Excitation of a Trapped Ion Qubit for Fast Gates and Photon Frequency Qubits." *Phys. Rev. Lett.*, **97**:040505, 07 2006.

[MS99] Klaus Mølmer and Anders Sørensen. "Multiparticle Entanglement of Hot Trapped Ions." *Phys. Rev. Lett.*, **82**:1835–1838, 03 1999.

[MSN13] J. Mizrahi, C. Senko, B. Neyenhuis, K. G. Johnson, W. C. Campbell, C. W. S. Conover, and C. Monroe. "Ultrafast Spin-Motion Entanglement and Interferometry with a Single Atom." *Phys. Rev. Lett.*, **110**:203001, 05 2013.

[NDM11] S. Narayanan, N. Daniilidis, S. A. Möller, R. Clark, F. Ziesel, K. Singer, F. Schmidt-Kaler, and H. Häffner. "Electric field compensation and sensing with a single ion in a planar trap." *Journal of Applied Physics*, **110**(11):114909, 2011.

[OIB07] R. Ozeri, W. M. Itano, R. B. Blakestad, J. Britton, J. Chiaverini, J. D. Jost, C. Langer, D. Leibfried, R. Reichle, S. Seidelin, J. H. Wesenberg, and D. J. Wineland. "Errors in trapped-ion quantum gates due to spontaneous photon scattering." *Phys. Rev. A*, **75**:042329, 04 2007.

[OLA08] C. Ospelkaus, C. E. Langer, J. M. Amini, K. R. Brown, D. Leibfried, and D. J. Wineland. "Trapped-Ion Quantum Logic Gates Based on Oscillating Magnetic Fields." *Phys. Rev. Lett.*, **101**:090502, 08 2008.

[OWC11] C. Ospelkaus, U. Warring, Y. Colombe, K. R. Brown, J. M. Amini, D. Leibfried, and D. J. Wineland. "Microwave quantum logic gates for trapped ions." *Nature*, **476**(7359):181–184, 08 2011.

[PBB19] G. Pagano, A. Bapat, P. Becker, K. S. Collins, A. De, P. W. Hess, H. B. Kaplan, A. Kyprianidis, W. L. Tan, C. Baldwin, L. T. Brady, A. Deshpande, F. Liu, S. Jordan, A. V. Gorshkov, and C. Monroe. "Quantum Approximate Optimization of the Long-Range Ising Model with a Trapped-Ion Quantum Simulator.", 2019.

[PK15] Thaned Pruttivarasin and Hidetoshi Katori. "Compact field programmable gate array-based pulse-sequencer and radio-frequency generator for experiments with trapped atoms." *Review of Scientific Instruments*, **86**(11):115106, 11 2015.

[POS67] E. J. POST. "Sagnac Effect." *Rev. Mod. Phys.*, **39**:475–493, Apr 1967.

[PYZ18] Richard H. Parker, Chenghui Yu, Weicheng Zhong, Brian Estey, and Holger Müller. "Measurement of the fine-structure constant as a test of the Standard Model." *Science*, **360**(6385):191–195, 2018.

[PZP19] Zachary Pagel, Weicheng Zhong, Richard H. Parker, Christopher T. Olund, Norman Y. Yao, and Holger Mueller. "Bloch beamsplitters and dual-lattice methods for atom interferometry.", 2019.

[RAM14] René Reimann, Wolfgang Alt, Tobias Macha, Dieter Meschede, Natalie Thau, Seokchan Yoon, and Lothar Ratschbacher. "Carrier-free Raman manipulation of trapped neutral atoms." *New Journal of Physics*, **16**(11):113042, 11 2014.

[Rei99] R. J. Reid. *CLEANING FOR VACUUM SERVICE*. CERN, 1999.

[RHS20] Zak David Romaszko, Seokjun Hong, Martin Siegele, Reuben Kahan Puddy, Foni RaphaÃl Lebrun-Gallagher, Sebastian Weidt, and Winfried Karl Hensinger. "Engineering of microfabricated ion traps and integration of advanced on-chip features." *Nature Reviews Physics*, 05 2020.

[RKW91] F. Riehle, Th. Kisters, A. Witte, J. Helmcke, and Ch. J. Bordé. "Optical Ramsey spectroscopy in a rotating frame: Sagnac effect in a matter-wave interferometer." *Phys. Rev. Lett.*, **67**:177–180, Jul 1991.

[RSK16] T. Ruster, C. T. Schmiegelow, H. Kaufmann, C. Warschburger, F. Schmidt-Kaler, and U. G. Poschinger. "A long-lived Zeeman trapped-ion qubit." *Applied Physics B*, **122**(10), 09 2016.

[RZ32] N. Rosen and C. Zener. "Double Stern-Gerlach Experiment and Related Collision Phenomena." *Phys. Rev.*, **40**:502–507, 05 1932.

[SBS19] R. Srinivas, S. C. Burd, R. T. Sutherland, A. C. Wilson, D. J. Wineland, D. Leibfried, D. T. C. Allcock, and D. H. Slichter. "Trapped-Ion Spin-Motion Coupling with Microwaves and a Near-Motional Oscillating Magnetic Field Gradient." *Phys. Rev. Lett.*, **122**:163201, 04 2019.

[SCR06] S. Seidelin, J. Chiaverini, R. Reichle, J. J. Bollinger, D. Leibfried, J. Britton, J. H. Wesenberg, R. B. Blakestad, R. J. Epstein, D. B. Hume, W. M. Itano, J. D. Jost, C. Langer, R. Ozeri, N. Shiga, and D. J. Wineland. "Microfabricated Surface-Electrode Ion Trap for Scalable Quantum Information Processing." *Phys. Rev. Lett.*, **96**:253003, 06 2006.

[SFH10] D Stick, K M Fortier, R Haltli, C Highstrete, D L Moehring, C Tigges, and M G Blain. "Demonstration of a microfabricated surface electrode ion trap.", 2010.

[SFS17] Makfir Sefa, James A. Fedchak, and Julia Scherschligt. "Investigations of medium-temperature heat treatments to achieve low outgassing rates in stainless steel ultrahigh vacuum chambers." *Journal of Vacuum Science & Technology A*, **35**(4):041601, 05 2017.

[Sie86] Anthony E. Siegman. *Lasers*. University Science Books, 1986.

[SIH14] A M Steane, G Imreh, J P Home, and D Leibfried. "Pulsed force sequences for fast phase-insensitive quantum gates in trapped ions." *New Journal of Physics*, **16**(5):053049, 05 2014.

[SM99] Anders Sørensen and Klaus Mølmer. "Quantum Computation with Ions in Thermal Motion." *Phys. Rev. Lett.*, **82**:1971–1974, 03 1999.

[SM00] Anders Sørensen and Klaus Mølmer. "Entanglement and quantum computation with ions in thermal motion." *Phys. Rev. A*, **62**:022311, 07 2000.

[SSB19] R T Sutherland, R Srinivas, S C Burd, D Leibfried, A C Wilson, D J Wineland, D T C Allcock, D H Slichter, and S B Libby. "Versatile laser-free trapped-ion entangling gates." *New Journal of Physics*, **21**(3):033033, 03 2019.

[SSB20] R. T. Sutherland, R. Srinivas, S. C. Burd, H. M. Knaack, A. C. Wilson, D. J. Wineland, D. Leibfried, D. T. C. Allcock, D. H. Slichter, and S. B. Libby. "Laser-free trapped-ion entangling gates with simultaneous insensitivity to qubit and motional decoherence." *Phys. Rev. A*, **101**:042334, 04 2020.

[SSK16] Christian T. Schmiegelow, Jonas Schulz, Henning Kaufmann, Thomas Ruster, Ulrich G. Poschinger, and Ferdinand Schmidt-Kaler. "Transfer of optical orbital angular momentum to a bound electron." *Nature Communications*, **7**(1):12998, 10 2016.

[Ste] Daniel Steck. "Quantum and Atomic Optics." Available at https://www.https://atomoptics.uoregon.edu/~dsteck/teaching/quantum-optics/quantum-optics-notes.pdf.

[UAK20] Eduardo Uruñuela, Wolfgang Alt, Elvira Keiler, Dieter Meschede, Deepak Pandey, Hannes Pfeifer, and Tobias Macha. "Ground-state cooling of a single atom inside a high-bandwidth cavity." *Phys. Rev. A*, **101**:023415, 02 2020.

[VVE90] Fernande Vedel, Michel Vedel, and Raymond Evans March. "New Schemes for resonant ejection in r.f. quadrupolar ion traps." *International Journal of Mass Spectrometry and Ion Processes*, **99**(1):125–138, 1990.

[Wes08] J. H. Wesenberg. "Electrostatics of surface-electrode ion traps." *Phys. Rev. A*, **78**:063410, 12 2008.

[Wes19] Adam D. West. "Systematic effects in two-dimensional trapped matter-wave interferometers." *Phys. Rev. A*, **100**:063622, 12 2019.

[WMI98] D. J. Wineland, C. Monroe, W. M. Itano, D. Leibfried, B. E. King, and D. M. Meekhof. "Experimental Issues in Coherent Quantum-State Manipulation of Trapped Atomic Ions." *Journal of research of the National Institute of Standards and Technology*, **103**(3):259–328, 1998.

[WMJ17] J. D. Wong-Campos, S. A. Moses, K. G. Johnson, and C. Monroe. "Demonstration of Two-Atom Entanglement with Ultrafast Optical Pulses." *Phys. Rev. Lett.*, **119**:230501, 12 2017.

[WPC21] Adam D West, Randall Putnam, Wesley C Campbell, and Paul Hamilton. "Tunable transverse spin–motion coupling for quantum information processing." *Quantum Science and Technology*, **6**(2):024003, 01 2021.

[WWC18] A. E. Webb, S. C. Webster, S. Collingbourne, D. Bretaud, A. M. Lawrence, S. Weidt, F. Mintert, and W. K. Hensinger. "Resilient Entangling Gates for Trapped Ions." *Phys. Rev. Lett.*, **121**:180501, 11 2018.

[YMD17] Dahyun Yum, Debashis De Munshi, Tarun Dutta, and Manas Mukherjee. "Optical barium ion qubit." *J. Opt. Soc. Am. B*, **34**(8):1632–1636, 08 2017.

[ZHM19] G. Zarantonello, H. Hahn, J. Morgner, M. Schulte, A. Bautista-Salvador, R. F. Werner, K. Hammerer, and C. Ospelkaus. "Robust and Resource-Efficient Microwave Near-Field Entangling $^{9}Be^{+}$ Gate." *Phys. Rev. Lett.*, **123**:260503, 12 2019.